AD
A108553

INSTITUTE

FOR

AEROSPACE STUDIES

LEVEL II (12)

UNIVERSITY OF TORONTO

PSEUDO-STATIONARY OBLIQUE SHOCK-WAVE REFLECTION

IN CARBON DIOXIDE — DOMAINS AND BOUNDARIES

by

Samon Ando

DTIC
S ELECTE
DEC 1 5 1981
E

April, 1981

81 12 14 031

REPORT DOCUMENTATION PAGE	READ INSTRUCTIONS BEFORE COMPLETING FORM

1. REPORT NUMBER	2. GOVT ACCESSION NO.	3. RECIPIENT'S CATALOG NUMBER
AFOSR-TR- 81-0807	AD A108 533	

4. TITLE (and Subtitle)	5. TYPE OF REPORT & PERIOD COVERED
PSEUDO-STATIONARY OBLIQUE SHOCK-WAVE REFLECTION IN CARBON DIOXIDE - DOMAINS AND BOUNDARIES	Interim
	6. PERFORMING ORG. REPORT NUMBER UTIAS Tech. Note No. 231

7. AUTHOR(s)	8. CONTRACT OR GRANT NUMBER(s)
Samon ANDO	AFOSR-77-3303

9. PERFORMING ORGANIZATION NAME AND ADDRESS	10. PROGRAM ELEMENT, PROJECT, TASK AREA & WORK UNIT NUMBERS
University of Toronto Institute for Aerospace Studies 4925 Dufferin St., Downsview, Ont. M3H 5T6, Canada	61102F 2307/A3

11. CONTROLLING OFFICE NAME AND ADDRESS	12. REPORT DATE
Air Force Office of Scientific Research/NA Bldg. 410, Bolling Air Force Base, DC 20332	April 1981
	13. NUMBER OF PAGES 131

14. MONITORING AGENCY NAME & ADDRESS(if different from Controlling Office)	15. SECURITY CLASS. (of this report)
	Unclassified
	15a. DECLASSIFICATION/DOWNGRADING SCHEDULE

16. DISTRIBUTION STATEMENT (of this Report)

Approved for public release; distribution unlimited.

17. DISTRIBUTION STATEMENT (of the abstract entered in Block 20, if different from Report)

18. SUPPLEMENTARY NOTES

19. KEY WORDS (Continue on reverse side if necessary and identify by block number)

1. Pseudo-stationary oblique shock-wave reflections; 2. Perfect and real-gas flows; 3. Shock-tube flows; 4. Interferometric measurements; 5. Optical flow-visualization

20. ABSTRACT (Continue on reverse side if necessary and identify by block number)

The transition boundaries for a triatomic gas between various types of shock-wave reflection configurations - regular reflection (RR), single Mach reflection (SMR), complex Mach reflection (CMR), and double Mach reflection (DMR) - exhibited by a plane shock impinging on a compressive corner in a shock tube were studied experimentally using CO_2 as the test gas. The shock Mach numbers ranged from 1.8 to 10.2, and the initial pressure from 3.5 to 80 torr at room temperature. The regions corresponding to the four types of

reflection were obtained in terms of the shock Mach number M_S and the wedge angle θ_w. Excellent agreement was found between analysis based on a perfect-gas model with $\gamma = 1.290$. Poorer agreement was found for complete and partial equilibrium models. The resultant transition map in the $M_S - \theta_w$ plane will be of value to future researchers in the field as an aid in designing their experiments.

The density contours of the flow fields were obtained by means of infinite-fringe interferograms, some of which, particularly those of CMR and DMR, were hitherto unavailable in the literature. They may prove valuable for comparison with the results of numerical simulation of the phenomena, which is currently the subject of intense research at various institutions.

Qualified requestors may obtain additional copies from the Defense
Documentation Center, all others should apply to the National Technical
Information Service.

Conditions of Reproduction:

Reproduction, translation, publication, use and disposal in whole or in
part by or for the United States Government is permitted.

Approved for public release; distribution unlimited.

Accession For	
NTIS GRA&I	☒
DTIC TAB	☐
Unannounced	☐
Justification	
By	
Distribution/	
Availability Codes	
Dist	Avail and/or Special
A	

PSEUDO-STATIONARY OBLIQUE SHOCK-WAVE REFLECTION

IN CARBON DIOXIDE -- DOMAINS AND BOUNDARIES

by

Sanon Ando

Submitted March 1981

Acknowledgements

Summary

The transition boundaries for a triatomic gas between various types of shock-wave reflection configurations--regular reflection (RR), single Mach reflection (SMR), complex Mach reflection (CMR), and double Mach reflection (DMR)--exhibited by a plane shock impinging on a compressive corner in a shock tube were studied experimentally using CO_2 as the test gas. The shock Mach numbers ranged from 1.8 to 10.2, and the initial pressure from 3.5 to 80 torr at room temperature. The regions corresponding to the four types of reflection were obtained in terms of the shock Mach number, M_s, and the wedge angle, θ_w. The resultant transition map in the $M_s - \theta_w$ plane will be of value to future researchers in the field as an aid in designing their experiments.

Excellent agreement was obtained between the transition boundary from CMR to DMR according to the criterion proposed by Ben-Dor & Glass (7a, b) that the flow downstream of the reflected shock should be sonic relative to the kink of the reflected shock for the transition to occur and the results of the present experiments. This fact will further confirm the validity of their criterion.

The density contours of the flow fields were obtained by means of infinite-fringe interferograms, some of which, particularly those of CMR and DMR, were hitherto unavailable in the literature. They may prove valuable for comparison with the results of numerical simulation of the phenomena, which is currently the subject of intense research at various institutions.

The analysis of shock-polar diagrams for the present experiments appear to cast doubts on the validity of the hypothesis made by Henderson & Lozzi (29) that an apparent RR beyond the von Neumann criterion was actually a nascent DMR which was too small to be identified as such.

It seems reasonable to conclude from the results of the present experiments and of Ben-Dor & Glass (7a, b) that a perfect-gas model with an appropriate constant γ should be used in determining the transition angles between various types of shock reflection for shock Mach numbers at least up to 10, which is the upper limit of the present experiments.

TABLE OF CONTENTS

Notation

CMR   complex Mach reflection

DMR   double Mach reflection

E   intersection point of the extension of the slipstream and wedge surface, see Fig. 21a

h   enthalpy

I   incident shock

K   kink of the reflected shock, or Gladstone-Dale constant

L   horizontal distance between the triple point and the vertex of the wedge, or the depth of the test section of the shock tube

ℓ horizontal distance between the triple point and the kink of the reflected shock, or relaxation length

M   Mach number, or Mach stem

MR   Mach reflection

P   pressure, the reflection point, or a point in the plane

R   reflected shock

RR   regular reflection

S   sonic point, or slipstream

T   temperature, or triple point

t   time

u   flow velocity in the stationary frame of reference

w   velocity of the triple point relative to E

x   x-coordinate in the physical plane

y   y-coordinate in the physical plane

Z   molecular weight ratio

Δ difference of the predicted and measured value

γ specific heat ratio

η = y/t

θ flow deflection angle, or an angle

λ wavelength of the light source

ξ pressure ratio across the shock $(=P_0/P_1)$, or = x/t

ρ density

σ intersection of the I-polar and the P-axis

τ relaxation time

ϕ, Φ wave angle

χ trajectory angle of the triple point

ψ $= \pi - (\chi + \theta_3)$, i.e. the angle subtented by the slipstream and the wedge surface at their intersection, see Fig. 21a

ω angle of reflection

Subscripts

a   ahead of the shock

b   behind the shock

D   the detachment criterion

N   the von Neumann criterion

s   shock

v   vibration

w   wedge

0,1,2,3   regions defined by Figs. 5a, 11a, 15a, and 21a

Superscripts

'   "secondary," "effective," or relative to the reflecting surface

*   measured quantity

1. INTRODUCTION

When a plane shock wave impinges on a sharp wedge, it exhibits different patterns of reflection, depending on the strength of the shock and the angle of incidence. The reflection patterns may be broadly divided into two types: regular reflection (RR) and Mach reflection (MR). The latter may further be divided into three subvarieties: single Mach reflection (SMR), complex Mach reflection (CMR), and double Mach reflection (DMR) (see Fig. 1).

The shock transition between various types of reflection patterns has been studied extensively in the past not only as an important gasdynamic phenomenon per se, aiming at understanding the nature of reflection, refraction, and diffraction of shock waves, but also for its implications and utilities for military purposes, such as the prediction of shock loading on structures and optimal heights of burst for weapons [see e.g., Glass (22)]. Although the studies have predominantly been, and still are, concerned with the transition between RR and MR, the interest in the transition criteria among other types of reflection has been increasing in recent times; especially with the advent of sensitive pressure transducers, some insight into the flow properties behind the reflected shock, which are perhaps of the most practical significance, has been obtained [Merritt (45), Bazhenova et al (4), Bertrand (13)].

The objectives of the present studies are:

1) To delineate the regions corresponding to various types of reflection in carbon dioxide, in terms of the shock Mach number M_s and the actual wedge angle θ_w.

2) To investigate the nature of the secondary Mach shock* which characterizes DMR.

3) To study the density distribution of the flow field by means of infinite-fringe interferograms.

The present study is a direct continuation of the work by Ben-Dor & Glass (7a,b) who studied the transition criteria of shock reflection in nitrogen and argon, extending the work of Law & Glass (43).

The transition boundary maps depicting the regions of RR and MR have appeared in previous works: e.g. Courant & Friedrichs (19), Bleakey & Taub (14), Polacheck & Seeger (50), Syschikova & Krassovskaya (60). Bazenova et al. (3) were the first to attempt to delineate the regions corresponding to other types of reflection than those of RR and MR. With the aid of pressure transducers embedded in the reflecting surface, they obtained over a limited range of shock Mach number the transition boundary between CMR and DMR experimentally. Ben-Dor & Glass (7a,b) proposed a new criterion for the transition from CMR to DMR that the flow behind the reflected shock be sonic with respect to the kink of the reflected shock, and delineated the regions for four known types of reflection — RR, SMR, CMR, and DMR — for perfect and equilibrium nitrogen and argon over the shock

---

*See Sec. 2.2.3 for the description of the secondary Mach shock.

Mach number range from 1.0 to 8.0

The θ - P/P_0 shock-polar diagram is provided for every photograph of the present experiments included in this report so as to afford an overall perspective of the phenomena under investigation, which is not visible in the photograph. For example, the shock polars corresponding to the incident and reflected shocks, or the I- and R-polars, together with the Mach numbers of the oncoming flows to the respective shocks, visualize all the states achievable downstream of the shocks in terms of the two parameters, the pressure ratio across the shock P/P_0 and the flow deflection angle θ. Moreover, one of more intersections of the I and R-polars are the possible solutions of the two-shock and three-shock relations, so that the actual states of the angular regions around the confluence point of the shocks seen in the photograph are indeed represented by one of the intersection points.

It should be borne in mind that these θ - P/P_0 shock-polar diagrams are the pictorial representations of the two-shock and three-shock interactions in the frame of reference with its origin attached to the confluence point of the shock, in which the shocks are thus made stationary.

2. CLASSIFICATION OF TYPES OF SHOCK REFLECTION

As our major objective is to delineate the regions corresponding to various types of reflection configurations in pseudo-stationary flow, in terms of the shock Mach number and the actual wedge angle, it is desirable to have precise ideas of what is meant by regular, single Mach, complex Mach, and double Mach reflections (Fig. 1) and how they are determined.

2.1 Regular Reflection

Referring to Fig. 2a, when the wave angle ϕ_0 is sufficiently small, the intersection point P of the incident shock I and the reflected shock R occurs on the wall, and moves along the wall surface. In a coordinate system attached to P, the initial flow u_0 along the wall is deflected toward the wall by the incident shock, and the deflected flow u_1 generates the reflected shock R which turns the flow u_1, so that u_2 is again parallel to the wall. Except for one particular value Φ_0 of the wave angle, however, the reflection is not specular, i.e. the angle of reflection ω is not equal to the wave angle ϕ_0. (The value of Φ_0 is 39.2^0 for $\gamma = 1.4$, and 40.3^0 for $\gamma = 1.29$.) For ϕ_0 greater than Φ_0, ω is greater than ϕ_0; and for ϕ_0 smaller than Φ_0, ω is less than ϕ_0 [see Polachek & Seeger (50)].

In the coordinate system attached to the reflection point P (the intersection point of the two shocks and the wall), the flow configuration is made stationary, so that the simple two-shock theory [von Neumann (61), Bleakney & Taub (14), Polachek & Seeger (50)] may be used to find the flow properties of the angular regions around P. Since the velocity with which P moves along the wall is very high for small values of wave angle ϕ_0, the flow u_2 behind the reflected shock R is in general supersonic relative to P, except for the narrow range of ϕ_0 between the detachment angle (the

2

limiting wave angle beyond which RR is not possible according to the detachment criterion, see Sec. 3 below, and the sonic angle (the wave angle at which u_2 is just sonic relative to P), over which u_2 is subsonic.* The sonic angle is also referred to as the catch-up angle, since the sonic pulse from the corner can catch up to P at this wave angle. As can be seen from the wave angle-flow deflection angle diagrams in Fig. A2 in Appendix A, the sonic angle is 3° to 4.5^O smaller than the detachment angle for $M_0 \lesssim 2$, and the difference quickly decreases with the increases in M_0.

If the flow u_2 behind the reflected shock is supersonic with respect to the reflection point P, the sonic signal from the corner cannot reach P, so that there will be a region behind R in which the thermodynamic state of the gas is uniform; as a result, the segment of R delineating this region is straight.

Figure 2b is the flow-deflection angle-pressure ratio shock polar diagram of regular reflection as depicted in Fig. 2a. Sonic points, S_1 of the I-polar and S_2 of the R-polar, represent the condition that the flows behind the incident shock I and the reflected R, respectively, are just sonic. Thus, a sonic point divides the polar into two branches, one lying below it (usually referred to as the weak branch), along which the flow behind the shock is supersonic, and the other lying above it (usually referred to as the strong branch), along which the flow behind the shock is subsonic. Note that the R-polar meets the P-axis below the intersection point σ of the strong branch of the I-polar and the P-axis, and that there are consequently only two possible solutions, denoted by points 2 and 2' in Fig. 2b. Although a rigorous theoretical proof is yet to be given, it has amply been demonstrated experimentally in the past that, in case two points equally satisfy the boundary condition that $\theta_1 + \theta_2 = 0$, where θ_1 and θ_2 are the flow deflection angles in the regions behind the incident and reflected shocks, respectively, it is always the one on the weak branch that is actually observed. With solution point 2' thus eliminated as physically unlikely, point 2 is the only possible solution. Thus, physical state of the region behind the reflected shock seen in the shadowgraph of a typical RR in Fig. 3a is represented by solution point 2 in Fig. 3b.

However, as will be explained in detail in Sec. 3 below, there are two conflicting criteria—usually referred to as the von Neumann and detachment criteria—concerning the transition from RR to MR. As a result, classification of the reflection type becomes subject to debate in the case where the R-polar meets the P-axis above the intersection σ of the I-polar and the P-axis, see Figs. 4b, 5b, and 6b; for then, excluding solution point 2' which is not physically meaningful, there now exist two possible solutions denoted by 2_N (N for Neumann criterion) and 2_D (D for detachment criterion). According to the von Neumann criterion, the reflections in Figs. 4a, 5a, and 6a are Mach reflection, while according to the detachment criterion, they are still regular reflection, so that the states of the regions behind the reflected shocks (and the Mach stems in the case of the von Neumann criterion) are represented by 2_N and 2_D respectively, in Figs. 4b, 5b, and 6b.

To the accuracy of the resolution (0.2mm) of the interferograms

---

*See, e.g., Fig. 6 of Bleakney and Taub (14).

in the present experiments, reflections in Figs. 4a, 5a, and 6a are regular. (For further discussion, see Sec. 3.)

2.2 Mach Reflection

As the wave angle ϕ_0 is increased, the intersection point of the incident and reflected shock occurs off the wall, and is connected to the wall by a third shock M (see Fig. 7). The resultant irregular reflection configuration is called Mach reflection, and the third shock is referred to as the Mach stem.

Since the confluence consisting entirely of three shocks is impossible in a two-dimensional flow [Courant & Friedrichs (19), Breed (17)], there is always a fourth discontinuity S in the flow, across which entropy, density, temperature, and flow velocity are discontinuous, but pressure and the flow direction are continuous, and is referred to as the slipstream, contact discontinuity, or vortex sheet. The confluence point T of the four discontinuities is called the triple point.

2.2.1 Single Mach Reflection

This configuration occurs when the flow u_2 behind the reflected shock R is subsonic relative to the triple point T, and is identified by the curved reflected shock over its entire length up to T (see Fig. 8a).

This configuration is always observed when the incidence is near glancing ($\phi_0 \simeq 90^{\circ}$). In general, in the case of SMR, the flow angles to the incident shock and the Mach stem differ only slightly, and hence the reflected shock is weak. As a result, it is difficult to pinpoint the triple point T exactly and to determine the shock angles at T.

In most cases, the shock angles at T are measured by a conventional protractor or some modification thereof; however, it is interesting to note that Kawamura & Saito (40) determined the slopes of the shocks by differentiating the 5th-order polynomials approximating the traced images of the shocks.

Figure 8b shows an example of the shock polars for SMR, which is characterized by the intersection point of the I- and R-polars occuring on the subsonic branch of the R-polar. Thus, the flow u_2 behind the reflected shock R is subsonic relative to the triple point T. Figure 9a shows the finite-fringe interferogram of SMR. In general the flow u_1 behind the incident shock I is only slightly above sonic in SMR, so that the reflected shock tends to be nearly normal to u_1. In the shock polar diagram, this fact is manifested by the smallness of the R-polar in Fig. 9b, for which $M_1 = 1.05$. Note the minute R-polar near the sonic point S_1 of the I-polar.

At the limiting flow angle, or the "extreme sonic angle" [Smith (56)], the R-polar degenerates to a point at the sonic point S_1 of the I-polar; and a reflected shock is no longer possible beyond this limit, inasmuch as no stationary shock can exist in subsonic flow. This means that, in the polar diagram, no R-polar can be drawn in the strong branch of the I-polar where the flow is subsonic.

4

Almost laminar isopycnics along the reflected shock in Fig. 10a show in the most striking manner that the expansion wave which appears in the middle of the reflected shock envelope in the density contours obtained numerically by Schneyer (51) (see Fig. C-3c in Appendix C) is indeed "spurious" as Schneyer himself remarked. The isopycnics in Fig. 10a are evaluated in Fig. 10c, using the frozen-gas relations with $\gamma = 1.290$. Figure 11 illustrates the superposition method for evaluating band displacement for the case comparative to Fig. 10a.

2.2.2 Complex Mach Reflection

When the flow u_2 behind the reflected shock R is supersonic relative to the triple point T, R is made straight at T [Kawamura (39)]. The resultant Mach reflection configuration (Fig. 12a) with a straight reflected shock R at the triple point T is referred to as complex Mach reflection to distinguish it from single Mach reflection which has a curved reflected shock over its entire length.

It should be borne in mind that there is nothing intrinsically "complex" about this type of reflection in particular, as the term may imply. Because of the straight reflected shock in CMR and DMR, the flow around the triple point is uniform and indeed simpler in CMR and DMR than in SMR where the curvature of the reflected shock R inevitably introduces non-uniformity in the flow behind R.

Figure 12b is a typical shock polar diagram of CMR, which is identified by the intersection of the I- and R-polars occuring in the supersonic branch of the R-polar; so that the flow behind the reflected shock is supersonic relative to the triple point. The smaller the wedge angle, the closer the angle of incidence to the extreme sonic angle, and hence the closer the R-polar to the sonic point S of the I-polar.

For lower range of M_s, the transition from the straight shock R to a curved bow wave may take place smoothly without a so-called kink K shown in Fig. 12a. Figure 13a illustrates such a case. As M_s is increased, the juncture of R and the curved bow wave becomes more and more pronounced as can be seen in the subsequent photographs. Note the Mach waves along the wedge surface in Fig. 13a, which are generated at the very fine machining striation on the reflecting surface. The density of each isopycnic in Fig. 14a is evaluated in Fig. 14c, using the frozen-gas relations with $\gamma = 1.290$. Figure 15a is a shadowgraph of complex Mach reflection. The two plumb lines visible in this and other photographs are 1.0 cm apart. The dark spots visible in the region behind the curved bow wave, one large and blurred, and the other small and distinct, were owing to superficial damages on the lenses of the interferometer and the test-section window glass. Figure 15c shows the Mach numbers of the flow along the reflecting surface, measured by means of the Mach waves enamating from the reflecting surface. Considering the foot of the Mach stem to be normal to the wedge surface, the Mach number of the induced flow immediately behind it was calculated using the three-shock theory, and the predicted value 1.88 is in excellent agreement with the measured value 1.9. The sudden increase in the flow Mach number downstream of the Mach stem is due to the clockwise

vorticity of the flow caused by the interaction of the flow along the wedge surface and the flow along the slipstream which curls up near the wedge surface. The turbulent nature of the slipstream is clearly visible in Fig. 15a. As shown in Figs. 16 and 17, as the wedge angle decreases, the angle between the oncoming flow and the incident shock I increases, causing the flow velocity behind I to decrease. Thus, the R-polars in Figs. 16b and 17b are located close to the sonic points S_1 of the I-polars. It will be noticed in the preceding photographs (Figs. 14a through 17a) that the kink K becomes more and more pronounced as M_s increases.

2.2.3 Double Mach Reflection

This type of Mach reflection (see Fig. 18a), first reported by White (64) in 1952, is characterized by an appearance of a new shock M', which we shall call the secondary Mach shock*, emanating from the kink of the reflected shock. Consequently, there exist two systems of the three-shock interactions in the flow, hence the term double Mach reflection. And the kink now becomes the secondary triple point T'.

For lower shock Mach numbers, M' extends only a short distance away from T', as can be seen in Fig. 19a which shows a nascent secondary Mach shock M'. As well, in Fig. 19a, the derivative of the slope of the shocks at T' appears to be still continuous, and the entire straight segment of the primary slipstream S is distinctly visible as the centre of the vorticity of the flow at the juncture of S and the reflecting surface is some distance away from S, but its influence is strong enough to cause the Mach stem to slightly bulge upstream. The reflected shock R from the primary triple point T in Fig. 19a is almost parallel to the trajectory path of T, inclined at the angle χ to the reflecting surface (Fig. 18a). In Fig. 20a, weak though it may be, a spoon-shaped M' spans between T' and the primary slipstream S, intersecting the latter almost perpendicularly. The image of M' at T' appears as though M' were the appendage of the curved bow wave, no change in the shapes of the two shocks being discernible. A sudden change of the shape of M' near S, as a result of which M' has a trowel-like appearance, may be construed as an indication of complexity of the flow downstream of the reflected shock R. The image of the primary slipstream S becomes progressively ill-defined beyond the half-length, illustrating the fact that the shear flow along S near the primary triple point T turned into turbulence.

Photographs in Figs. 21a through 24a were taken using the same wedge of 27° semi-vertex angle, and are in the increasing order of M_s so as to visualize the corresponding gradual growth of M'. Figures 21a shows an incipient M'. (Dark images near the reflecting surface are due to the smudges on the test-section window.) Figure 22a distinctly shows the nature

---

*This terminology was chosen so that each shock in the flow field may be uniquely referred to, even though it differs from the system of reference adopted by Ben-Dor & Glass (7a,b) who considered the new shock under discussion as the secondary reflected shock R_1 by drawing analogy between the gasdynamic discontinuities I, R, M, S and R, R_1, M_1, S_1, respectively, see Fig. 18c.

of turbulence along S. Because M' is very weak, the secondary slipstream is entirely invisible, even though its existence is guaranteed theoretically as previously mentioned. In Fig. 23a, M', smooth and distinct, connects T' and S, meeting S somewhat obliquely. (Again, the smudges on the window are visible.) To the accuracy of the resolution of the photograph, the derivative of the slope of the shock envelope at T' is continuous.

With further increases in M_s, M' becomes more and more straight, and its intersection point with S shifts downstream towards the reflecting surface as evident in Fig. 24a. Figures 25a through 32a show cases of strong to very strong incident shocks. In Fig. 25a, the curvature of M' appears to be concave downstream, while, in the previous photographs, it is concave upstream. The intersection of M' with S occurs nearly at the extreme position relative to S, i.e. near the reflecting surface. The angle ω between the reflected shock R and the trajectory path of the triple point T, or the angle of reflection (see Fig. 18a), is now "negative"; that is to say, R is located below the trajectory path. Visible in the shadowgraph of Fig. 25a is the secondary slipstream S' enamating from T'. Note the crescent image in the lower part of the Mach stem M. This is a manifestation of the three-dimensional character of the bulge of M as explained below, since its effect is more apparent in the later photographs. As in Fig. 20a, S becomes less and less visible along its length, indicating the gradual transition from shear flow to turbulence along S. A large curling of S near the reflecting surface observable in the previous photographs has drastically diminished its size. The gray furrow-like image along the reflecting surface behind the curved bow wave is the boundary layer, enhanced by the minute striations--from which Mach waves are generated-- on the surface. Figure 26a confirms the observation made earlier, i.e. M' is strongest at T'. This is borne out by the fact that the isopycnics of M' become denser towards T'. A high degree of compression of the gas near the foot of the slipstream S is made manifest by the cluster of dense isopycnics. No signs of the secondary slipstream are evident. Note the disturbance immediately ahead of the curved bow wave. This disturbance, the cause of which is yet to be investigated, appears quite distinctly in some interferograms, not only of the present experiments (Figs. 27a, 28a, and 29a below, for example), but also in an interferogram in CO_2 included in Law & Glass (43) who used the same apparatus as in the present case. A remarkable fact is that it is only in CO_2 that the disturbance is evident, and not in any other types of gases. The density contours such as shown in Fig. 27a makes one wonder whether some extraneous disturbances are influencing the flow behind the curved bow wave. Figure 27a shows the flow downstream of the Mach stem M surging up from the reflecting surface along the vortex of the slipstream toward M. This is the flow that causes M to bulge near its foot. The density of each isopycnic in Fig. 27a is evaluated in Fig. 27c, using the frozen-gas relations with $\gamma = 1.290$, and the results obtained by the finite-fringe method by Ben-Dor & Glass (7a,b) for comparable cases in N_2 as the guide. The values for ρ/ρ_0 assigned to the isopycnics in the region inside the curved bow wave appear to be rather large. This resulted from the fact that the variation in density between two consecutive isopycnics in an infinite-fringe interferogram is known (see Appendix C), and the fact that the values for ρ/ρ_0 increase steadily toward downstream according to the isopynics in Ref. 7a,b. Figures 28a

through 31a are of the experiments using the identical wedge of 30° semi-vertex angle. (The Mach waves emanating from the reflecting surface are particular to this wedge.) Due to the constraints on the experimental set-up, the initial pressures are lower for large M_s. As noted above, Figs. 28a and 29a show the disturbance immediately ahead of the curved bow wave. No trace of the secondary slipstream is discernible in either figure. In Fig. 29a, the bulge of M can be examined in detail. The clockwise flow along the vortex associated with the slipstream S interacts with the induced flow behind M; as a result, a part of M is "pushed" upstream, causing a bulge. In Fig. 29a, the bulge is seen to be three-dimensional in the sense that the extent of the departure from the planarity of the front is more severe in the region near the centre-plane of the shock tube than near the window, as a close examination of the profile of M will show. (In Fig. 25a above, one sees the early stage of this effect.) In Figs. 30a and 31a, the concentric rings of isopycnics indicative of the vorticity associated with the slipstream S are no longer visible; the slipstream appears L-shaped, instead. The number of isopycnics visible in either interferogram is less than in the previous ones, due to the decrease in the initial density. Figure 32a shows the highest M_s achieved in the present experiments (M_s = 10.17), which also results in DMR. The bulge of M appears two-dimensional in this case. Note the somewhat peculiar shapes of isopycnics downstream of M, indicating the complexity of the flow field. The density of each isopycnic in Fig. 32a is evaluated in Fig. 32c, using the frozen-gas relations with $\gamma = 1.290$.

It is not possible to distinguish between CMR and DMR on the basis of the shock polar diagrams, since the flow behind the reflected shock is supersonic in either case.

3. TRANSITION FROM RR TO MR

As mentioned in Sec. 2.1 above, there are two main criteria for the transition from RR to MR. One, attributed to von Neumann (61), requires that, when the flow angle to the incident shock is increased while maintaining the shock strength constant, the changes in the pressures in the regions around the confluence point of the shocks should also be gradual at transition from RR to MR. In other words, the regions will remain in "mechanical equilibrium" during the transition. According to this criterion, therefore, the pressure in the region immediately behind the reflected shock at the confluence point will not suffer a sudden drop when the transition occurs, the phenomenon predicted by the detachment criterion discussed below. [This is most easily understood by examination of the flow deflection angle - pressure ratio (θ - P/P_0) shock polar diagrams, see Figs. 4b, 5b, and 6b, and also Fig. 2 of Hornung et al (32).] The required condition is realizable only in the so-called stationary Mach reflection configuration (Fig. 33) in which the slipstream is parallel to the wall and the Mach stem is perpendicular to the oncoming flow [von Neumann (61), Courant & Friedrichs (19)]. Thus, one of the boundary conditions in this configuration is that the flow deflection suffered through the incident shock be exactly compensated by the re-deflection through the reflected shock.(See Refs. 19, 50, 61 for further discussion.)

The other, usually referred to as the detachment criterion, which is put forward by standard textbooks on gasdynamics such as Liepmann & Roshko (44), specifies that the transition from RR to MR occurs when the flow deflection angle θ_1 through the incident shock exceeds the maximum flow deflection angle θ_2 through the reflected shock. The flow angle ϕ_0 to the incident shock corresponding to the von Neumann criterion is less than that corresponding to the detachment criterion over the entire range of shock strength, except at one critical point at which the two values coincide, see Fig. 34a. (Note that the effective wedge angle θ_w' in Figs. 34a-e, which is the sum of the actual wedge angle θ_w and the trajectory angle χ of the triple point, is the complement of the flow angle ϕ_0 to the incident shock, i.e. $\theta_w' = \pi/2 - \phi_0$).

In addition to the above two main criteria, a third one, which may be termed the sonic criterion, has been suggested [see, e.g. Kawamura & Saito (40)] according to which the transition from RR to MR is expected to occur at the sonic angle, the angle of incidence at which the flow behind the reflected shock is just sonic relative to the reflection point. The underlying argument is that, when the flow behind the reflected shock is subsonic, the corner signal can reach the reflection point P causing disturbances in the entire flow downstream of P, and the transition to MR is set off as a result, since by assuming the MR configuration, the flow is relieved of the high pressure behind the reflected shock and hence is more "stable" than just prior to the transition [see e.g. Jahn (35)].

However, owing to the proximity of the sonic and the detachment angles, it is not possible to resolve these two points experimentally.

In the region in the angle of incidence-shock strength plane, or the ϕ_0 - ξ plane (or equivalently in the M_s - θ_w' plane, as done in this study), overlapped by two boundaries corresponding to the von Neumann and detachment criteria, either type of reflection, RR or MR, is theoretically possible. So far as strong shocks are concerned, however, the results of shock-tube experiments by Smith (56), Bleakney & Taub (14), Kawamura & Saito (40), Henderson & Lozzi (29), Hornung & Kychakoff (31), Ben-Dor & Glass (7a,b), and others have given evidence in support of the detachment criterion, while the experiments by Hendorson & Lozzi (29), Hornung & Kychakoff (31), and Hornung et al (32) appear to confirm the von Neumann criterion in the case of stationary flow.

In light of this apparent inconsistency of the transition criteria between the two types of flow, Henderson & Lozzi (29), and later, Syshchikova & Krassovskaya (60), postulated that the transition from RR to MR occurred at the boundary corresponding to the von Neumann criterion, and that the apparent RR beyond that limit was actually a nascent double Mach reflection that was too small to be identified.

On the other hand, Hornung et al (32) suggested an explanation for the well-known persistence of RR beyond the limit predicted by the detachment criterion in terms of the displacement thickness of the boundary layer at the reflection point in pseudo-stationary flow. (We note that

this suggestion is, however, not without difficulty; for as mentioned in their paper, previous experiments by one of the authors had shown an increase in the angle of reflection, while the proposed displacement effect of the wall should have resulted in a decrease.)

Thus, there exist two opposing views regarding the persisted regular reflection: according to Henderson & Lozzi (29), it is a nascent double Mach reflection, while Hornung et al (32) claim that it is still a regular reflection.

On the basis of the appearance in the photographs, a series of present experiments done by using a wedge of 50.4° semi-vertex angle (three of which are shown in Figs. 4, 5, and 6) have been classified as regular reflection. According to the hypothesis of Henderson & Lozzi (29), however, they are all double Mach reflection; and the states behind the reflected shock and Mach stem map into the point 2_N in the accompanying shock polar diagrams. (The point 2_D corresponds to regular reflection.)

According to our three-shock solution for $\gamma = 1.290$, the flow angles ϕ_3 to the Mach stems corresponding to the point 2_N in Figs. 5 and 6 are 88.5° and 87.5°, respectively. Hence, if one assumes that

$$\chi = 90^{\circ} - \phi_3$$

then the predicted angles χ of the triple point trajectory will be 1.5° and 2.5°, respectively, and therefore, the Mach stem should definitely be observable.

The two-shock theory gives two values for the angle of reflection ω for given shock strength ξ and angle of incidence ϕ_0; the higher value is termed the strong solution and the lower one the weak solution, and it is the latter that is usually observed in practice. The two solutions coincide at a critical angle of incidence, or the extreme angle, beyond which no solutions exist. Polacheck & Seeger (50) for example, show that the solution curves of the two-shock and three-shock theories for a given shock strength ξ in the $\phi_0 - \omega$ plane intersect at a single point. The particular value of ξ for which this intersection point coincides with the extreme angle of the two-shock curve is the critical shock strength that separates the two classes of shocks, weak and strong. [As shown by Polacheck & Seeger (50), this occurs at $\xi = 0.433$ and $\phi_0 = 41.4^{\circ}$ for $\gamma = 1.4$.] Kawamura & Saito (40)* found that in the case of strong shocks, the transition from RR to MR was accompanied by a sudden decrease in the angle of reflection ω while the transition was smooth and the angle of reflection increased continuously in the case of weak shocks.

---

*There has been a certain amount of uncertainty concerning the numerical values of the parameters cited in Kawamura & Saito's paper, stemming mainly from an apparent misprint of the value of the Mach number of the incident flow. Molder (48) recently recalculated these quantities for $\gamma = 7/5$ and $5/3$, maintaining seven significant digits.

Here we disagree with Henderson & Lozzi (30) who interpreted Kawamura & Saito's findings to be the "ω_N [the von Neumann criterion] was the criterion for strong shocks and the ω_e [the detachment criterion] was the one for weak shocks". As evident from the inspection of the ϕ_0-ω planes or the θ-P polar diagrams, the transition from RR to MR according to the von Neumann criterion must be smooth without a discontinuous change in the angle of reflection, while the detachment criterion predicts a sudden drop in the angle of the reflection at the transition. Thus, the results of strong-shock experiments by Kawamura & Saito are reconcilable only with the detachment criterion.

4. TRANSITION FROM CMR TO DMR

Law & Glass (43)* suggested that DMR occured when the flow u_2 (see Fig. 8) behind the reflected shock R was supersonic relative to the wedge surface. Gvozdeva et al (26) suggested that the DMR configuration was brought about as a result of the excitation of the internal degrees of freedom of the gas molecules behind the shocks. Semenov et al (53) proposed that the inception of the secondary Mach shock M' (Fig. 21a) was due to the rotational flow which developed in the region between the primary Mach stem M and the reflected shock R and caused the primary slip-stream S to curl up into a vortex. Gvozdeva et al (26) and Bazhenova et al (4) measured the pressure on the reflecting surface of the wedge by using piezo-gauges and found that their results concerning the inception of DMR did not agree with the criterion suggested by Law & Glass (43). They considered that the flow u_2 behind the reflected shock R to be supersonic with respect to the primary triple point T as the necessary (but not sufficient) condition for DMR, and suggested that the appearance of the second increase in pressure on the reflecting surface from the oscillo-graphic trace as a way to distinguish DMR from other types of Mach reflec-tion. We remark, however, the difference in sensitivity between the optical method and the pressure-transducer method of data acquisition. Figure 19 is a case in point; while a nascent secondary Mach shock is clearly visible in the shadowgraph, it is doubtful if it will make its presence known to the pressure transducer on the reflecting surface, which after all is capable of registering only the integrated pressure over the area of its pressure-sensitive surface.

Thus, it seems natural that the two boundaries determined experimentally by an optical method and a pressure-transducer method should disagree. Ben-Dor & Glass (7a,b) suggested that the transition from CMR to DMR occurred when the flow u_2 behind the reflected shock R (see Fig. 12a)

---

*In the paper cited, Law & Glass acknowledge the suggestion made to them by Dr. L.G. Gvozdeva of the Institute of High Temperature, Moscow, U.S.S.R. as the basis of their criterion.

was supersonic with respect to the kink K of R. They compared the predicted regions of various types of reflection in the M_S - θ_w' plane, where M_S is shock Mach number and θ_w' the "effective wedge angle" (the sum of the wedge angle θ_w and the angle χ of the triple-point trajectory), with experiments using argon and nitrogen over the range of M_S from 1.9 to 8. The results for N_2 are shown in Fig. 53 of Ben-Dor (6) and Fig. 18 of Ben-Dor & Glass (7a). In spite of an apparent agreement of data points with the predicted regions corresponding to equilibrium nitrogen as shown in the two figures, if one plots the data for the experiments in N_2 listed in Table 5 of Ben-Dor (6) onto the M_S - θ_w' plane in Fig. 23 of the same report, one will notice that there are some points that fall into the regions overlapped by the two boundaries corresponding to a perfect diatomic gas $\gamma = 1.4$ and to equilibrium nitrogen (e.g. Exp. #33, 42, 43, 44, 45, 46 of Ref. 6). The reason for the fact that the experimental points now agree with the regions corresponding to a perfect gas, instead of those corresponding to equilibrium gas may be that the theory is adequate but the equilibrium-gas analysis is irrelevant for the purpose of delineating the regions since the shock waves remain frozen (Appendix E).

Since the criterion for the transition from CMR to DMR put forward by Ben-Dor & Glass (7a,b) is in terms of the Mach number of the flow behind the reflected shock with reference to the kink K which itself is moving in the laboratory frame of reference, it is necessary to find the relative velocity u of the kink with respect to some reference point, say, the triple point T. Thus, Ben-Dor & Glass (7a,b) assumed as Law & Glass (43) did that the kink K moved with the same horizontal velocity as the induced flow behind the incident shock I, so that the ratio ℓ/L, where ℓ and L are horizontal distances between T and K, and T and the vertex of the wedge, respectively, is equal to the density ratio across the incident shock irrespective of the wedge angle θ_w. This assumption, however, was proved to be invalid by Bazhenova et al (4) who measured the ratio ℓ/L in their experiments and found that for a given incident shock Mach number the ratio decreased with the increases in the wedge angle.

It is relevant here to remember that along the transition boundary between CMR and DMR (see Figs. 34 and 35), the ratio ℓ/L obviously vanishes because the triple point T and the kink K coincide, and hence $\ell = 0$, on that boundary.

In the present experiments, the measurements were made of the ratio ℓ/L for three incident shock Mach numbers 5, 7, and 8; the results are shown in Fig. 36.

In general, the pressure in regions 4 and 5 behind the bow wave (see Fig. 18a) is greater than that in regions 2 and 3 behind the reflected shock R, as evident in the pressure traces taken by Bertrand (13) or Merritt (45). It appears, therefore, that the ratio ℓ/L is in correlation with this pressure difference; with the increases in the wedge angle, the bow wave becomes more and more normal to the induced flow behind the incident shock, so that the pressure in region 4 becomes higher and the secondary triple point T' is "pushed" upstream. And the ratio ℓ/L decreases as a result.

It seems possible that this pressure difference between region 2 and 4 is a significant factor in the genesis of the secondary Mach shock M', for when the pressure difference increases, some drastic mechanism such as a shock is necessary to raise the pressure of region 2 to that of region 4. We note that in the DMR configuration, the gas in region 5 that has passed the straight reflected shock R is separated from the gas in region 4 that has passed the bow wave by the secondary slipstream S' (see Fig. 18a).

The extent to which the failure of the assumption regarding the velocity of the kink K (or the secondary triple point T') relative to the (primary) triple point T will have on the transition boundary predicted by Ben-Dor's criterion requires further analysis.

5. EXPERIMENTS

The experiments were performed in the 10 cm x 10 cm hypervelocity shock tube and its 23-cm dia plate Mach-Zehnder interferometer at UTIAS. As the detailed accounts of the structures and operation of the facilities have been described elsewhere [Boyer (16),Hall (28), and Ben-Dor & Whitten (10)], only the special considerations relevant to the present study will be included here.

The shock tube consists of a driver section 1.8-m long and a channel 12-m long, with 10 cm x 18 cm cross-section, separated by a diaphragm. Mylar polyester films of various thickness were combined and employed as diaphragms. The initial pressure ratios across the diaphragms were computed using the shock-tube relations with an adequate allowance to compensate for shock-wave attenuation effects [Boyer (16)]. Initially, the channel was evacuated by three types of vacuum pumps in series--mechanical, Roots, and diffusion pumps--down to 5 to 15 μHg. The vacuum was measured by a Pirani vacuum gauge (Type GP 140). The initial pressures ranged from 3.5 torr for high shock Mach numbers to 80 torr for low shock Mach numbers. Relatively high initial pressures were required to meet the triggering threshold of the pressure transducers, which were used for measuring the traversing velocity of the shock, as well as to maintain a reasonable degree of reprod-ucibility of shocks. Owing to air leaks into the tube and the accuracy of the vacuum gauge, the purity of the gas ahead of the shock was expected to be 0.04% to 0.4%. The commercially available carbon dioxide of purity exceeding 99.8% was used as the test gas. Carbon dioxide for weak shocks, and helium or hydrogen for strong shocks, were employed as driver gases. The initial pressure was measured by a U-tube manometer, partially filled with an oil of known specific weight, for up to 28 torr and by a Wallace & Tierman pressure gauge (Model FA 160-PP10936) for over 28 torr. Possible errors in the initial pressure do not exceed 0.8%. The whole procedure of firing a run after the isolation of the channel took 10 to 25 minutes, depending on the pressure ratio across the diaphragm. For lower Mach numbers, the reproducibility of a shock was quite good, while significant scatter proved unavoidable for higher Mach numbers.

The initial temperature of the test gas was taken to be the same as that of the shock tube at the midsection which was measured by an ordinarily mercury thermometer embedded in the tube. Measurements of the

temperature variations at the test section by the mercury thermometer placed inside the tube indicated that a temperature equilibrium inside the tube was achieved within 5 to 6 minutes after the introduction of the test gas. The shock speed was calculated from the measured traverse time between the two consecutive pressure transducers (Atlantic LD-25), 0.305m apart, situated immediately upstream of the test section.

The wedges made of steel of 1.8°, 3.8°, 10.3°, 20.3°, 27.1°, 30.1°, 40.2°, 50.4°, and 60.1° semi-vertex angles (see Fig. 37) were bolted firmly to the bottom wall of the tube at the test section. The sides of wedges were flush with the inside walls of the tube and the window glass.

Although a number of experiments were done by using 1.8° and 3.8° wedges, the results could not be used for analysis since it proved impossible to pinpoint the shock confluence point exactly on either shadowgraphs or interferograms due to the weak reflected shock (see Fig. 38a).

In the present experiments, infinite-fringe interferograms were taken to investigate qualitatively the density distribution of the flow field, and to furnish a means for a direct check on the assumptions underlying the simple theories of two-shock and three-shock interactions, such as uniformity of the flow properties in the angular regions between the gas-dynamic discontinuities at the confluence point. All four mirrors of the Mach-Zehnder interferometer were adjusted parallel to each other so that a single fringe occupied the entire field of view under a "no-flow" condition. With this arrangement, any fringe contour observed in the "flow" picture corresponds to a line of equal density, or an isopycnic (or isopycnal).

As well, the superposition method of flow and no-flow inter-ferograms to produce isopycnics was applied to some experiments (see Figs. 38b and 11a). When the two negatives of the finite-fringe interferograms corresponding to "flow" and "no-flow" conditions are superimposed, those regions where the fringes are just 180° out of phase become visible as gray strips, or isopycnics in two-dimensional flow corresponding to those observed in the infinite-fringe interferograms. However, as evident in Figs. 38b and 11a, it is extremely difficult in practice to obtain high enough contrast to make the gray strips clearly visible in the superposition pictures.

It is desirable to prepare the following four kinds of inter-ferograms of the identical experiments before drawing isopycnics of a flow field: (1) a white-light "flow" interferogram; (2) a "no-flow" finite-fringe monochromatic interferogram; (3) a "flow" finite-fringe monochromatic interferogram; and (4) a "flow" infinite-fringe interferogram. (1) determines the fringe shifts across shocks from which density at any point in the flow field may be determined by (2) and (3), while (4) provides an aid in connect-ing the points of equal density. Thus, the process demands a high degree of reproducibility of shocks, since these four interferograms should ideally be taken under the identical conditions.

For small variations of density, the infinite-fringe interferogram sometimes proves to be not sensitive enough to determine the accurate order of a fringe [Whitteman (66)].

The adjustments on the interferometer for the infinite-fringe interferograms were not without difficulty: as the four mirrors were brought to a near perfect parallel to each other, an "island" began to appear in the field owing to the minute imperfections in the optics — which are hardly noticeable in the finite-fringe interferograms — and if this "island" was successfully eliminated from the field of view, then two to three nearly parallel fringes started to appear in an extreme upper corner instead. Fortunately, however, these residual fringes were situated far removed from the critical area in the field, i.e. the vicinity of the wedge surface, their effects on the quality of the infinite-fringe interferograms were negligible; and all the infinite-fringe interferograms in the present study were taken under that condition.

The shadowgraphs were made using the same equipment but obstructing the passage of lower arm of the light path by placing a cardboard in front of a mirror.

The Control Data pulsed laser (Model 104A) was used as the light source. It provided a monochromatic light (6943$\overset{o}{A}$) of approximately 30 nsec duration; and was triggered by an adjustable delay circuit to make it possible to photograph the shock wave in the desired position. A bandpass of the identical wavelength was placed in front of the camera. If desired, it was possible to make interferograms with the second harmonic light (3472$\overset{o}{A}$) simultaneously with the fundamental mode. With this arrangement, it is possible to evaluate various effects that involve changes in refractive indeces of two constituents; for example, dissociation of diatomic gases, ionization of monoatomic gases, etc.

The interferograms and shadowgraphs were photographed by using 4" x 5" Kodak Royal X-Pan sheet films and enlarged to 1 to 3 times the actual size depending on how detailed analysis was required.

Two vertical threads 1 cm apart and one horizontal thread were placed at one side of the window nearly 2 cm away from the outer surface of the glass as the reference lines on the pictures (see Figs. 38a, 15, and 17, for example).

The Reynolds number per cm for the present experiments ranges from 5000 for lower Mach numbers to 4000 for the higher Mach numbers.

6. CO_2 — RELAXATION EFFECTS AND EQUATION OF STATE

When a polyatomic gas, initially in equilibrium, experiences a sudden compression by the passage of a shock wave, it requires a length of time to re-establish an equilibrium at a new energy level. This phenomenon is clearly observable in the finite-fringe interferograms in Figs. 4a, 5a, 6a, 9a, and 13a in the form of gradual increases in the fringe shift immediately behind the incident shock. As well, the superimposed finite-fringe interferogram in Fig. 11a shows gray bands immediately behind the incident shock and the Mach stem; and the infinite-fringe interferograms in Figs. 10a, 14a, and 16a show isopycnics in the corresponding locations. The equilibration processes between various degrees of freedom of the

15

molecules were treated by Bethe & Teller (12), who incidentally first pointed out the possibility of the fully dispersed shock wave. Kantrowitz (38) investigated the relaxation phenomena from the point of heat capacity lag using carbon dioxide as a model. Griffith et al (23) found that in CO_2 the valence vibrations adjusted at least 100 times more slowly than do the bending modes and suggested the possibility of separate relaxation times for each vibrational mode. Griffith and Kenney (24) reported the computational results on partial equilibrium state behind shock waves and the experimental results that excitation of each vibrational mode and dissociation took place at rates which differed by at least an order of magnitude so that the gas would go through a series of states of partial equilibrium. Schwartz (52) developed the relaxation equations which applied to the excitation of the lowest vibrational modes of CO_2 (doubly degenerate), and predicted direct excitation of the bending mode and indirect excitation of the valance modes, which was later confirmed by Witteman (67) in the temperature range 440° - $816^\circ K$. Johannesen et al (36) found that the relaxation frequency was not a simple function of translational temperature but depended strongly on the departure from equilibrium. Times of vibrational relaxation and dissociation behind shock waves in various diatomic and triatomic gases were measured by Gaydon & Hurle (21). Camac (18) investigated the structure of shock waves in CO_2 in the Mach number range from 5 to 25 and found that all four vibrational modes relaxed at the same rate and, that, at 4 mm per microsecond shock speed, the vibrational relaxation became comparable with the shock thickness. He found that the CO_2 vibrational relaxation time τ was given by

$$\tau = (1/P)\exp(36.5T^{-1/3}-3.9)\text{microsecond}$$

where P is pressure in atm and T in $^\circ K$. The experiments by Weihs & Manheimer-Timnat (62) showed dissociation relaxation time for CO_2 to change from 650 microsecond at $M_s = 7.5$ to about 400 microsecond at $M_s = 10$, for an initial pressure of 3mm Hg. (These happen to coincide with the upper limit of the present experiments.) Significantly, their values were about a half of those given by Gaydon & Hurle (21). The difference in the methods of measurement was considered responsible for the discrepancies. The relevant parameters of Gaydon & Hurle (21) and Weihs & Manheimer-Timnat (62) are reproduced in Table B1 of Appendix B.

Further discussion on the thermodynamic states and the proposed models of equations of state for CO_2 is included in Appendix B.

It should be remembered that, by the relaxation time is meant the time required for the departure from equilibrium to fall to 1/e, or approximately 37% of the equilibrium value, so that under the usual assumption that the approach to the equilibrium is exponential, it takes a considerable more time than those quoted in Table B1 to reach the final equilibrium where no further changes in the gas takes place.

The length of the relaxation zone in the photograph can be determined by multiplying the relaxation time in the laboratory frame of reference by the shock speed. For CO_2, in the experiments by Gaydon & Hurle (21), the vibrational relaxation length ranged from 0.3 to 3 cm and the dissociation relaxation length was approximately 25 cm, for

$M_s \approx 9$; while Weihs & Manheimer-Timnat (62) found that the dissociation relaxation length to be 12 cm at $M_s = 7.5$ and about 8 cm at $M_s = 10$. The initial pressure in all cases cited were approximately 3 torr, which compares with the present experiments.

As well, it will be recalled that the lower the shock Mach number, the longer the relaxation times, as can be observed in Fig. B4 in Appendix B. This is a direct consequence of lower temperature rises across the shocks of lower Mach numbers, and of the fact that the logarithm of the relaxation time is proportional to $T^{-1/3}$, where T is temperature [see eg. Kantrowitz (38), Camac (18)]. According to Fig. B4, the vibrational relaxation zone behind the shock extends approximately 10 cm for $M_s = 5$.

In the light of these data, and in the light of the fact that the extent of the zones of interest downstream of the incident shock, in which the shock angles are measured, is approximately 1 cm in most cases in the present experiments, it appears reasonably adequate to assume the perfect gas model with $\gamma = 1.290$ for CO_2 for the present study, the principle of which is to delineate the domains of various types of reflection with engineering accuracy.

7. PREDICTED REGIONS OF VARIOUS TYPES OF SHOCK REFLECTION AND COMPARISON WITH EXPERIMENTS

The measured parameters of each experiment in the present study are listed in Tables 1 and 2. Theoretical transition boundaries of four types of reflection (RR, SMR, CMR, and DMR) are plotted in the shock Mach number - effective wedge angle plane (the M_s - θ'_w plane) in Fig. 34*, using the five models of equation of state discussed in Appendix B. The influence of variation of γ on the transition angles are made manifest in Figs. 34a through 34e. Figure 34a is based on the perfect-gas model with $\gamma = 1.290$ (Model P), and shows an excellent agreement between theory and experiments. This indicates that it is necessary and sufficient to consider the gas perfect when calculating the transition angles.

Transition boundary 1 indicates the von Neumann criterion, and separates the M_s - θ'_w plane into two domains: in the upper domain regular reflection occurs, while in the lower domain some form of Mach reflection occurs. The detachment criterion is indicated by boundary 2, which also divides the entire plane into two domains in a like manner as boundary 1. The overlapped region between boundaries 1 and 2 indicates the domain of conflict of the two criteria, the von Neumann and detachment, and according to the former, RR is no longer possible in this region. Boundary 3 is

---

*Error bars are not shown in Fig. 34, since both θ'_w and M_s can be measured to an order of 1%.

17

drawn using the criterion proposed by Ben-Dor & Glass (7a,b) that the transition from CMR to DMR occurs when the flow downstream of the reflected shock is supersonic with respect to the kink of the reflected shock. Boundary 4 corresponds to the condition $M_2 = 1$, so that the flow behind the reflected shock is supersonic relative to the triple point T in the domain above boundary 4 and subsonic below it. Thus, according to the definition of complex Mach reflection (Sec. 5.2.2), boundary 4 delineates the domain of CMR from that of SMR. Boundary 5 indicates the limiting angles for the given M_s at which flow behind the incident steady shock (Fig. 2a) is just sonic ($M_1 = 1$), so that no solution is possible by means of the two-shock or three-shock theories in the domain below boundary 5 where the flow behind the incident shock is subsonic. This boundary is sometimes called "the extreme sonic angle" [see Smith (56)].

To the accuracy of the resolution (0.2mm) of interferograms in the present experiments, the reflections in the overlapped regions between boundaries 1 and 2 were observed to be regular (see Figs. 4-6). An excellent agreement between the predicted regions for CMR and DMR and experiments clearly confirms the validity of the criterion suggested by Ben-Dor & Glass (7a,b), when using the effective wedge angle θ_w'.

Figure 35a shows the predicted domains of various types of reflection in the incident shock Mach number - actual wedge angle plane (the M_s-θ_w plane). The actual wedge angle is obtained by subtracting from the effective wedge angle of Fig. 35 the trajectory angle χ of the triple point which is calculated by using equation 5 in Appendix D. Figure 40 shows good agreement between the predicted domains and the present experiments. Note that the boundary corresponding to the von Neumann criterion is not shown in either Figs. 35a or 35b, since the results of the present study support the detachment criterion.

8. CONCLUSION

As a continuation of the work by Ben-Dor & Glass (7a,b), who investigated the transition boundaries between various types of shock reflection in argon and nitrogen, the present study addressed itself to the case of a triatomic gas using CO_2 as the test gas. The transition boundary map in the M_s-θ_w plane (Fig. 35a), where M_s is the shock Mach number and θ_w the actual wedge angle, for CO_2, similar to those reported in Refs. 7a,b for the cases of monatomic and diatomic gases, was obtained with a view to furnish a kind of guidepost for the design of experiments in future researches. Excellent agreement between the boundaries predicted by Ben-Dor & Glass (7a,b) and the present experiments demonstrates the validity of the criteria unequivocably for perfect CO_2.

The infinite-fringe interferometry has proved an excellent means for investigating the density contours of the flow fields in CO_2. Some of the infinite-fringe interferograms taken in the present experiments, those of CMR and DMR in particular, may prove valuable when used for comparison with the density contours predicted by means of the numerical simulation of the phenomena, toward which a great deal of effort is being made at

18

various research institutions at the present moment [see, eg. Book et al (15)].

Of the various models for equation of state for CO_2, the perfect-gas model with $\gamma = 1.290$ was found to be the most appropriate one to be used in conjunction with the simple two-shock and three-shock theories over the range of shock Mach number from 1.8 to 10.2 of the present experiments.

Each of the present experiments was analyzed by means of the shock polar diagram; the results disagree with the hypothesis made by Henderson & Lozzi (29) that an apparent regular reflection beyond the von Neumann criterion was actually a nascent double Mach reflection too small to be identified as such.

In view of the fact that there are now available the shock transition maps for monatomic, diatomic (Refs. 7a,b), and a triatomic gas, the logical next step will be to obtain a similar map for air, which is perhaps of the most practical interest. This research is presently underway at UTIAS.

REFERENCES

1. Allison, D. O.   "Calculation of Thermodynamic Properties of Arbitrary Gas Mixtures with Modified Vibrational-Rotational Corrections". NASA TN D-3538 (1966).

2. Allison, D. O.
   Newman, P. A.   "Direct Calculation of Specific Heats and Related Thermodynamic Properties of Arbitrary Gas Mixtures with Tabulated Results". NASA TN D-3540 (1966).

3. Bazhenova, T. V.
   Gvozdeva, L. G.
   Labastov, Yu. S.
   Naboko, I. M.
   Nemkov, R. G.
   Predvoditeleva, O. A.   "Shock Waves in Real Gases". NASA TT F-585 (1969)

4. Bazhenova, T. V.
   Fokeev, V. P.
   Gvozdeva, L. G.   "Regions of Various Forms of Mach Reflection and its Transition to Regular Reflection". Acta Astronautica 3, 131 (1976).

5. Ben-Dor, G.
   Glass, I. I.   "Nonstationary Oblique Shock-Wave Reflections: Actual Isopycnics and Numerical Experiments". AIAA J. 16, 1146 (1978).

6. Ben-Dor, G.   "Regions and Transitions of Nonstationary Oblique Shock Wave Diffractions in Perfect and Imperfect Gases". UTIAS Rep. No. 232 (1978)

7a. Ben-Dor, G.
   Glass, I. I.   "Domains and Boundaries of Non-Stationary Oblique Shock-Wave Reflexions. 1. Diatomic Gas". J. Fluid Mech. 92, 459 (1979).

7b. Ben-Dor, G.
   Glass, I. I.   "Domains and Boundaries of Non-Stationary Oblique Shock-Wave Reflexions. 2. Monatomic Gas". J. Fluid Mech. 96, 735 (1980).

8. Ben-Dor, G.   "Analytical Solution of Double-Mach Reflection". AIAA J. 18, 1036 (1979).

9. Ben-Dor, G.   "Steady Oblique Shock-Wave Reflections in Perfect and Imperfect Monatomic and Diatomic Gases". AIAA J. 18, 1143 (1979).

10. Ben-Dor, G.
    Whitten, B. T.   "Interferometric Techniques and Data Evaluation Methods for the UTIAS 10 cm x 18 cm Hypervelocity Shock Tube". UTIAS Tech. Note No. 208 (1979).

11. Ben-Dor, G.   "A Reconsideration of the Shock Polar Solution of a Pseudo-Steady Single-Mach Reflection". CASI J. 26, 98 (1980).

12. Bethe, H. A.
Teller, E.
"Deviations from Thermal Equilibrium in Shock Waves". Eng. Res. Inst., U. of Michigan Rep. No. X-117 (1951).

13. Bertrand, B. P.
"Measurement of Pressure in Mach Reflection of Strong Shock Waves in a Shock Tube". BRL Memo. Rep. No. 2196 (1972).

14. Bleakney, W.
Taub, A. H.
"Interaction of Shock Waves". Rev. Mod. Phys., 21, 584 (1949).

15. Book, D.
Boris, J.
Kuhl, A.
Oran, E.
Picone, M.
Zalesak, S.
"Simulation of Complex Shock Reflections from Wedges in Inert and Reactive Gaseous Mixtures". Proc. 7th Internat. Conf. on Numerical Methods in Fluid Dynamics (1980).

16. Boyer, A. G.
"Design, Instrumentation and Peformance of the UTIAS 4 in. x 7 in. Hypersonic Shock Tube". UTIAS Rep. No. 99 (1965).

17. Breed, B. R.
"Impossibility of Three Confluent Shocks in Two-Dimensional Irrotational Flow". Phys. Fluids 10, 21 (1967).

18. Camac, M.
"CO_2 Relaxation Processes in Shock Waves". Avco-Everett Res. Lab. Res. Rep. No. 194 (1964).

19. Courant, R.
Friedrichs, K. O.
Supersonic Flow and Shock Waves, Interscience Pub., New York (1948).

20. Ferri, A.

Tube Experiments, Pergamon, New York (1961).

21. Gaydon, A. G.
Hurle, I. R.
"Measurement of Times of Vibrational Relaxation and Dissociation Behind Shock Waves in N_2, O_2, Air, CO, CO_2 and H_2". 8th Symp. (International) on Comb. 309 (1962).

22. Glass, I. I.
Shock Waves & Man, U. of Toronto Press, Toronto (1974).

23. Griffith, W.
Brickl, D.
Blackman, V.
"Structure of Shock Waves in Polyatomic Gases". Phys. Rev. 102, 1209 (1956).

24. Griffith, W. C.
Kenney, A.
"State of Partial Equilibrium Behind Shock Waves in O_2, N_2, CO, CO_2 and N_2O". Tech. Rep. II-23, Dept. of Physics, Princeton U. (1957).

25. Gvozdeva, L. G.
Predvoditeleva, O. A.
"Experimental Investigation of Mach Reflection of Shock Waves with Velocities of 1000-3000 m/sec in Carbon Dioxide Gas, Nitrogen, and Air". Soviet Phys.-Doklady 10, 694 (1966).

26. Gvozdeva, L. G.   "Mach Reflection of Shock Waves in Real
    Bazhenova, T. V.   Gases". Astronautica Acta 14, 503 (1969).
    Predvoditeleva, O. A.
    Fokeev, V. P.

27. Gvozdeva, L. G.   "Transition from Mach to Regular Reflection
    Fokeev, V. P.   and Domains of Various Mach Reflection
                      Configurations". Comb., Deton., and Shock
                      Waves 13, 86 (1977).

28. Hall, J. G.   "The Design and Performance of a 9-inch
                      Plate Mach-Zehnder Interferometer".
                      UTIAS Rep. No. 27 (1954).

29. Henderson, L. F.   "Experiments on Transition of Mach Reflection".
    Lozzi, A.   J. Fluid Mech. 68, 139 (1975).

30. Henderson, L. F.   "Further Experiments on Transition to
    Lozzi, A.   Mach Reflection". J. Fluid Mech. 94, 541
                      (1979).

31. Hornung, H. G.   "Transition from Regular to Mach Reflexion
    Kychakoff, G.   of Shock Waves in Relaxing Gases". Proc.
                      11th International Shock Tube Symp. (1977).

32. Hornung, H. G.   "Transition to Mach Reflexion of Shock Waves
    Oertel, H.   in Steady and Pseudosteady Flow with and
    Sandeman, R. J.   without Relaxation". J. Fluid Mech. 90, 541
                      (1979).

33. Howe, J. T.   "The Dissociative Relaxation of CO_2 Behind
    Viegas, J. R.   Normal Shock Waves". NASA TN D-2131 (1963).

34. Hurle, I. R.   "Vibrational Relaxation and Dissociation of
    Gaydon, A. G   Carbon Dioxide Behind Shock Waves". Nature
                      184, 1858 (1959).

35. Jahn, R. G.   "Transition Processes in Shock Wave Inter-
                      actions". J. Fluid Mech. 2, 33 (1957).

36. Johannesen, N. H.   "Experimental and Theoretical Analysis of
    Zienkiewicz, H. K. Vibrational Relaxation Regions in Carbon
    Blythe, P. A.   Dioxide". J. Fluid Mech. 3, 213 (1962).
    Gerrard, J. H.

37. Jones, D. M.   "A Note on the Pseudo-Stationary Flow Behind
    Martin, P. M. E.   a Strong Shock Diffracted or Reflected at a
    Thornhill, C. K.   Corner". Proc. R. Soc. Lond. A. 209, 238
                      (1951).

38. Kantrowitz, A.   "Heat Capacity Lag in Gas Dynamics".
                      J. Chem. Phys. 14, 150 (1946).

39. Kawamura, R.   "On the Mach Reflection of a Shock Wave". J. Phys. Soc. Japan 6, 533 (1951).

40. Kawamura, R.
    Saito, H.   "Reflection of Shock Waves - I Pseudo-Stationary Case". J. Phys. Soc. Japan 11, 584 (1956).

41. Kutler, P.
    Shankar, V.S.   "Diffraction of a Shock Wave by a Compression Corner: I. Regular Reflection". AIAA J. 15, 197 (1977).

42. Law, C. K.   "Diffraction of Strong Shock Waves by a Sharp Compressive Corner". UTIAS Tech. Note No. 150 (1970).

43. Law, C. K.
    Glass, I. I.   "Diffraction of Strong Shock Waves by a Sharp Compressive Corner". CASI Trans. 4, 2 (1971).

44. Liepmann, H. W.
    Roshko, A.   Elements of Gasdynamics, John Wiley, New York (1957).

45. Merritt, D. L.   "Mach Reflection on a Cone". AIAA J. 6, 1208 (1968).

46. Miller III, C. G.
    Wilder, S. E.   "Tables and Charts of Equilibrium Thermodynamic Properties of Carbon Dioxide for Temperatures from 100K to 25000K". NASA SP-3097 (1976).

47. Miller III, C. G.
    Wilder, S. E.   "Tables and Charts of Equilibrium Normal Shock and Shock-Tube Properties for Pure Carbon Dioxide with Velocities from 1 to 16 km/sec". NASA SP-3100 (1976).

48. Molder, S.   "Particular Conditions for the Termination of Regular Reflection of Shock Waves". Can Aero. & Space J. 25, 44 (1979).

49. Pack, D. C.   "The Reflexion and Diffraction of Shock Waves". J. Fluid Mech. 18, 549 (1964).

50. Polachek, H.
    Seeger, R. J.   "On Shock-Wave Phenomena: Interaction of Shock Waves in Gases". Proc. 1st Symp. Appl. Math. 119 (1949).

51. Schneyer, G. P.   "Numerical Simulation of Regular and Mach Reflections". Phys. Fluids 18, 1119 (1975).

52. Schwartz, R. N.   "Equations Governing Vibrational Relaxation Phenomena in Carbon Dioxide Gas". NAVORD Rep. No. 3701 (1954).

53. Semenov, A. N.
    Syschikova, M. P.
    Berezkina, M. K.
"Experimental Investigation of Pecularities of Mach Reflection". Soviet Phys.-Tech. Phys. 15, 795 (1970).

54. Shankar, V. S.
    Kutler, P.
    Anderson, D. A.
"Diffraction of Shock Waves by a Compression Corner, Part II -- Single Mach Reflection". AIAA Paper 77 (1977).

55. Smiley, E. F.
    Winkler, E. H.
    Slawsky, T. K.
"Measurement of Vibrational Relaxation Effect in CO_2 by means of Interferograms". J. Chem. Phys. 20, 923 (1952).

56. Smith, L. G.
"Photographic Investigation of the Reflection of Plane Shocks in Air". OSRD Rep. No. 6271 (1945).

57. Smith, W. R.
"Mutual Reflection of Two Shock Waves of Arbitrary Strengths". Phys. Fluids 2, 533 (1959).

58. Smith, W. R.
"Four-Shock Configuration". Phys. Fluids 5, 593 (1962).

59. Sternberg, J.
"Triple-Shock-Wave Intersections". Phys. Fluids 2, 179 (1959).

60. Syshchikova, M. P.
    Krassovskaya, I. V.
"Some Properties of Regular and Irregular Interaction of Shock Waves". Arch. Mech. 31, 135 (1979).

61. von Neumann, J.
"Oblique Reflection of Shocks". Explosives Research Rep. No. 12, Navy Dept., Bureau of Ordnance (1943).

62. Weihs, D.
    Manheimer-Timnat, Y.
"Carbon dioxide Dissociation Relaxation Times, Measured in a Shock Tube". AIAA J. 7, 764 (1969).

63. Weynants, R. R.
"An Experimental Investigation of a Shock Wave Diffraction Over Compression and Expansion Corners". UTIAS Tech. Note No. 126 (1968).

64. White, D. R.
"An Experimental Survey of the Mach Reflection of Shock Waves". 2nd Midwestern Conf. on Fluid Mech. (1952).

65. White, W. B.
    Johnson, S. M.
    Dantzig, G. B.
"Chemical Equilibrium in Complex Mixtures". J. Chem. Phys. 28, 751 (1958).

66. Witteman, W. J.
"Instrument to Measure Density Profiles Behind Shock Waves". Rev. Sci. Instr. 32, 292 (1961).

67. Witteman, W. J.   "Vibrational Relaxation in Carbon Dioxide
                              II." J. Chem. Phys. 37, 655 (1962).

68. Zienkiewicz, H. K.   "Departures from the Linear Equation for
    Johannesen, N. H.   Vibrational Relaxation in Shock Waves in
                              Oxygen and Carbon Dioxide". J. Fluid
                              Mech. 17, 499 (1963).

25
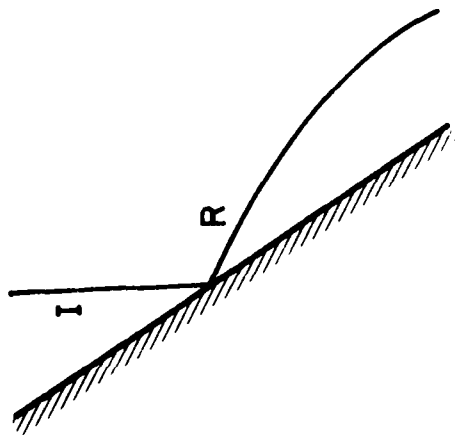
Regular Reflection (RR)
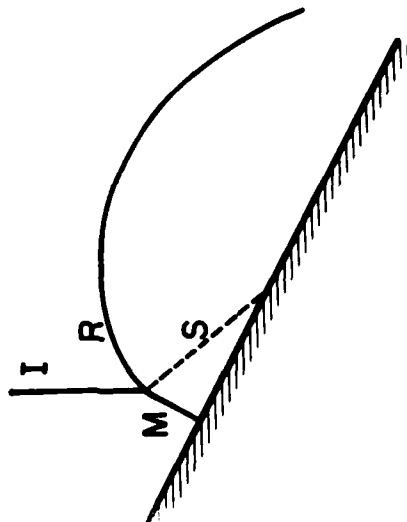
Single Mach Reflection (SMR)
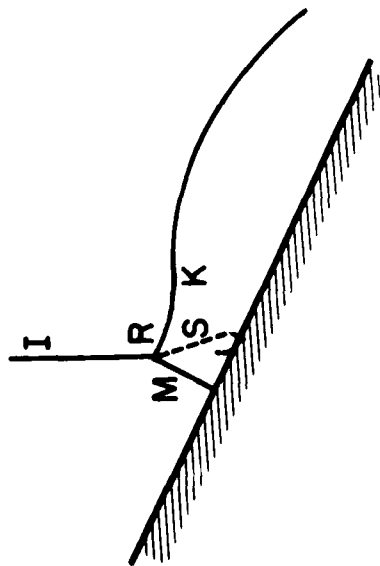
Complex Mach Reflection (CMR)
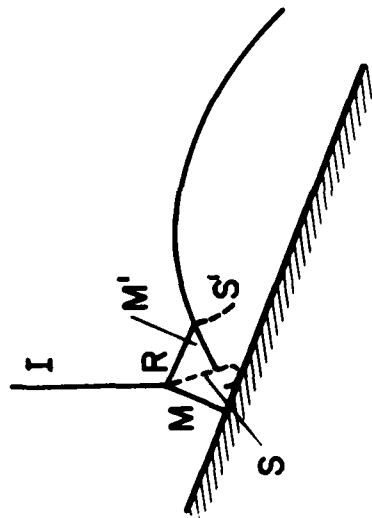
Double Mach Reflection (DMR)

FIG. 1 TYPES OF REFLECTION (SCHEMATIC)

I: INCIDENT SHOCK
R: REFLECTED SHOCK
M: MACH STEM
M':   SECOND MACH SHOCK
S,S':   SLIPSTREAM
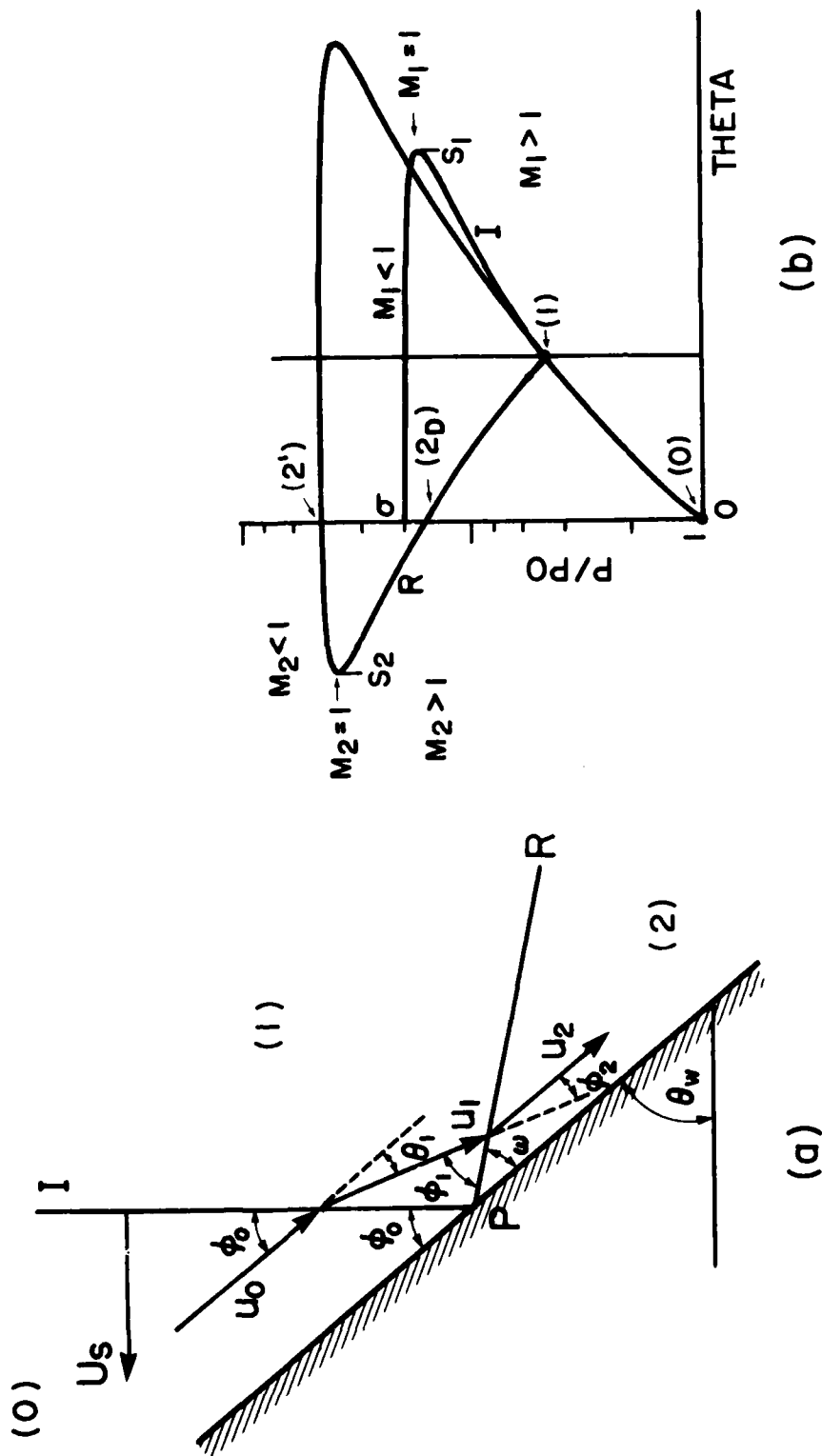
FIG. 2 REGULAR REFLECTION. (a) PHYSICAL PLANE, (b) θ-P PLANE.

I: INCIDENT-SHOCK POLAR
R: REFLECTED-SHOCK POLAR
S_1, S_2: SONIC POINTS

(0), (1) AND (2) INDICATE THE POINTS CORRESPONDING
TO REGIONS 0, 1 AND 2, RESPECTIVELY.

(a)

(b)

(b)

(a)

(b)

(a)
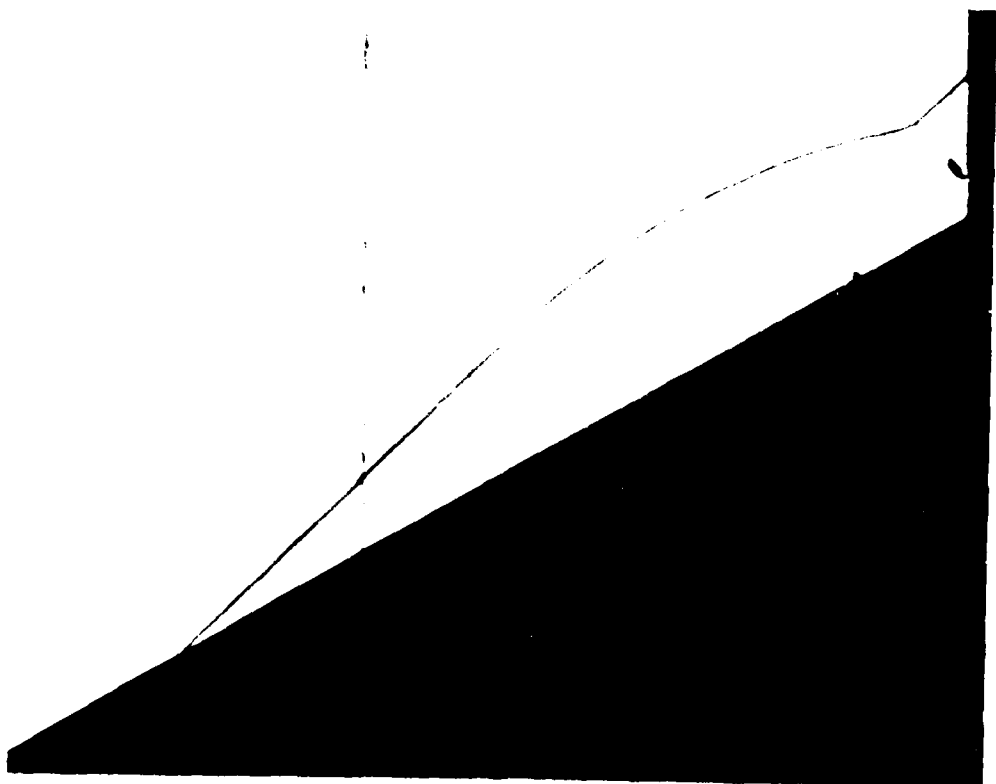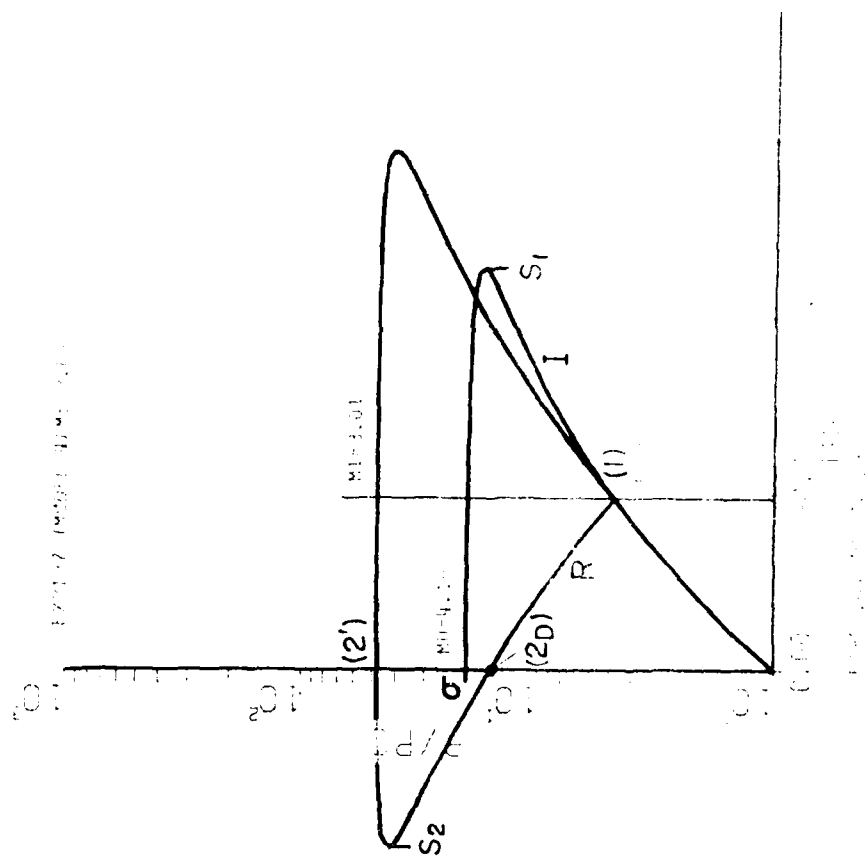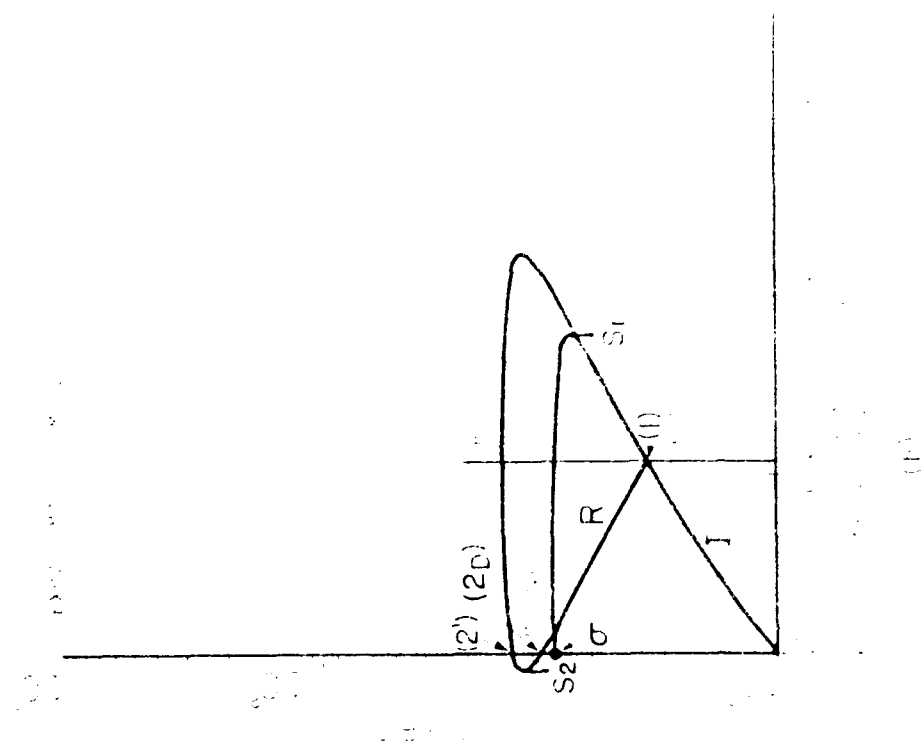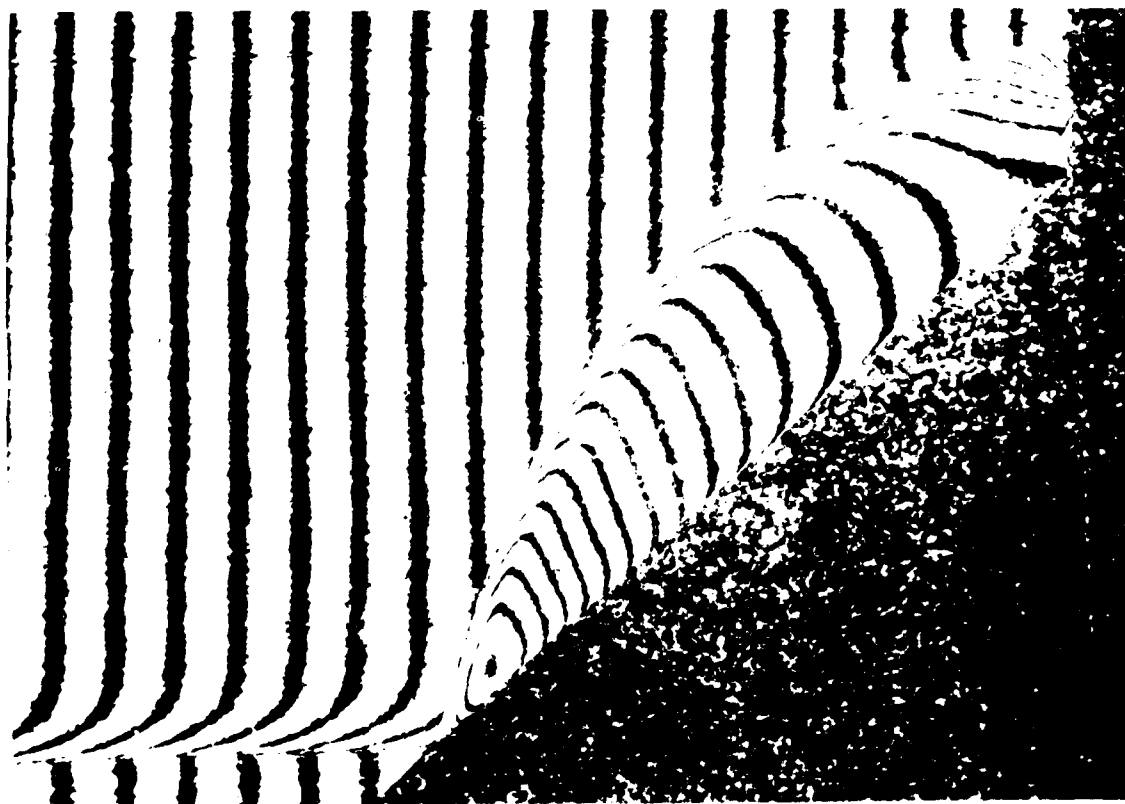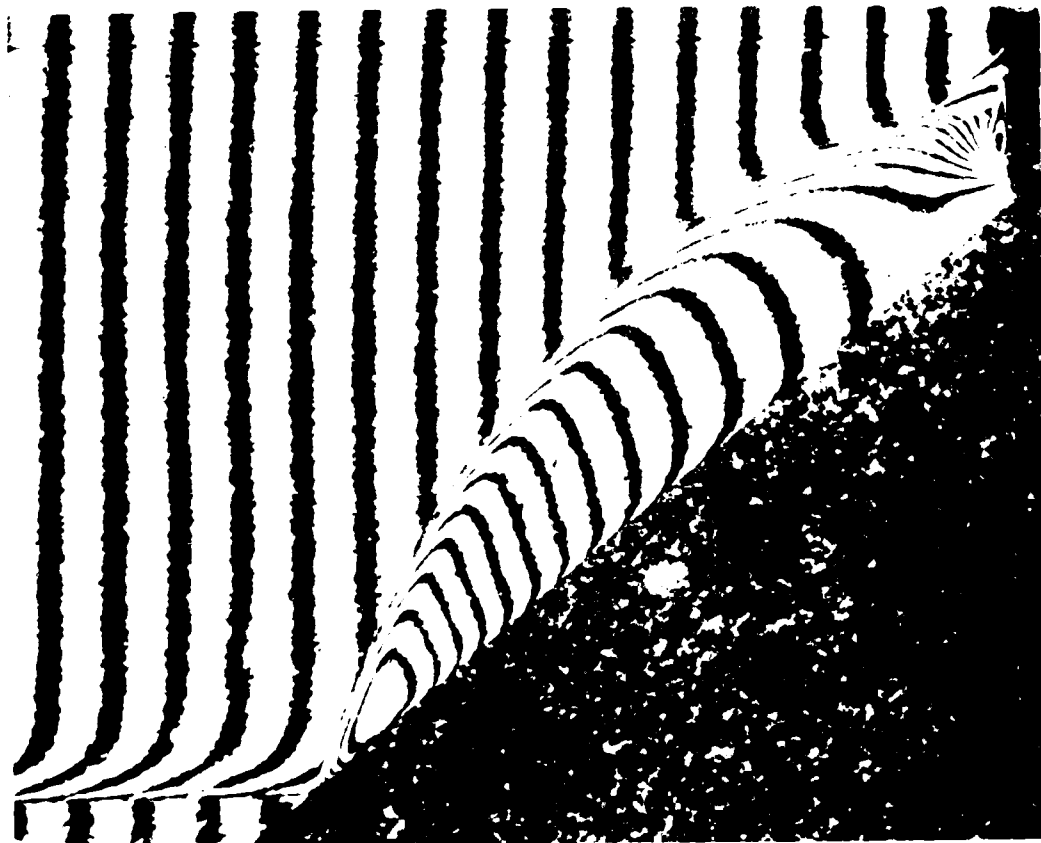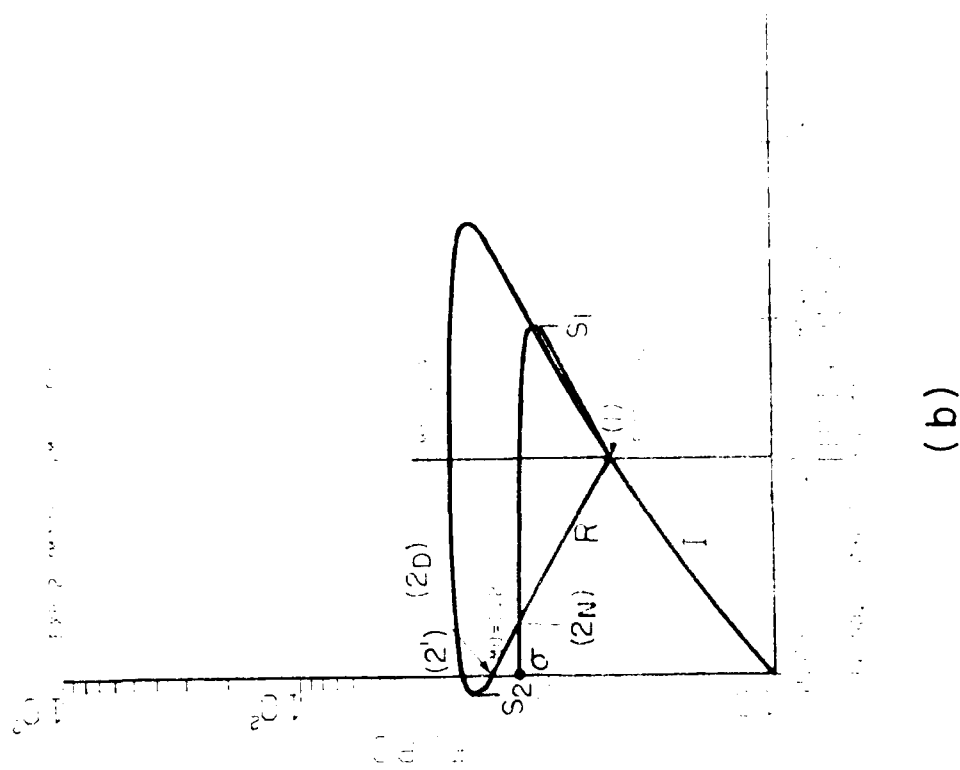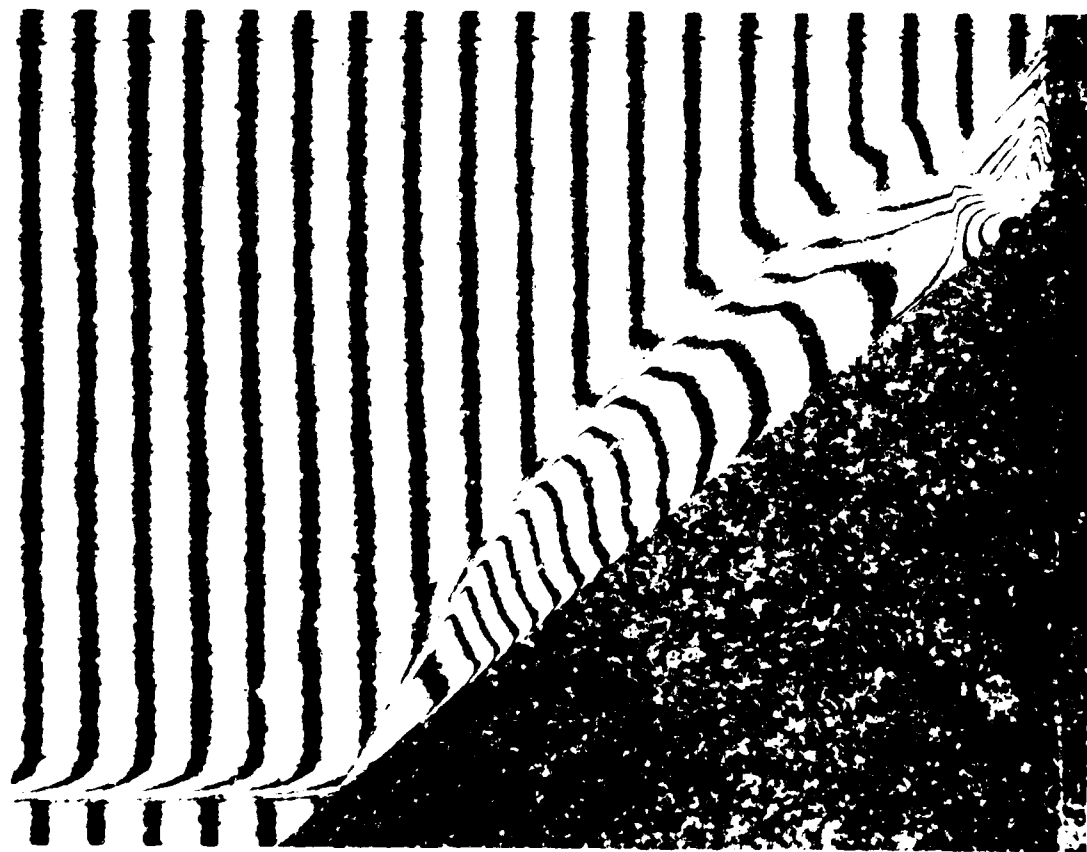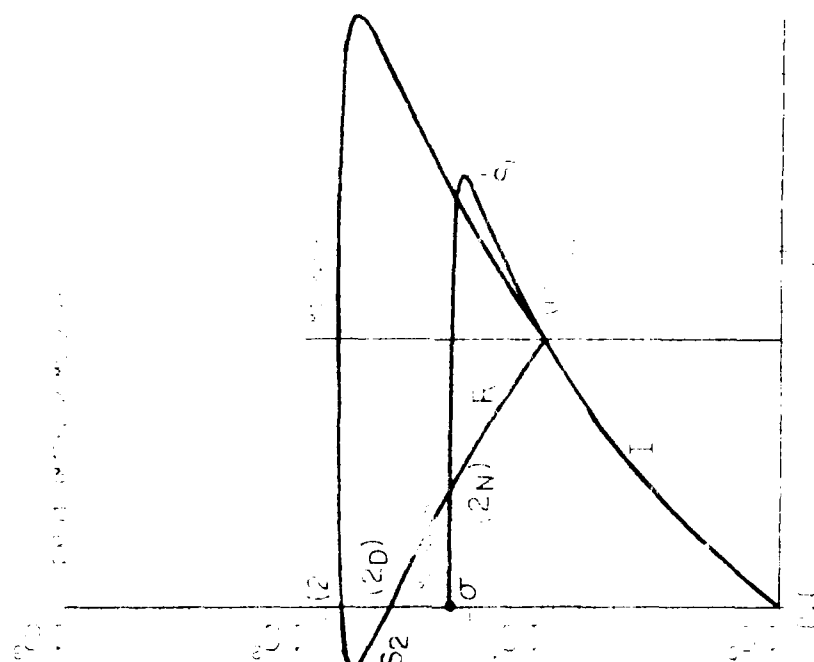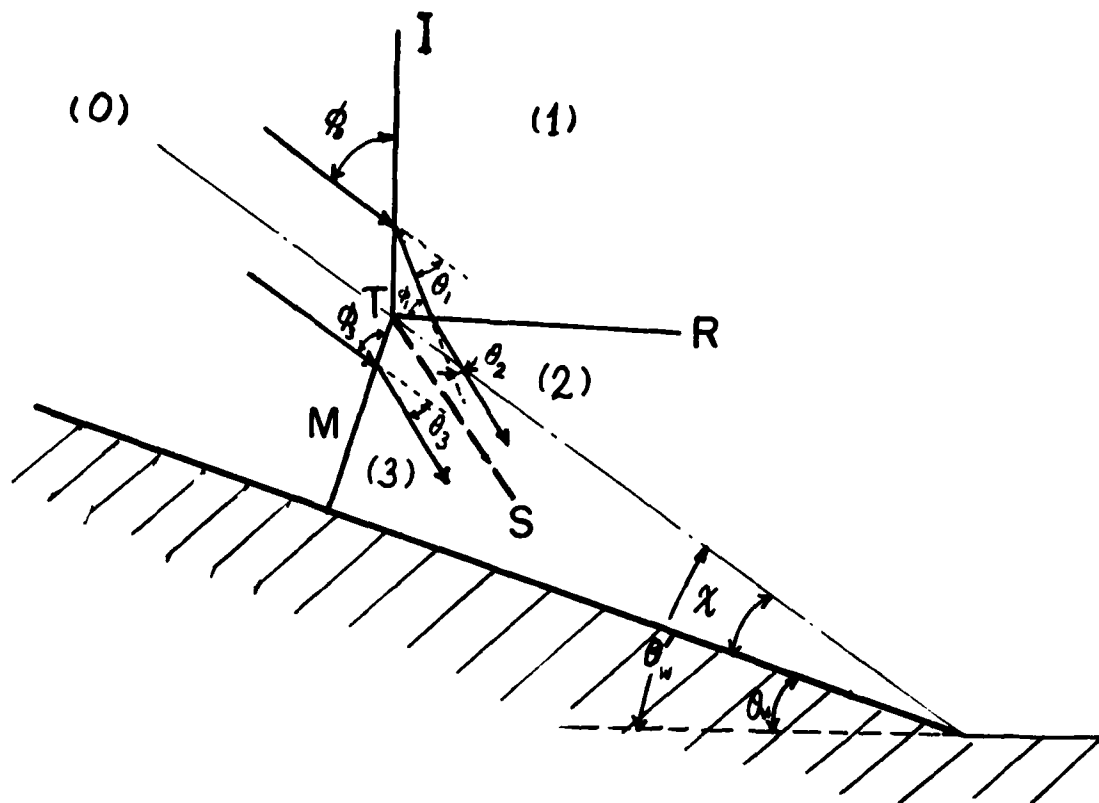
FIG. 7   MACH REFLECTION.   FLOW VELOCITIES IN THE FRAME OF REFERENCE
ATTACHED TO THE TRIPLE POINT T.

I: INCIDENT SHOCK
R: REFLECTED SHOCK
M: MACH STEM
S: SLIPSTREAM
θ_W: WEDGE ANGLE
χ: TRAJECTORY ANGLE OF THE TRIPLE POINT
$\theta_W' = \theta_W + \chi$:   EFFECTIVE WEDGE ANGLE

FIG. 8 SINGLE MACH REFLECTION. (a) PHYSICAL PLANE (SCHEMATIC),
(b) θ-P SHOCK POLAR DIAGRAM.

I: INCIDENT SHOCK POLAR
R: REFLECTED-SHOCK POLAR
S_1, S_2: SONIC POINTS OF I- AND R-POLARS, RESPECTIVELY.

NUMBERS IN PARENTHESES INDICATE THE STATES IN THOSE REGIONS.

(a)

(b)
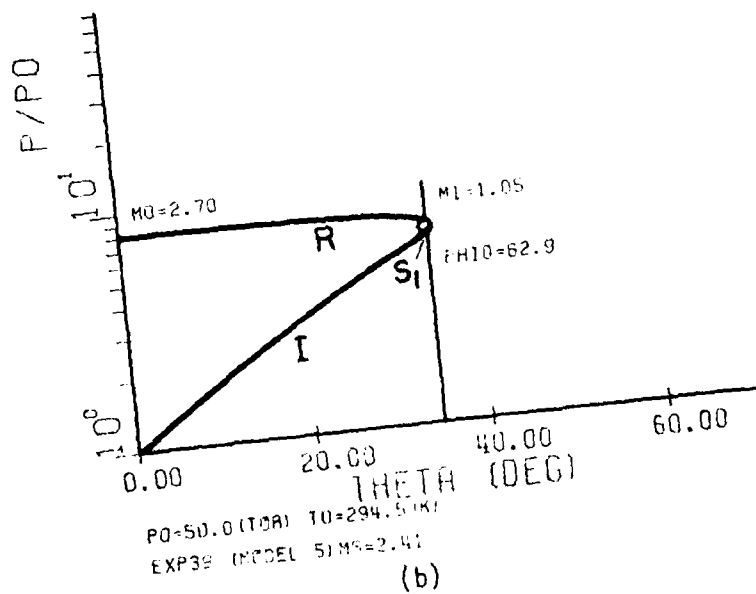
Gas: CO_2, $\theta_w = 10$, $M_s = 2.1$, $P_0 = $ torr, $T_0 = 294.5$ K.

(a) INTERFEROGRAM
(b) P-θ SHOCK POLAR DIAGRAM

(a)

(b)

I . . . . . , . w . 17 , N_s - 1.7° , i . . . torr, . . . - . . . .

. .) I . . . . - I . . I . . . . (. . . . .)
. . . . - . . . .

(a)

(b)

(a)

(b)

FIG. 12 COMPLEX MACH REFLECTION.

(a) PHYSICAL PLANE (SCHEMATIC)
(b) θ-P SHOCK POLAR DIAGRAM

I: INCIDENT-SHOCK POLAR
R: REFLECTED-SHOCK POLAR
S: SONIC POINT (M_1 = 1)
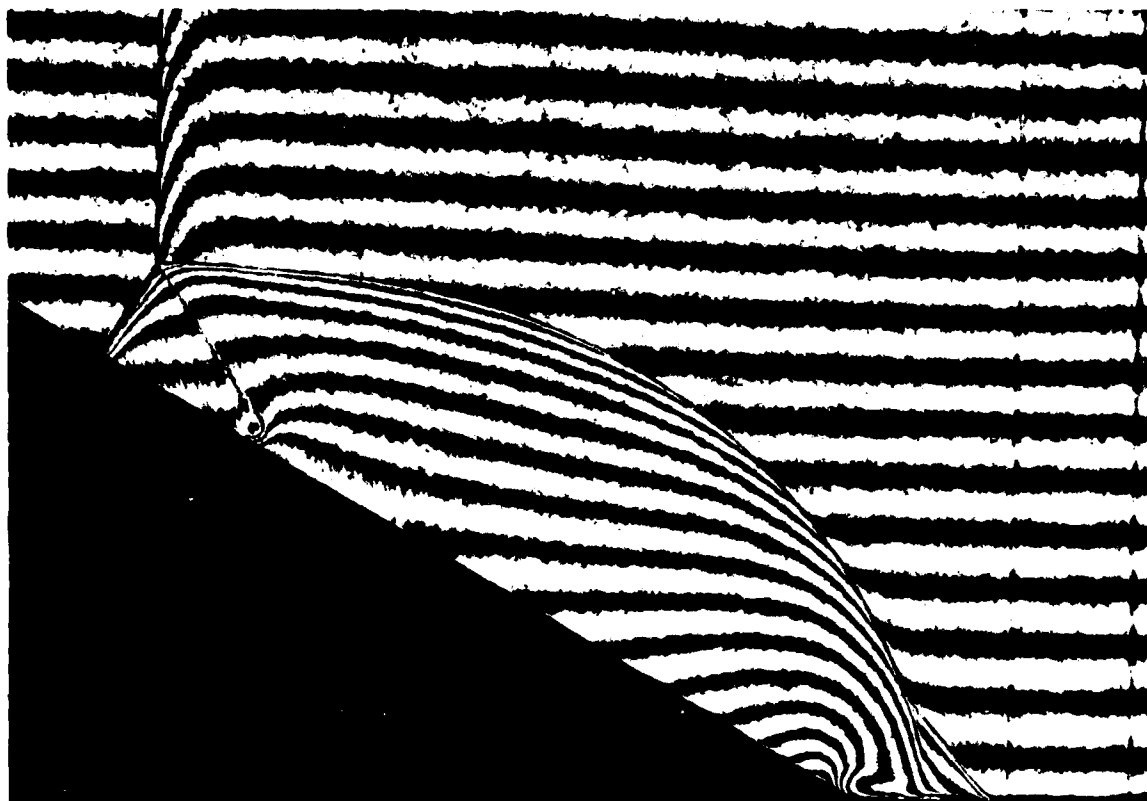
(a)
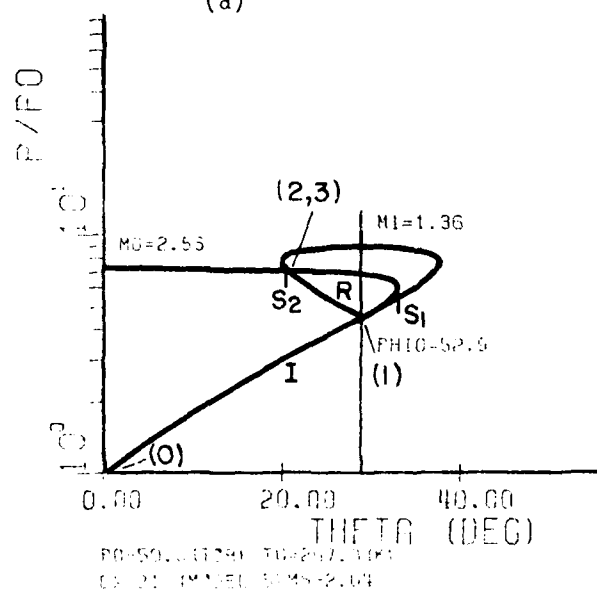
(b)
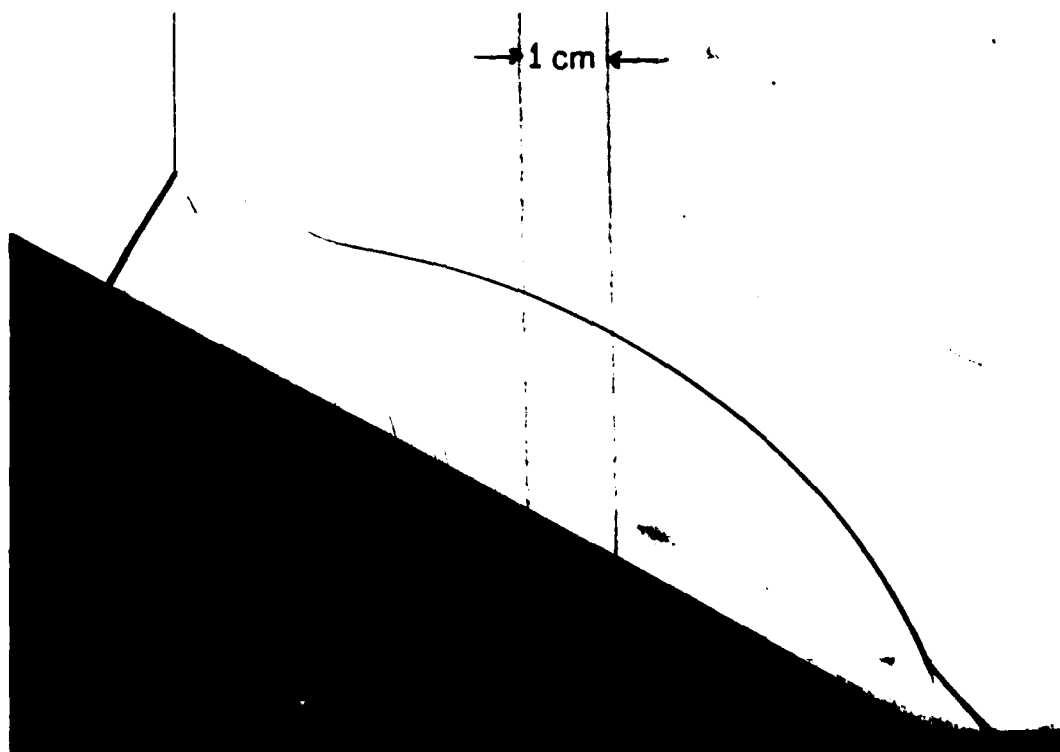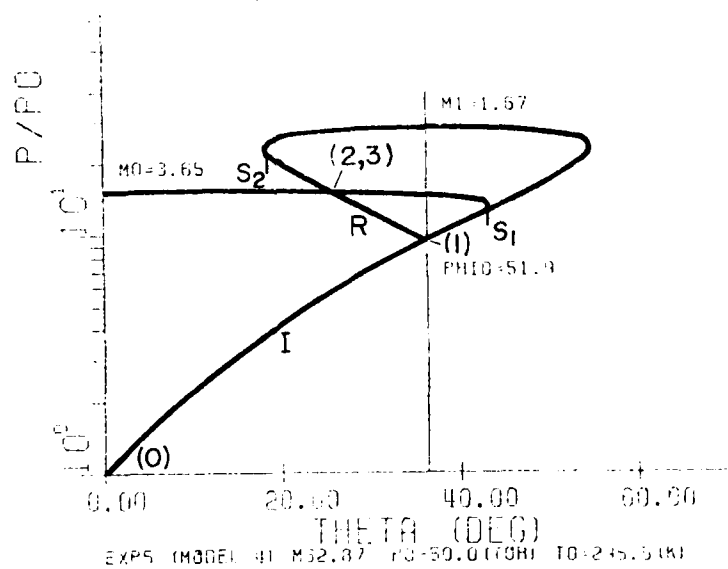
(a)

(b)

FIG. ... , ... = 7, M₀ ... , ... tons, ...

(a) ... -... ... AM (... R)
(b) -... ... ...

ρ / ρ_o

.
.
.
.
a .
.
.
.
6.62
.
.
.
.

Fig. 3 — ... $\alpha = 27.1°$, $p_o = 70$ torr.
... $\rho_o = ...$ x10^-6 g/cm³.

(a) ...

(a)

(b)

$I \ldots \ldots \Rightarrow 0 \Rightarrow$, $\quad \varphi = 20^\circ$, $M_0 = 2.17$, $P_0 = 5$ torr, $T_0 = 295.5°K$.

(a) A SCHAN
(b) A PHOTOGRAPH A DATABASE

FLOW MACH NO.

DISTANCE FROM THE FOOT OF THE MACH STEM (CM)

—— FLOW MACH NO.
--- PROFILE OF THE REFLECTED SHOCK AND SLIPSTREAM.
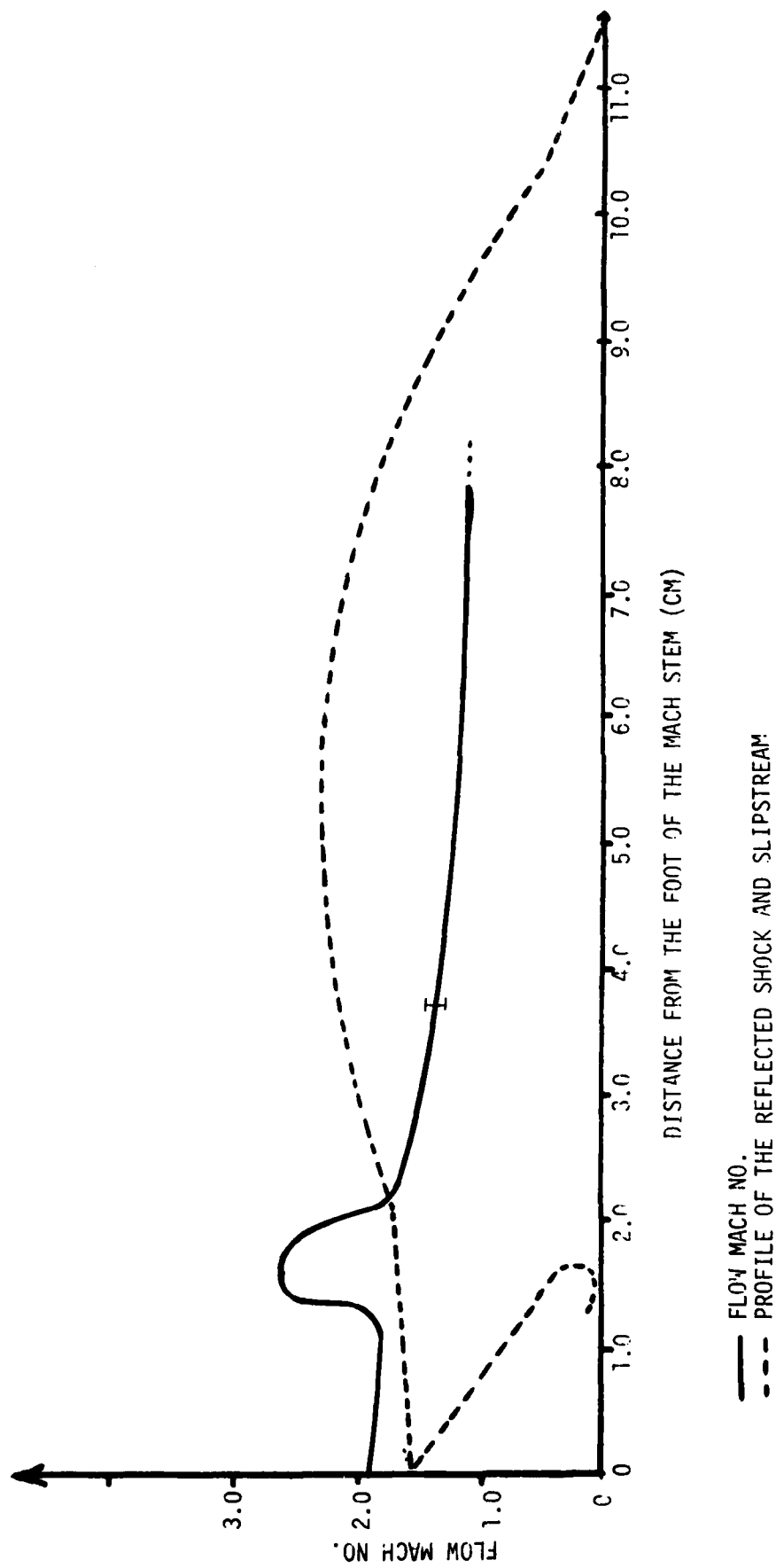
FIG. 15 - CONTINUED

(c) MACH NUMBERS OF THE FLOW ALONG THE REFLECTING SURFACE.
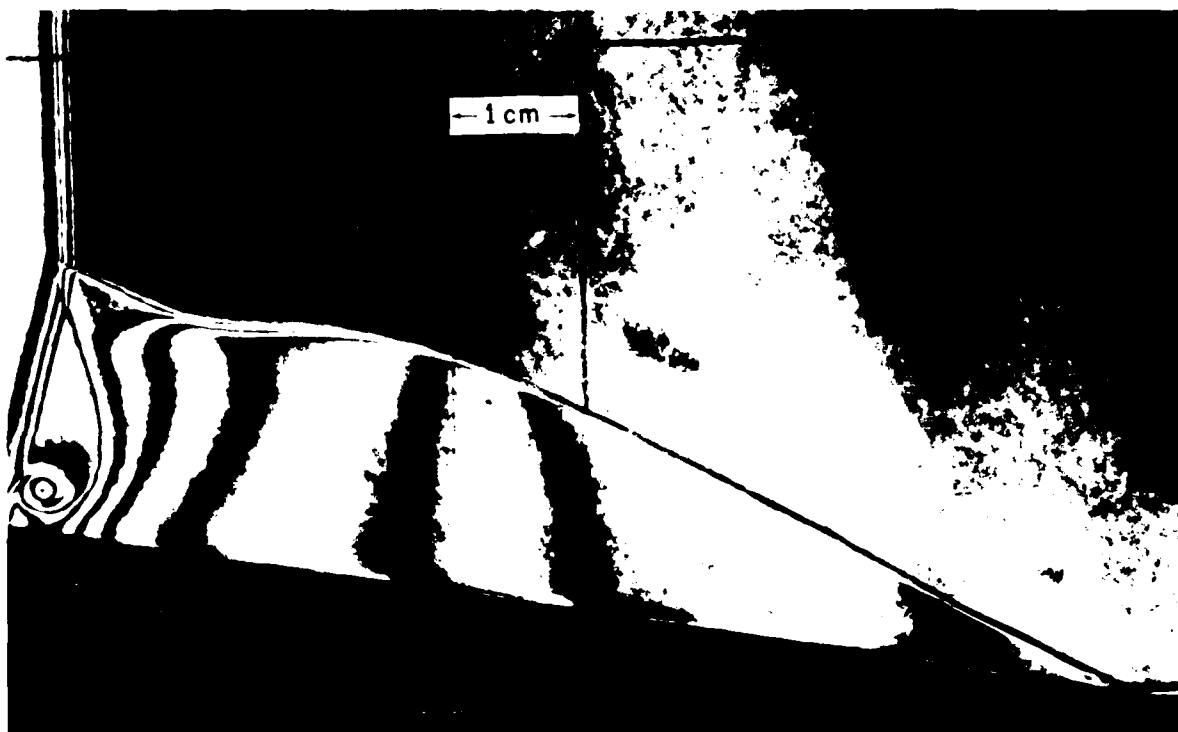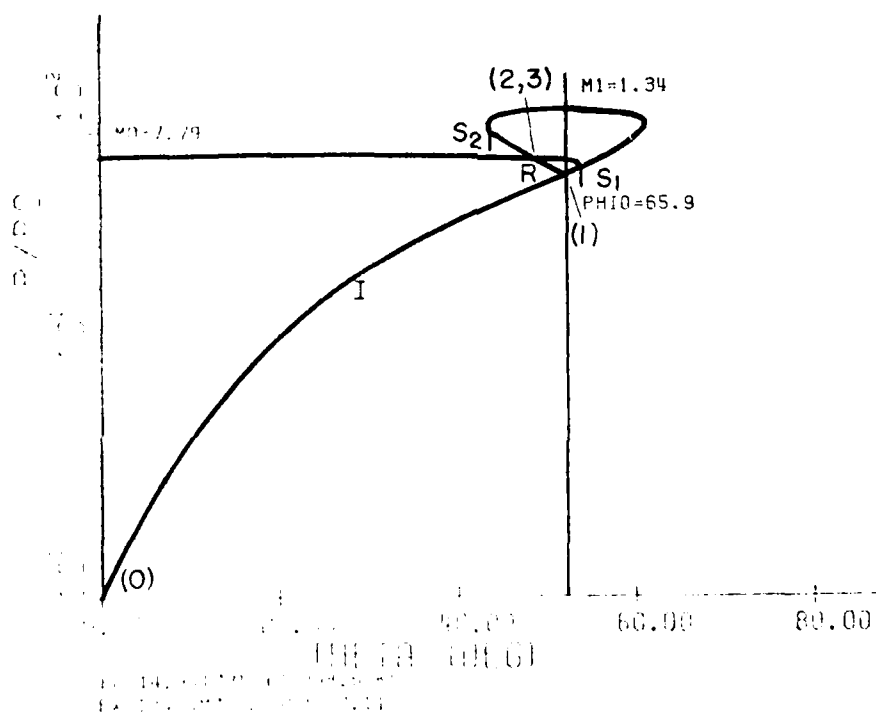
(a)

(b)

(a)
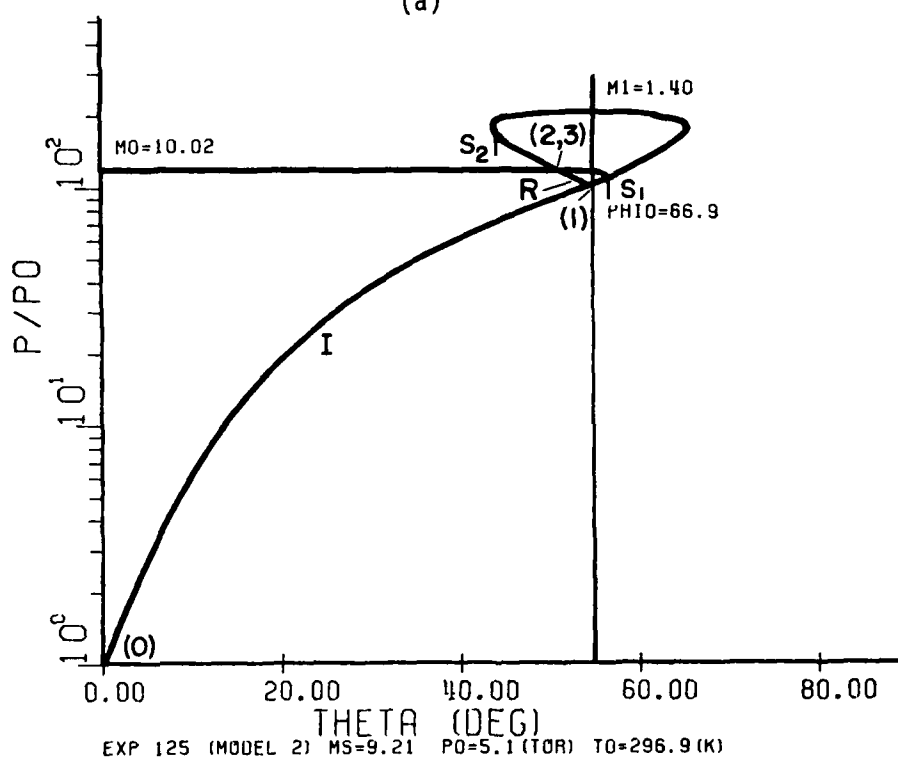
(b)

FIG. 17 CO_2, $\theta_w = 10°$, $M_s = 9.21$, $P_0 = 5.1$ torr, $T_0 = 296.9°K$.

(a) INFINITE-FRINGE INTERFEROGRAM ($\lambda = 6943\text{Å}$)
(b) θ-P SHOCK POLAR DIAGRAM

(a)

Bow Wave

M_S U_o I θ_1

(0)

U_o T θ_2 ω T'

(3) θ_3 (1) U_2 M'

M U_3 (5) (4)

S S'

E ψ

χ^*

θ'_w θ_w O

$P/P0$

$M_2 < 1$

$M_2 = 1$ S_2

$M_2 > 1$ R (2,3)

$M_1 < 1$

(1) S_1 $M_1 = 1$

I

$M_1 > 1$

(0)

0.

THETA
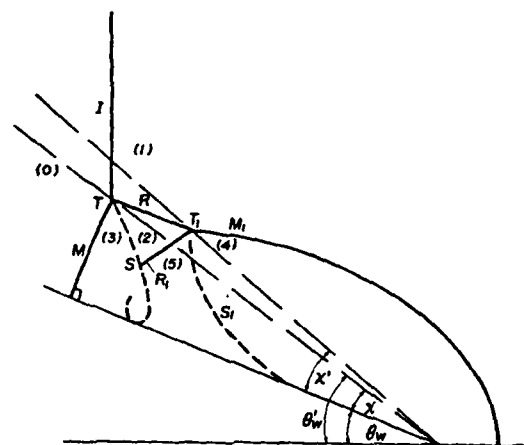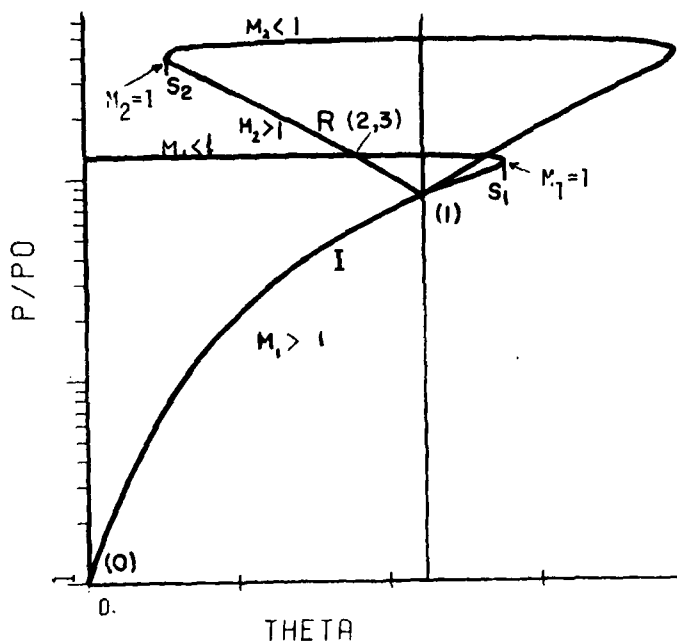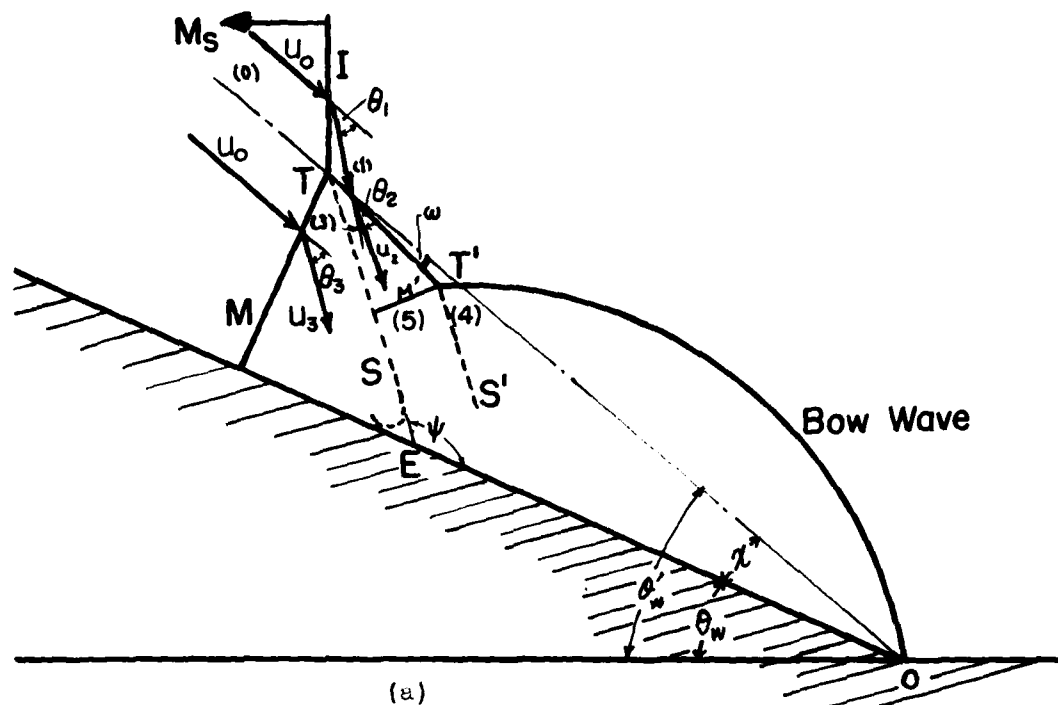
FIG. 18 DOUBLE MACH REFLECTION.

(a) PHYSICAL PLANE (SCHEMATIC)
(b) θ-P SHOCK POLAR DIAGRAM

I: INCIDENT-SHOCK POLAR
R: REFLECTED-SHOCK POLAR
S_1, S_2: SONIC POINTS OF THE I- AND R-POLARS, RESPECTIVELY

NUMBERS IN PARENTHESES INDICATE THE STATES IN THOSE REGIONS.

(c) THE SYSTEM OF REFERENCE FOR DMR ADOPTED BY BEN-DOR & GLASS (7a, b).
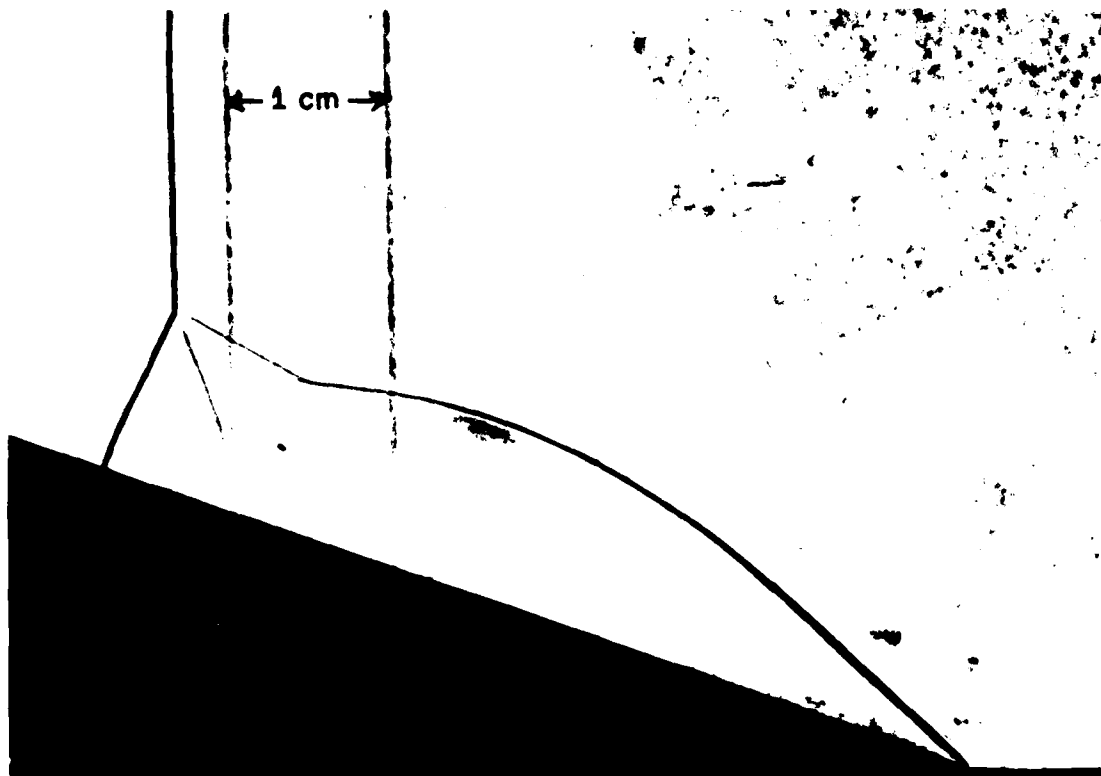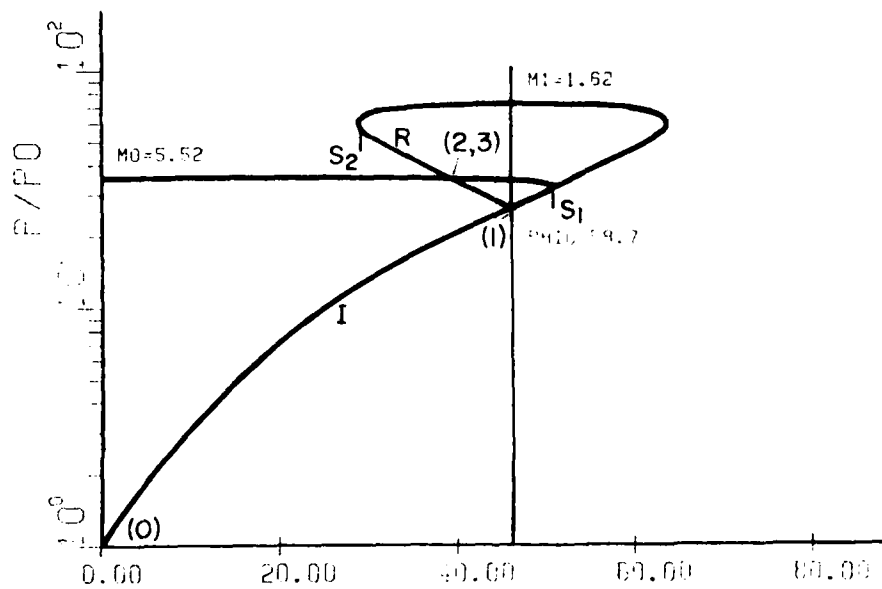
I

(1)

(0)

T R T_1 M_1

(3) (2) (4)

M

S (5) R_1

( ) S_1

χ' χ

θ'_w θ_w

FIG. 18 - CONTINUED

(a)

(b)

Ill. 19 CO_2, $w = 20°$, $M_s = 4.72$, $P_0 = 14.5$ torr, $T_0 = 207.7°K$.

    (a) SHADOWGRAPH
    (b) θ-P SHOCK POLAR DIAGRAM

(a)

(b)
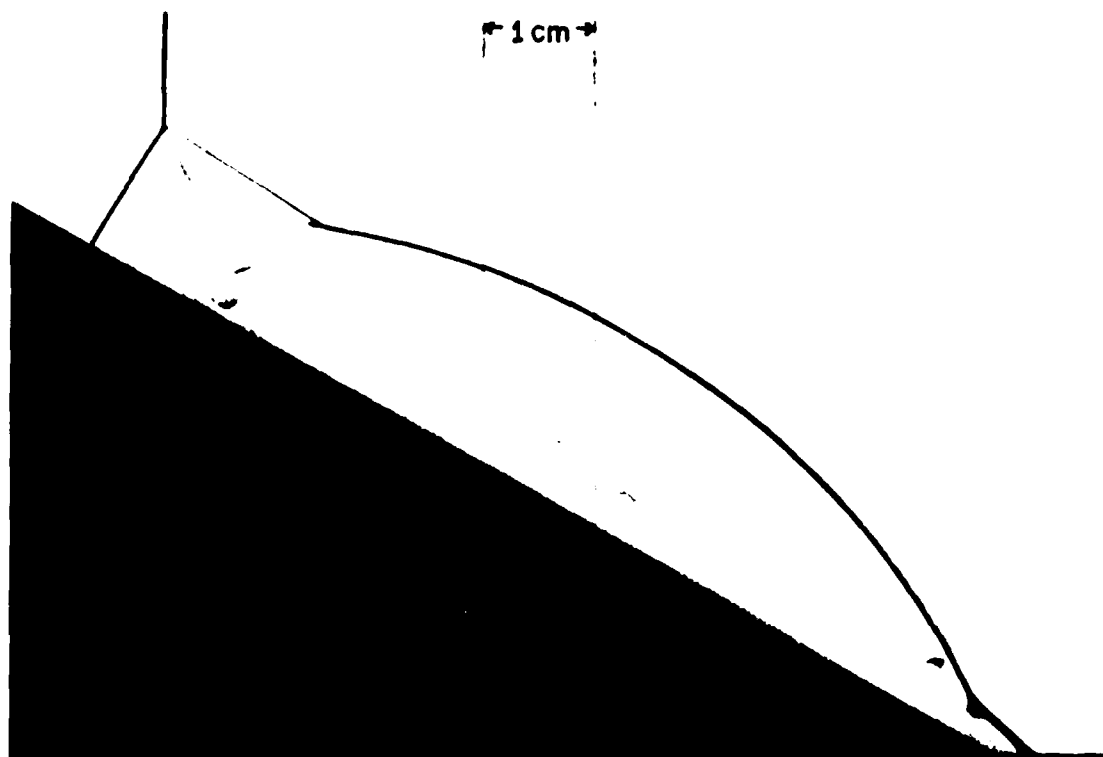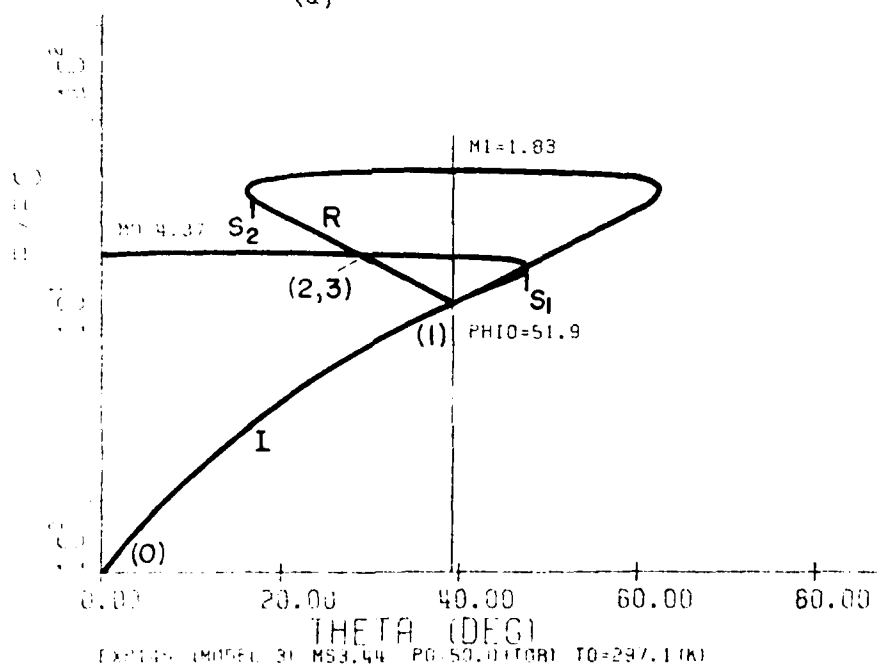
TL. 10 CO$_2$, w = 30°, M$_3$ = 3.—, P$_0$ = 50 torr, T$_0$ = 297.1°K.

(a) SLAT PHOTO.
(b) I-R SHOCK POLAR DIAGRAM

(a)

(b)
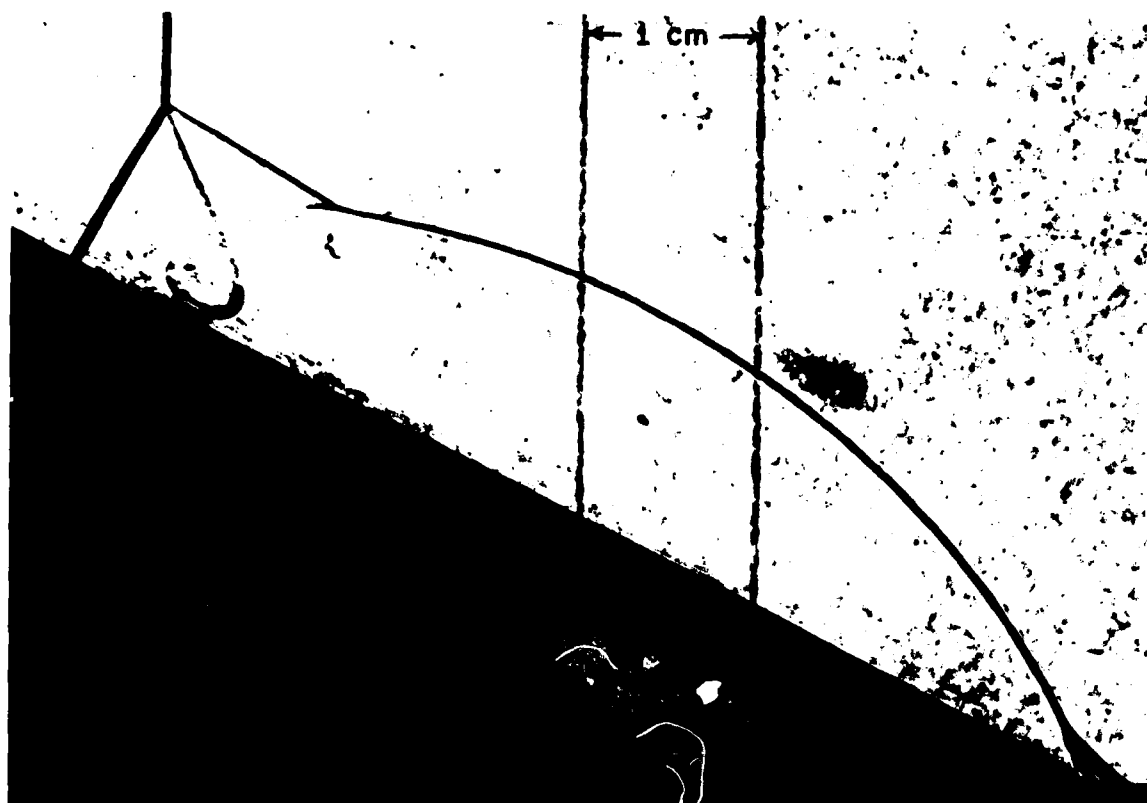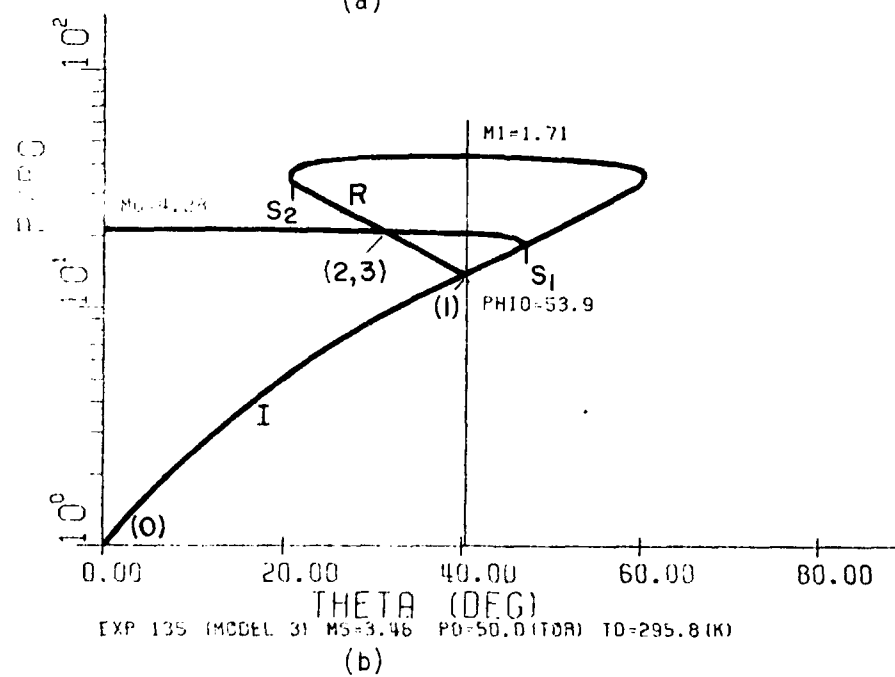
FIG. 21 CO_2, $w = 27°$, $M_s = 3.46$, $P_0 = 50$ torr, $T_0 = 295.8°K$.

(a) SHADOWGRAPH
(b) θ-P SHOCK POLAR DIAGRAM

(a)

(b)

(a)

(b)
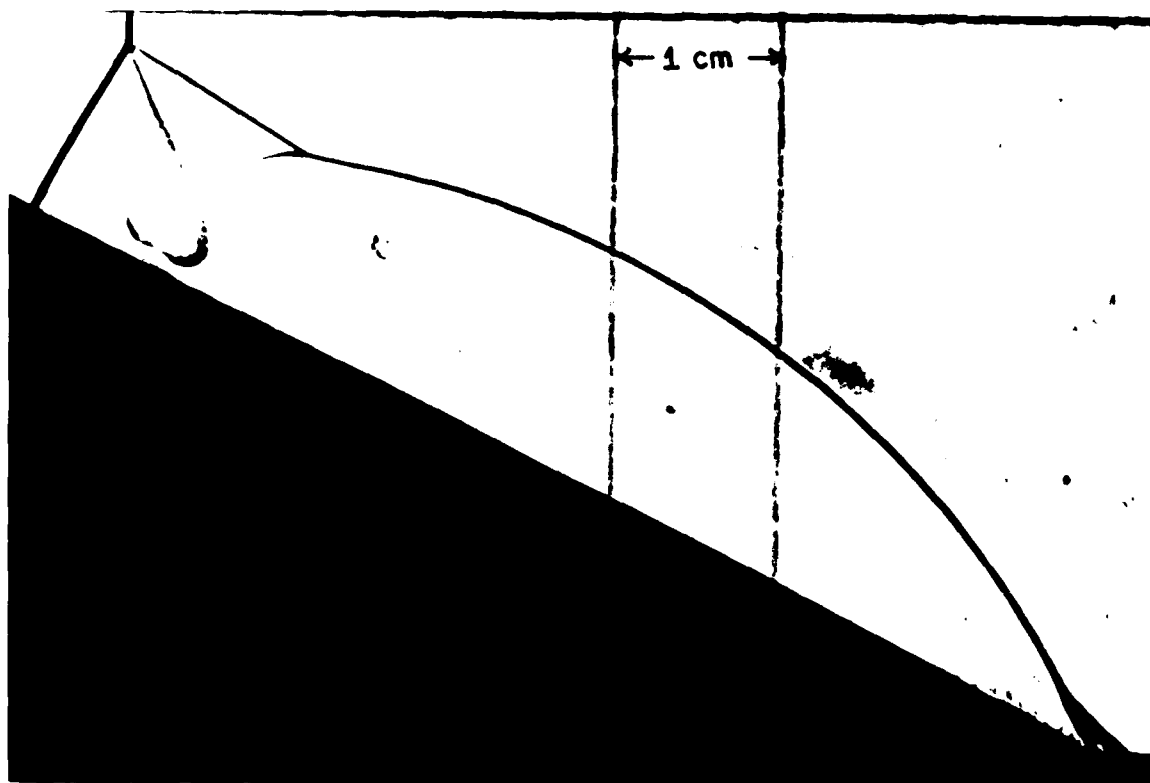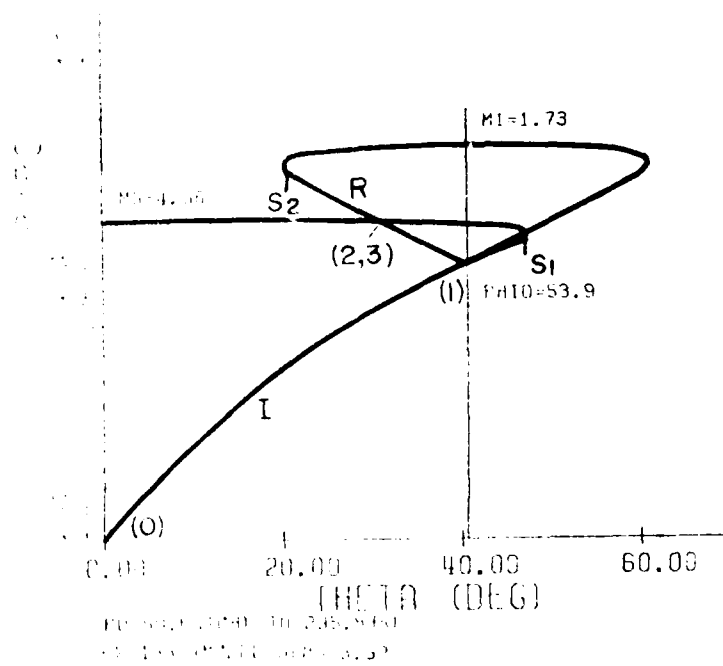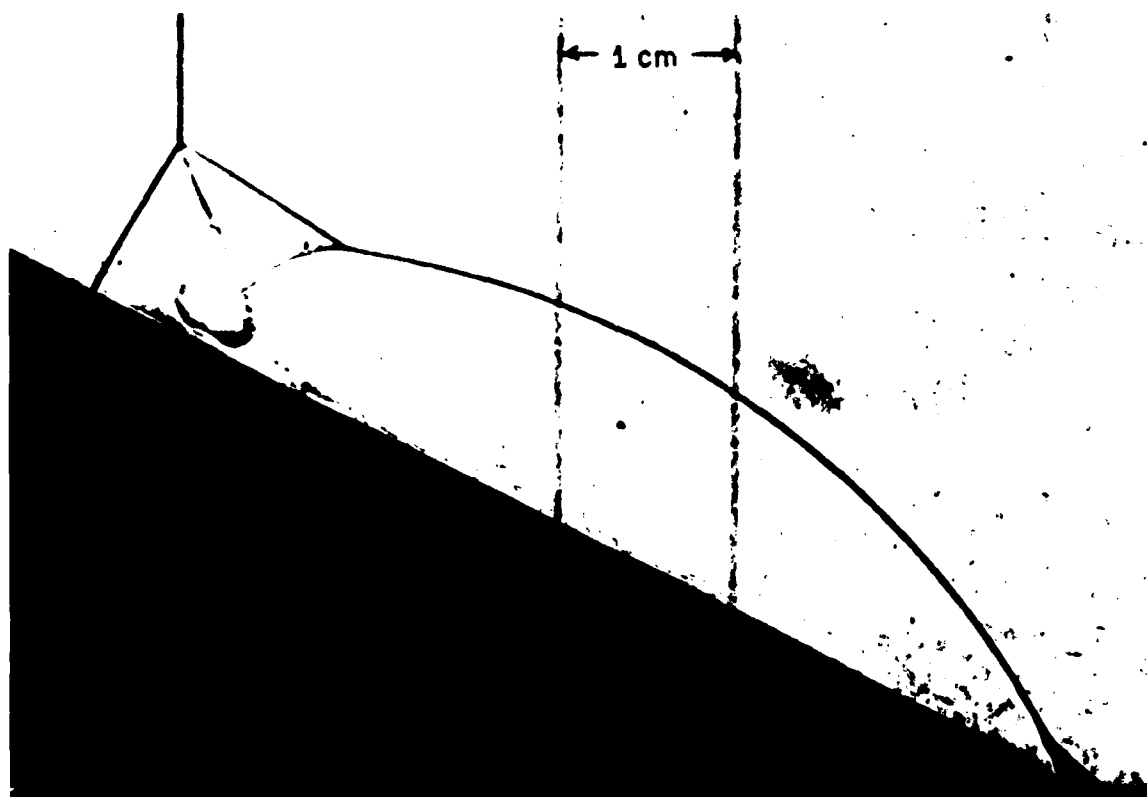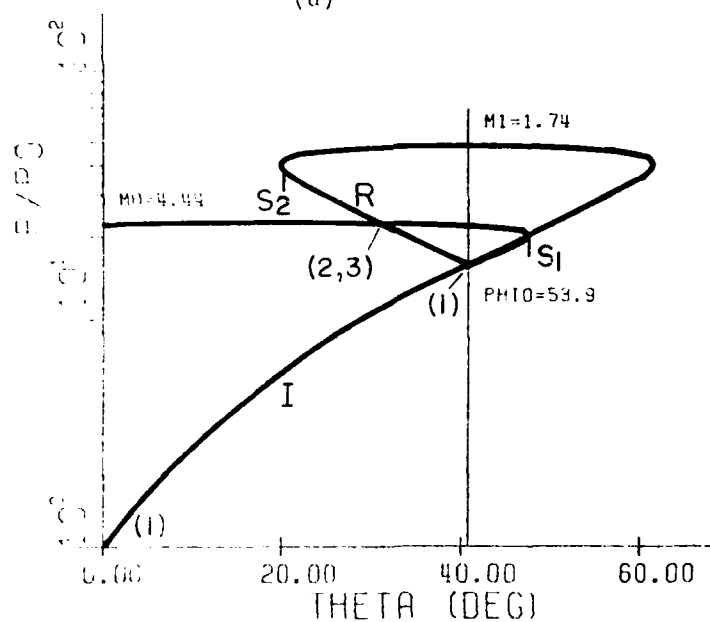
$\theta_{\text{w}} = 27°$, $M_0 = 3.54$, $P_0 = 50$ torr, $T_0 = 295.1°K$.
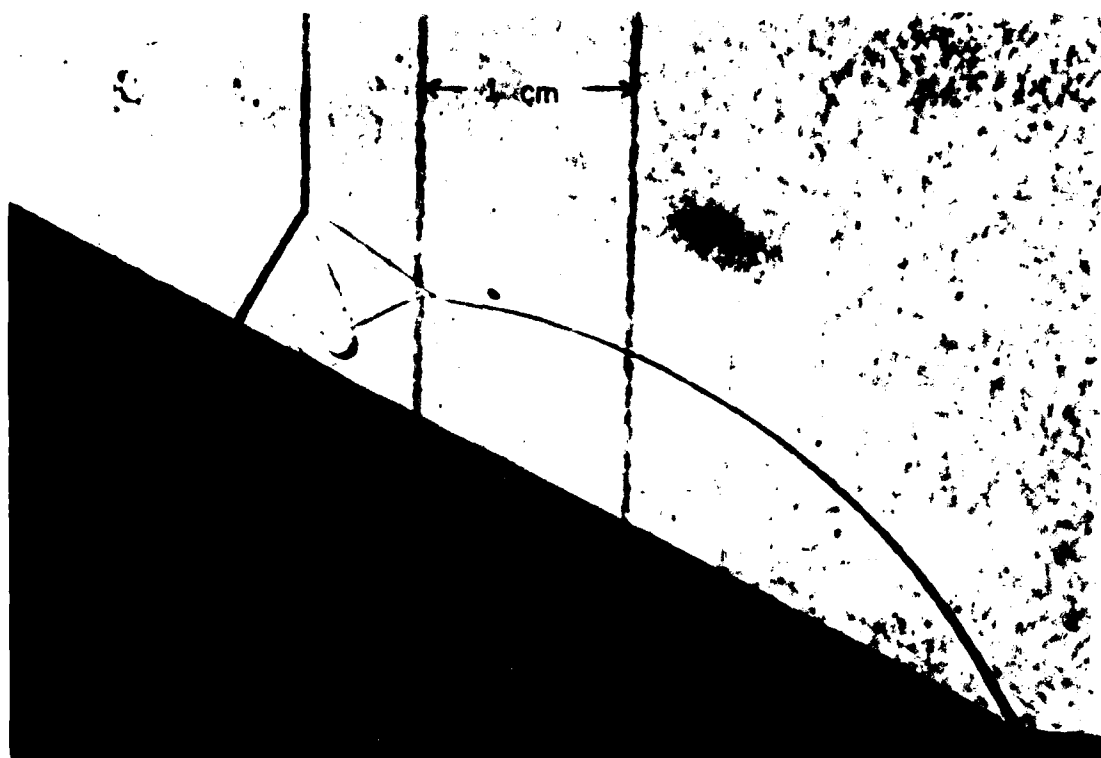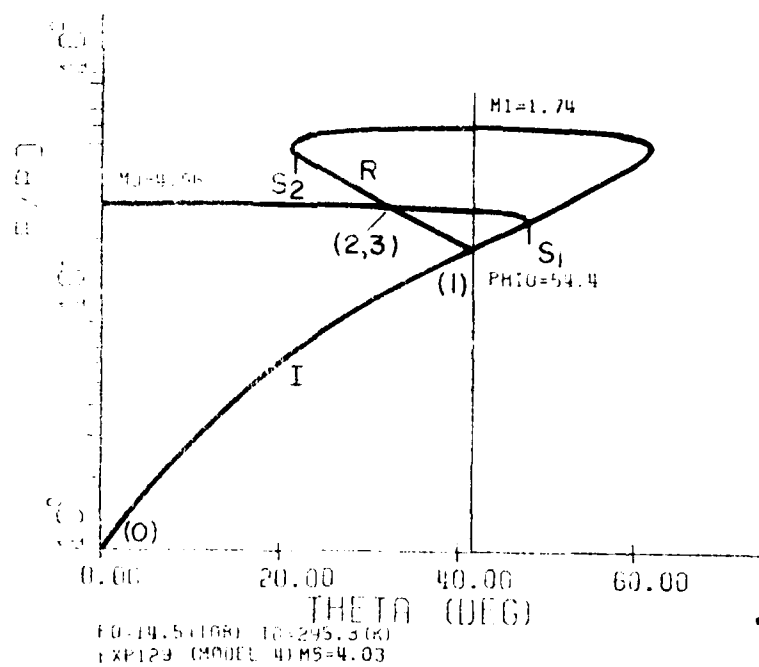
CONICAL FLAP
SHOCK POLAR DIAGRAM

(a)

(b)

(I). (･ ･), ｗ = 27°, ... = 4.03, ... = ...5 torr, T₀ = 295.3°K.

(.) ...Aꞏꞏꞏ AP.

(.) -.. ..OCK POLꞏ. ꞏIAꞏꞏAꞏ

(a)

(b)
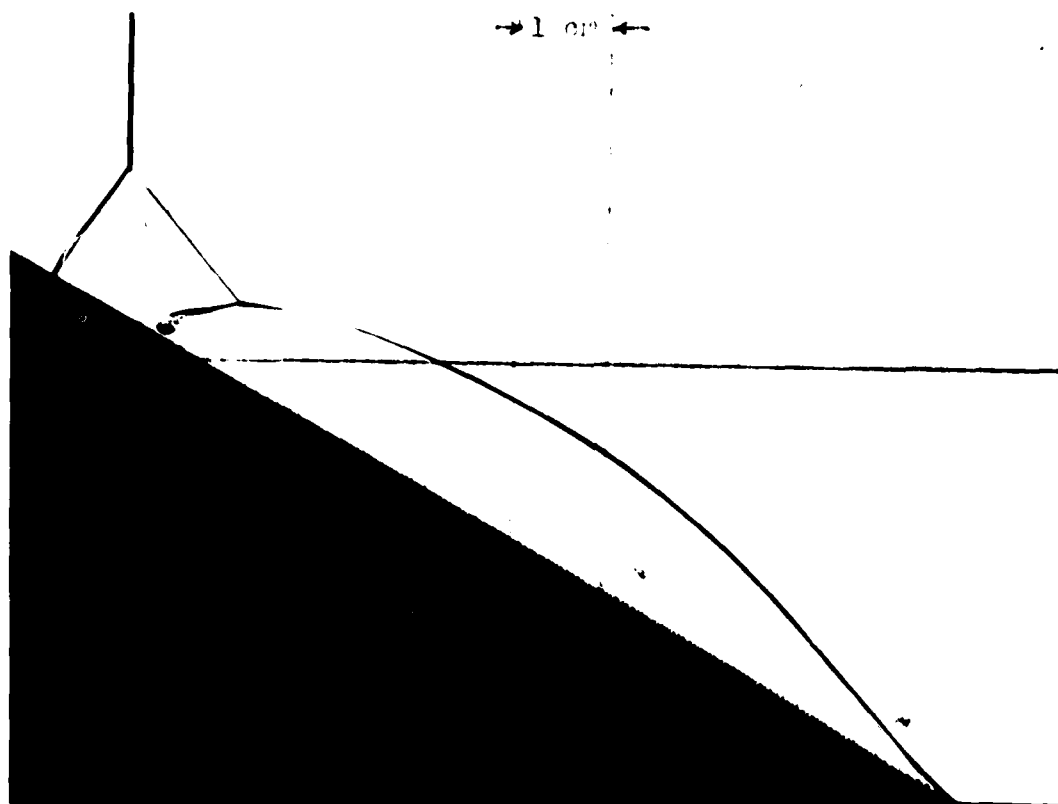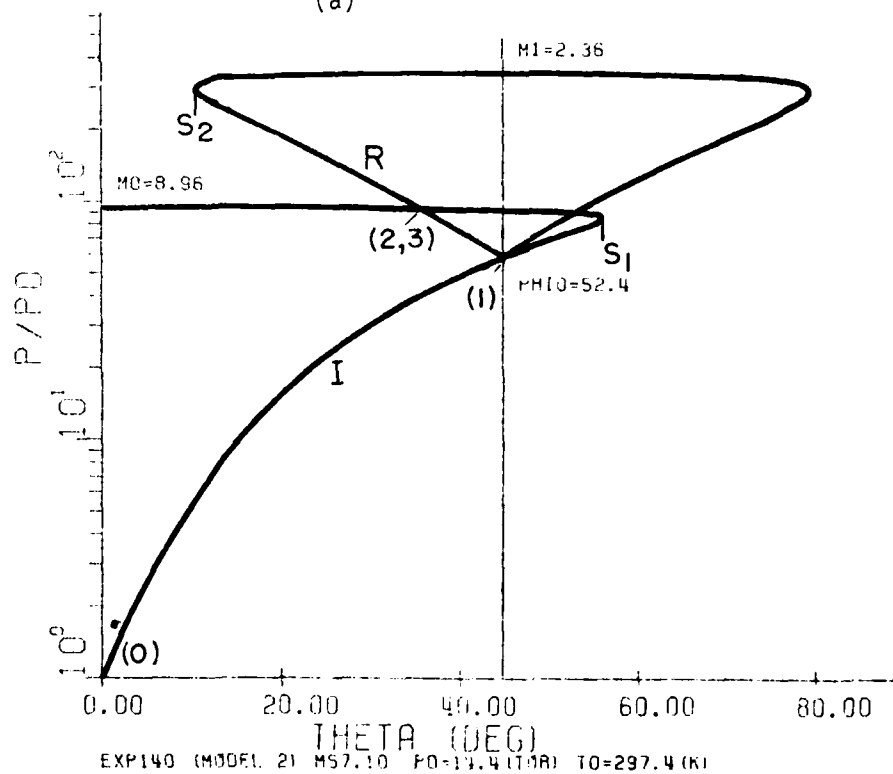
FIG. 25 CO_2, $\theta_w = 30°$, $M_S = 7.10$, $P_0 = 14.4$ torr, $T_0 = 297.4°K$.

(a) SHADOWGRAPH
(b) θ-P SHOCK POLAR DIAGRAM
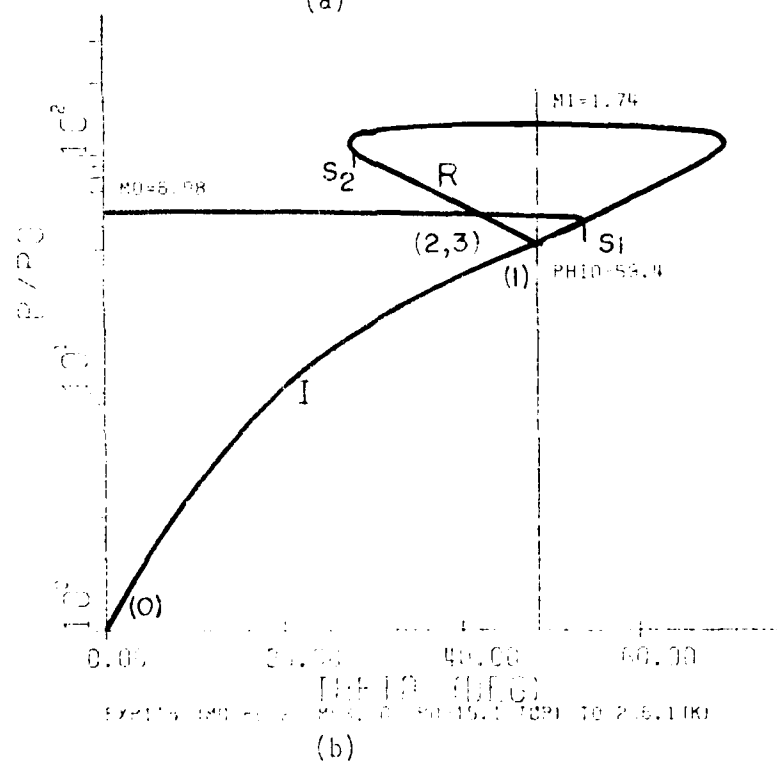
(a)

(b)

FIG. [...] [...], [...], M=[...], [...] 15.1 torr, T_0 = 296.1°K.

(a) [...] [...] (λ = [...]Å)
(b) [...] [...]

(a)

(b)

M1=2.22

M: 9.??

S₂

R

S₁

(2,3)

(I)   PHIO=54.9

I

(O)

Θ (DEG)

0.00   20.00   40.00   60.00   80.00

ρ/ρ_0

2
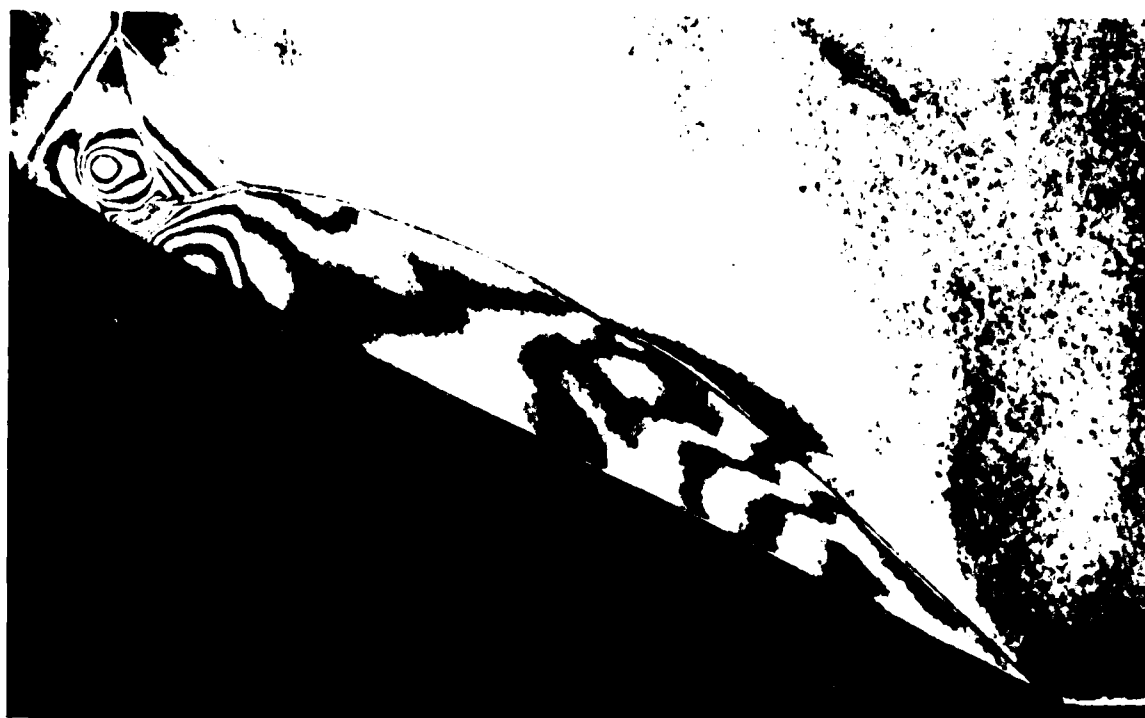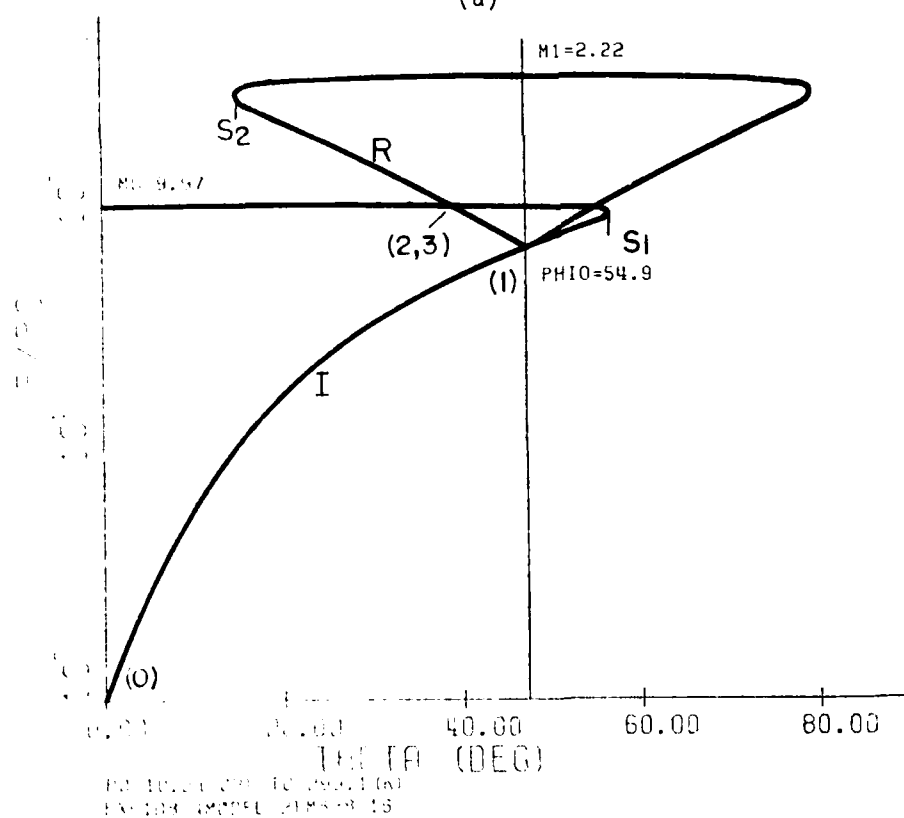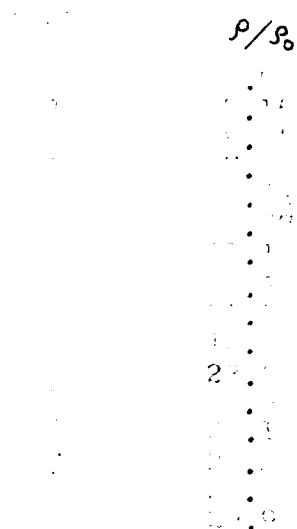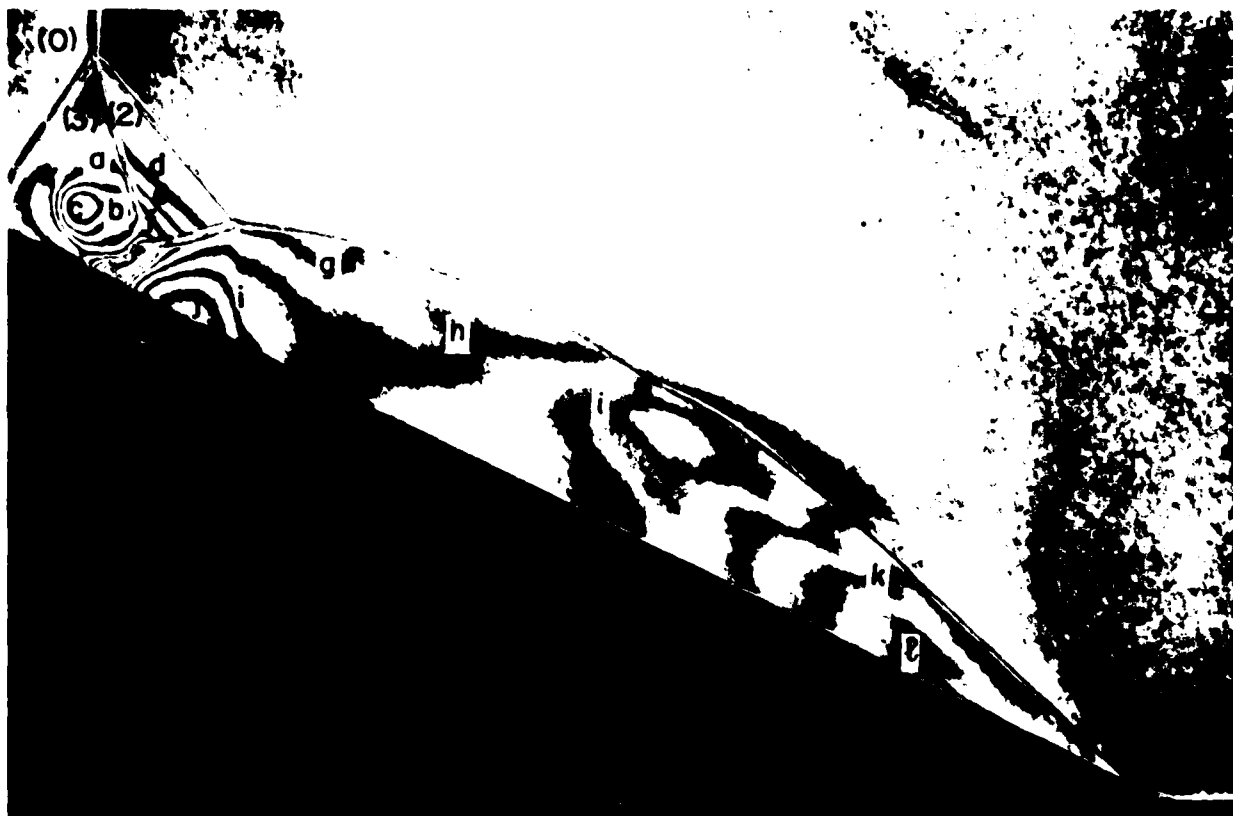
FIG. 17 - CONTINUED. N_2, $\alpha = 27.1°$, $P_0 = 10.2$ torr, $T_0 = 299.1°K$,
$\rho_0 = 0.0406 \times 10^{-7}$ g/cm^3.

(c) EVALUATION OF DENSITY FIELD

(a)
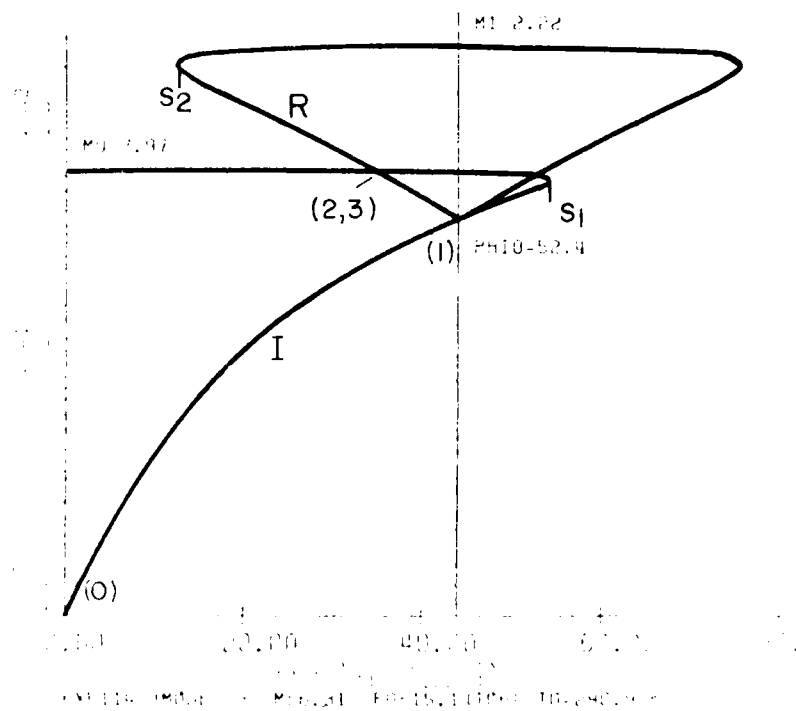
(b)

(a)

M1=2.46

S₂ R

MO=10.51

10^2

(2,3)

S₁

(1) PHIO=52.1

P/PO

I

10^1

10^0 (0)

0.00   20.00   40.00   60.00   80.00

THETA (DEG)

EXP 115 (MODEL 2) MS=8.30 PO=10.1(TOR) TO=297.5(K)

(b)
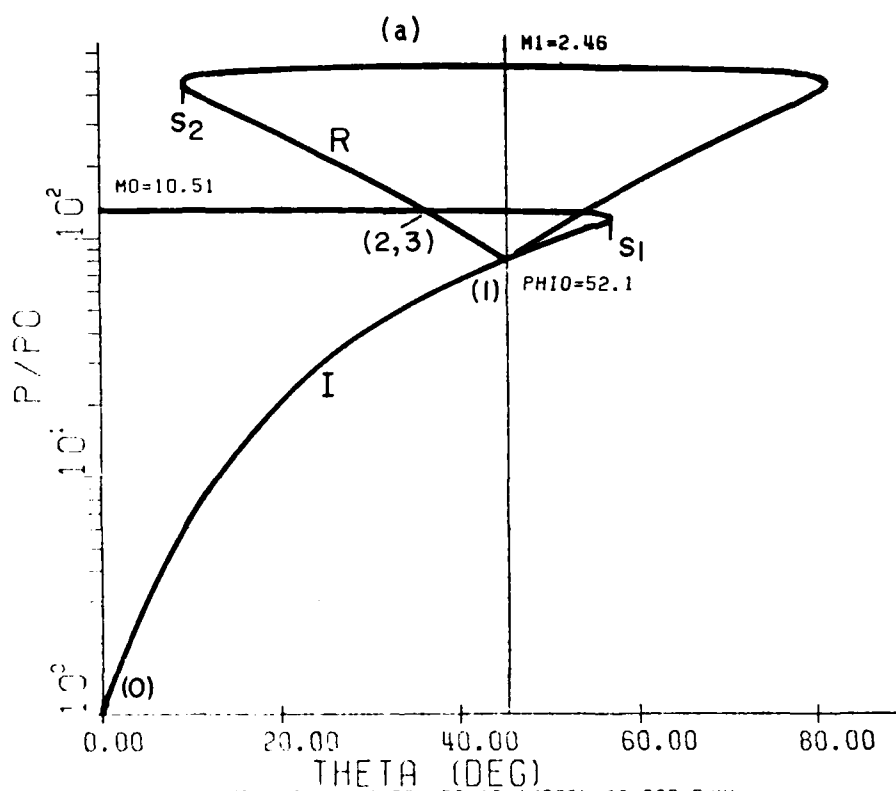
T: CO_2, $\theta_w = 30°$, $M_s = 8.30$, $p_0 = 10.1$ torr, $T_0 = 297.5°K$.

(a) INFINITE-FRINGE INTERFEROGRAM ($\lambda = 6943Å$)
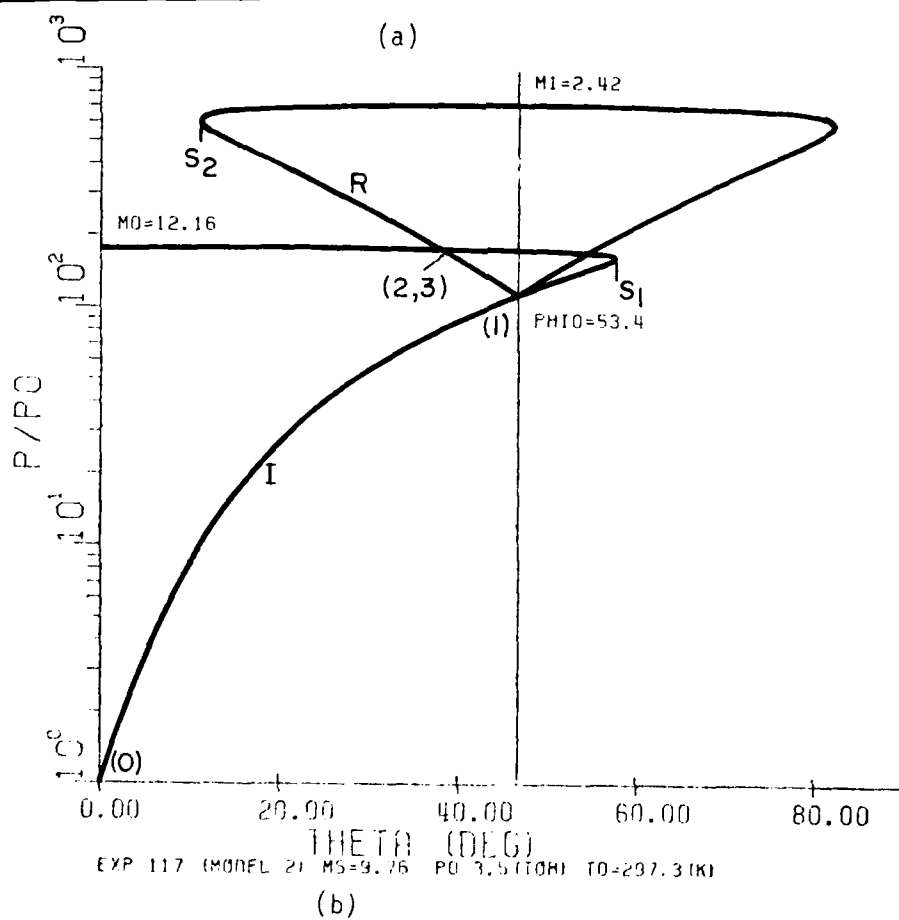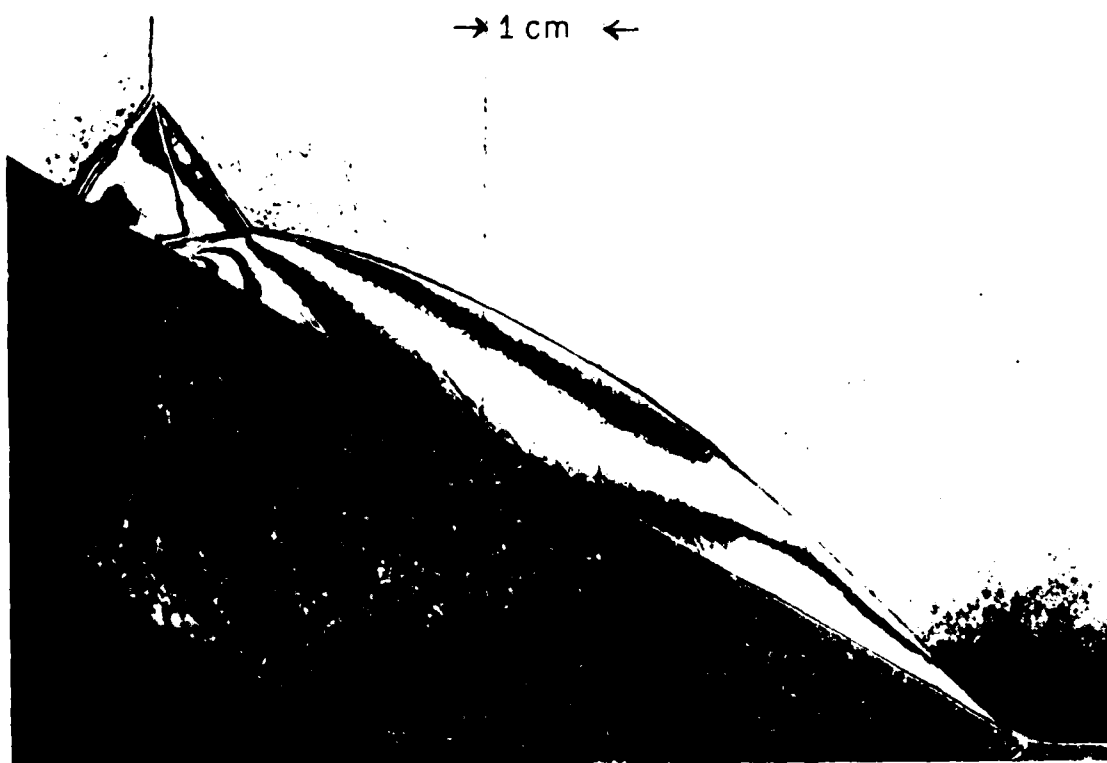
(b) ... THETA DIAGRAM

→1 cm ←

(a)

(b)

EXP 117 (MODEL 2) MS=9.76 P0 3.5(TORR) T0=297.3(K)
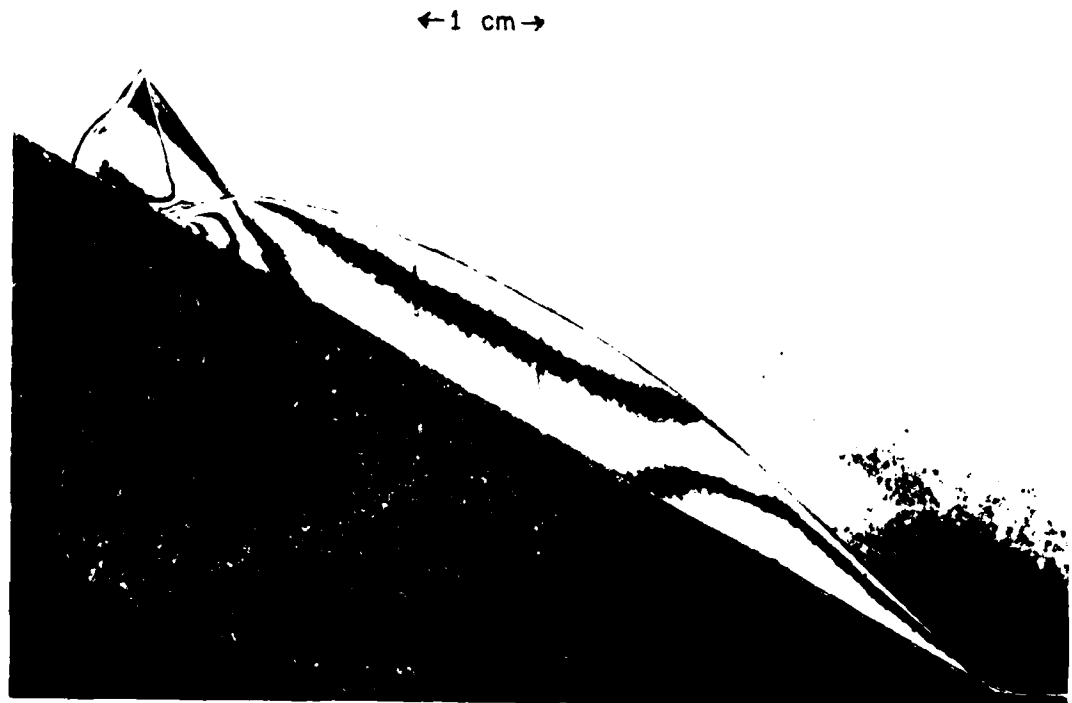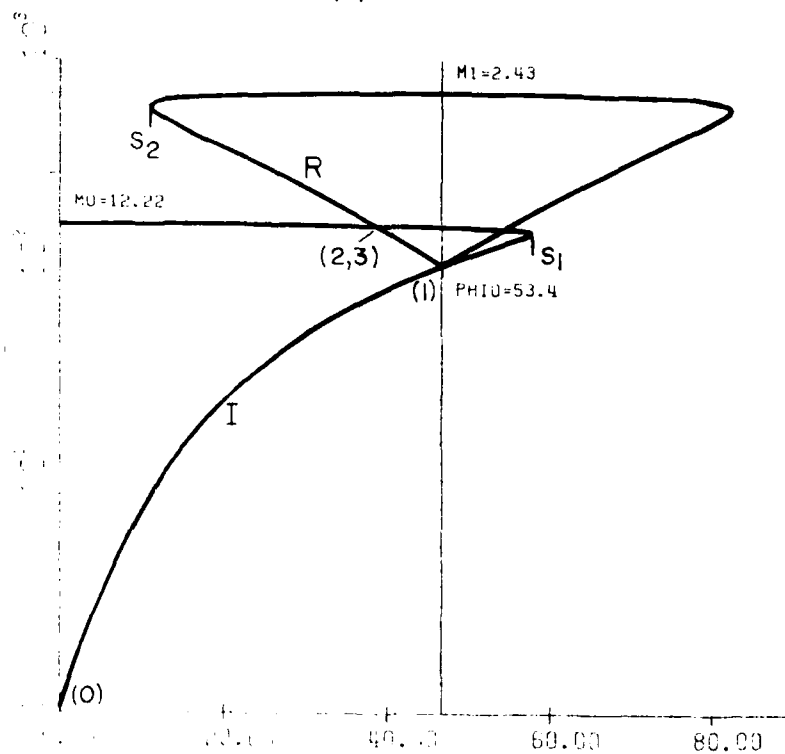
$M_1 = 2.42$

$M_0 = 12.16$

PHI0=53.4

← 1 cm →

(a)

M1=2.43

S₂

R

MU=12.22

(2,3)

S₁

(1) PHIO=53.4

I

(0)

40.0   60.00   80.00

DEPTH (DEG)

(b)

(a)

(b)

EXP 120 (MODEL 2) MS=10.17 PO=3.5 (TOR) T0=296.4 (K)

Fig. 2. CO_2, $M_0 = 11.84$, $M_1 = 1.97$, $P_0 = 3.5$ torr, $T_0 = 296.4$ K.

(a) COMPOSITE SCHLIEREN PHOTOGRAM (λ = 6943 Å)
(b) PRESSURE POLAR DIAGRAM

(0) (1)
(3) (2)
a
c d
e f
g

P/P_0

- - PROFILE - - D - - ... M. = 10.17, P_0 = 3.5 torr,

(e) EVALUATION OF DENSITY STEP
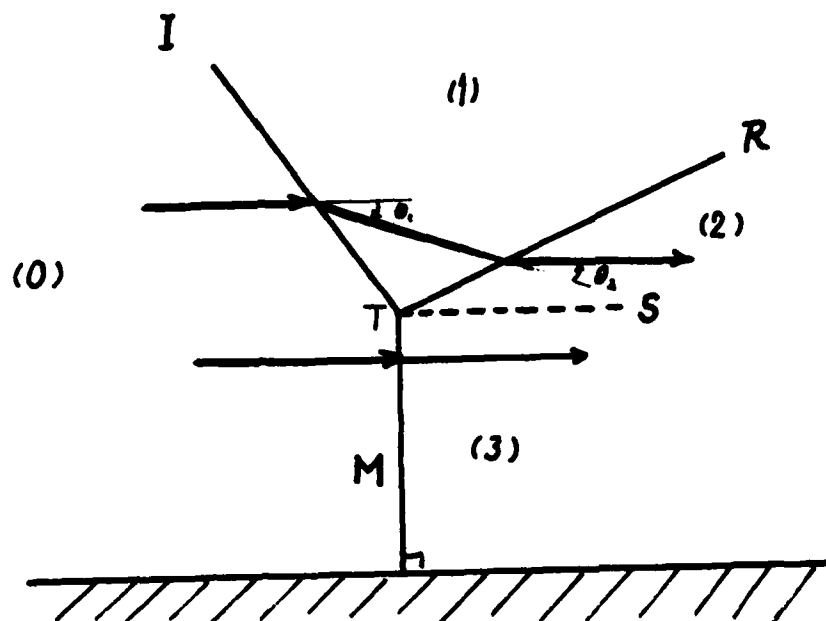
FIG. 33   STATIONARY MACH REFLECTION.

    I: INCIDENT SHOCK
    R: REFLECTED SHOCK
    M: MACH STEM
    S: SLIPSTREAM
    T: TRIPLE POINT
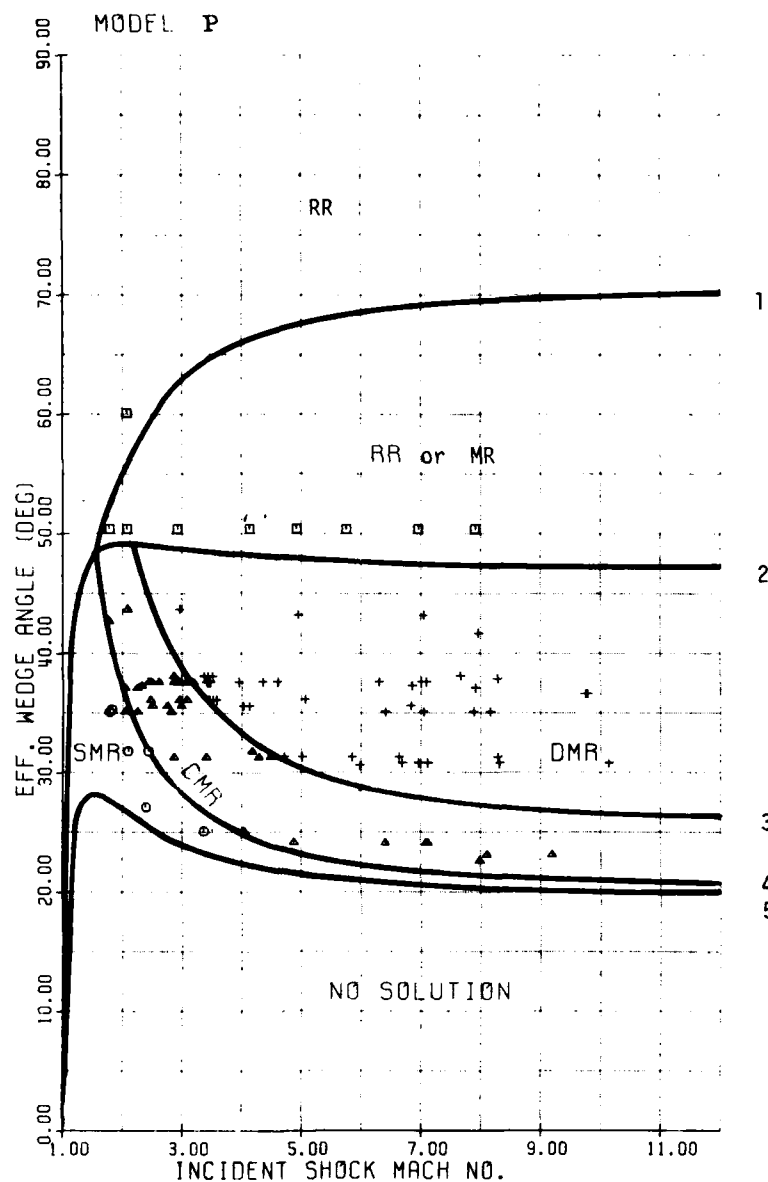
FIG. 34   COMPARISON OF PREDICTED REGIONS OF VARIOUS TYPES OF REFLECTION
AND EXPERIMENT.

(a) PERFECT CO_2: $\gamma = 1.290$ (MODEL P)

TRANSITION BOUNDARIES:

(1) THE VON NEUMANN CRITERION
(2) THE DETACHMENT CRITERION
(3) FLOW BEHIND THE REFLECTED SHOCK IS SONIC RELATIVE
     TO THE SECONDARY TRIPLE POINT
(4) FLOW BEHIND THE REFLECTED SHOCK IS SONIC RELATIVE
     TO THE PRIMARY TRIPLE POINT ($M_2 = 1$)
(5) THE EXTREME SONIC ANGLE ($M_1 = 1$)

TYPES OF REFLECTION: $\square$ = RR; $\circ$ = SMR; $\triangle$ = CMR; + = DMR.
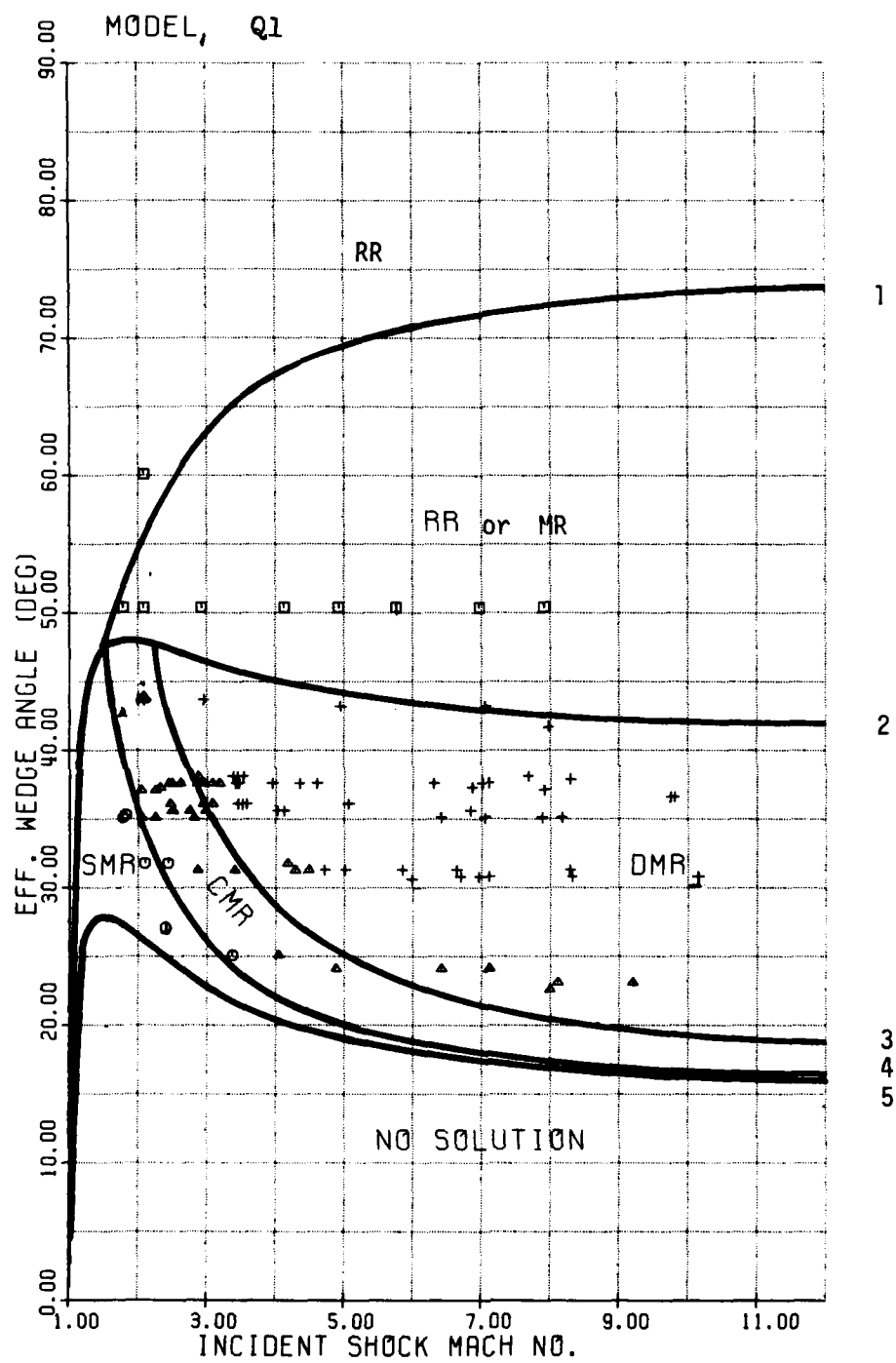
FIG. 34 - CONTINUED.

(b) QUASI-EQUILIBRIUM CO_2 (MODEL Q1).
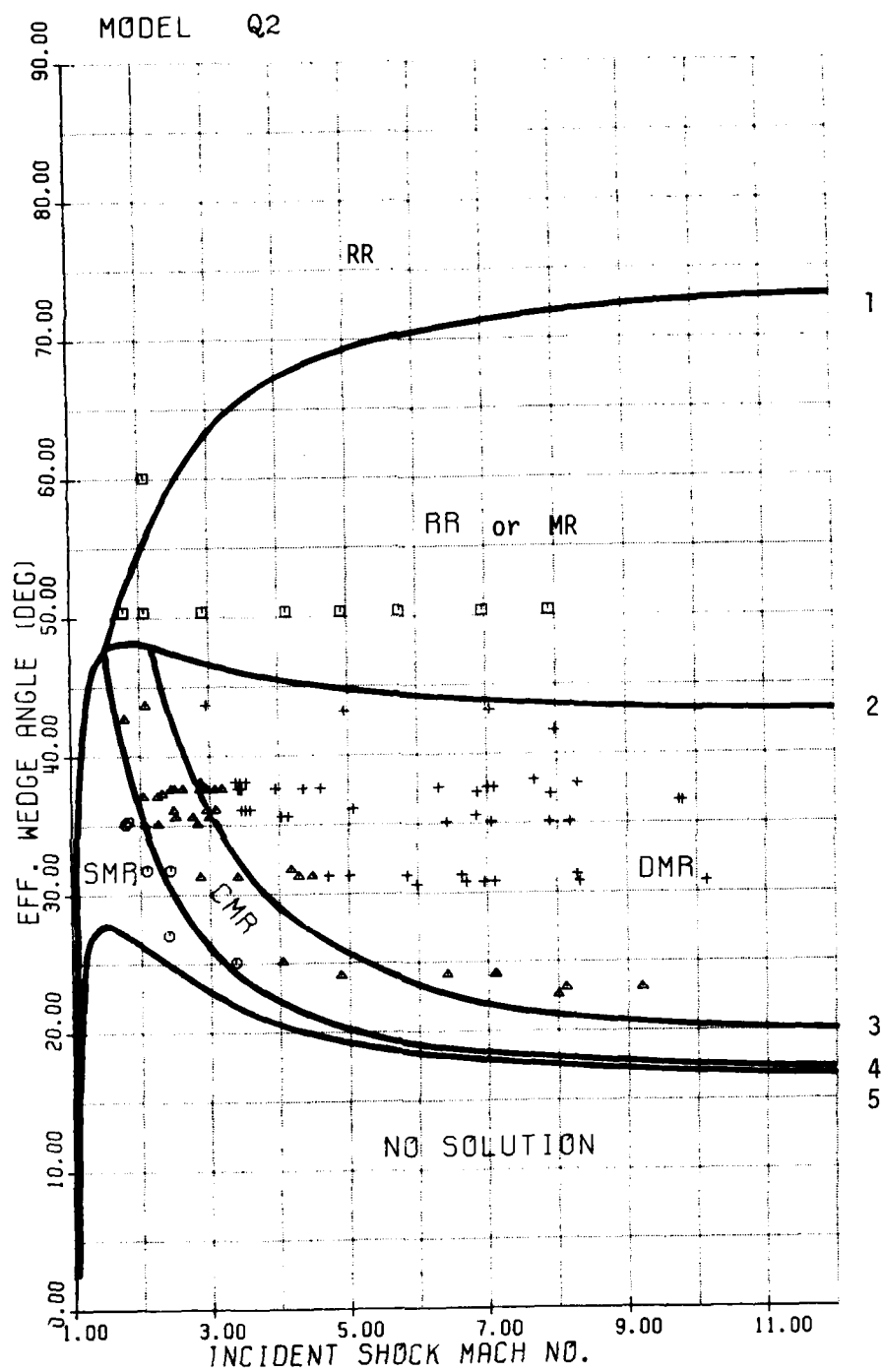
FIG. 34 - CONTINUED.

(c) QUASI-EQUILIBRIUM CO_2 (MODEL Q2)
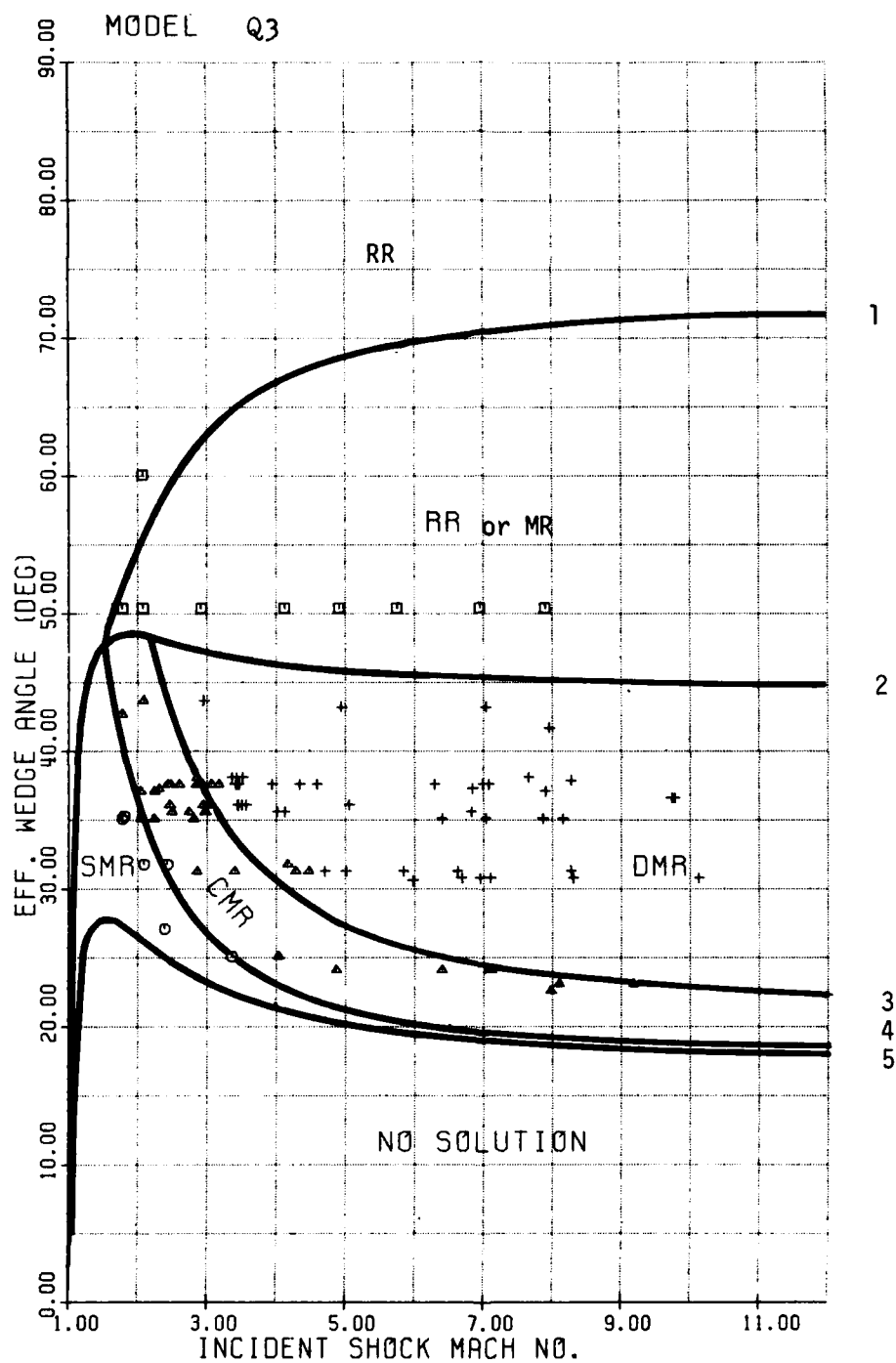
FIG. 34 - CONTINUED.

(d) QUASI-EQUILIBRIUM CO_2 (MODEL Q3)
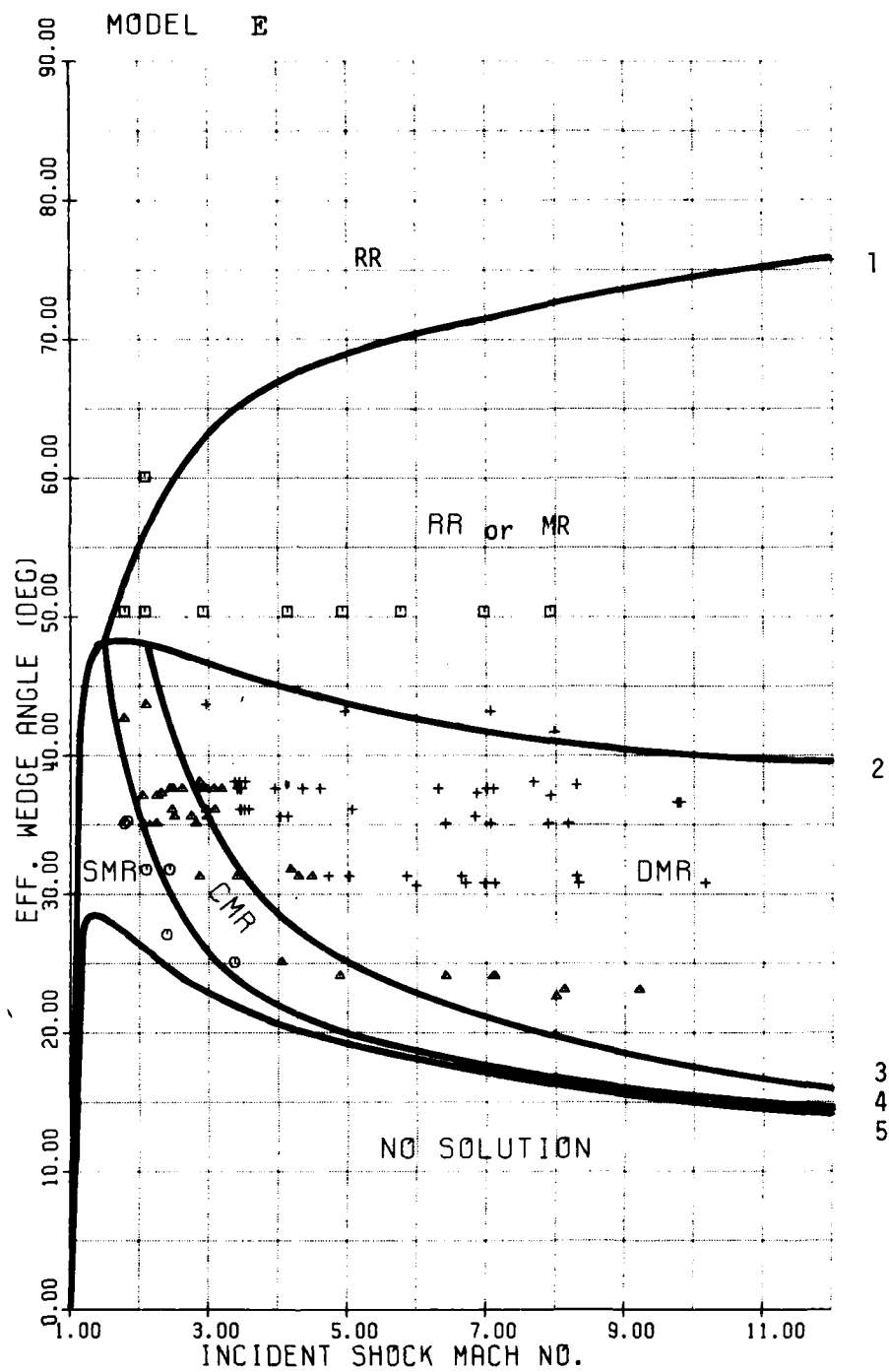
FIG. 34 - CONTINUED.

(e) EQUILIBRIUM CO_2 (MODEL E)
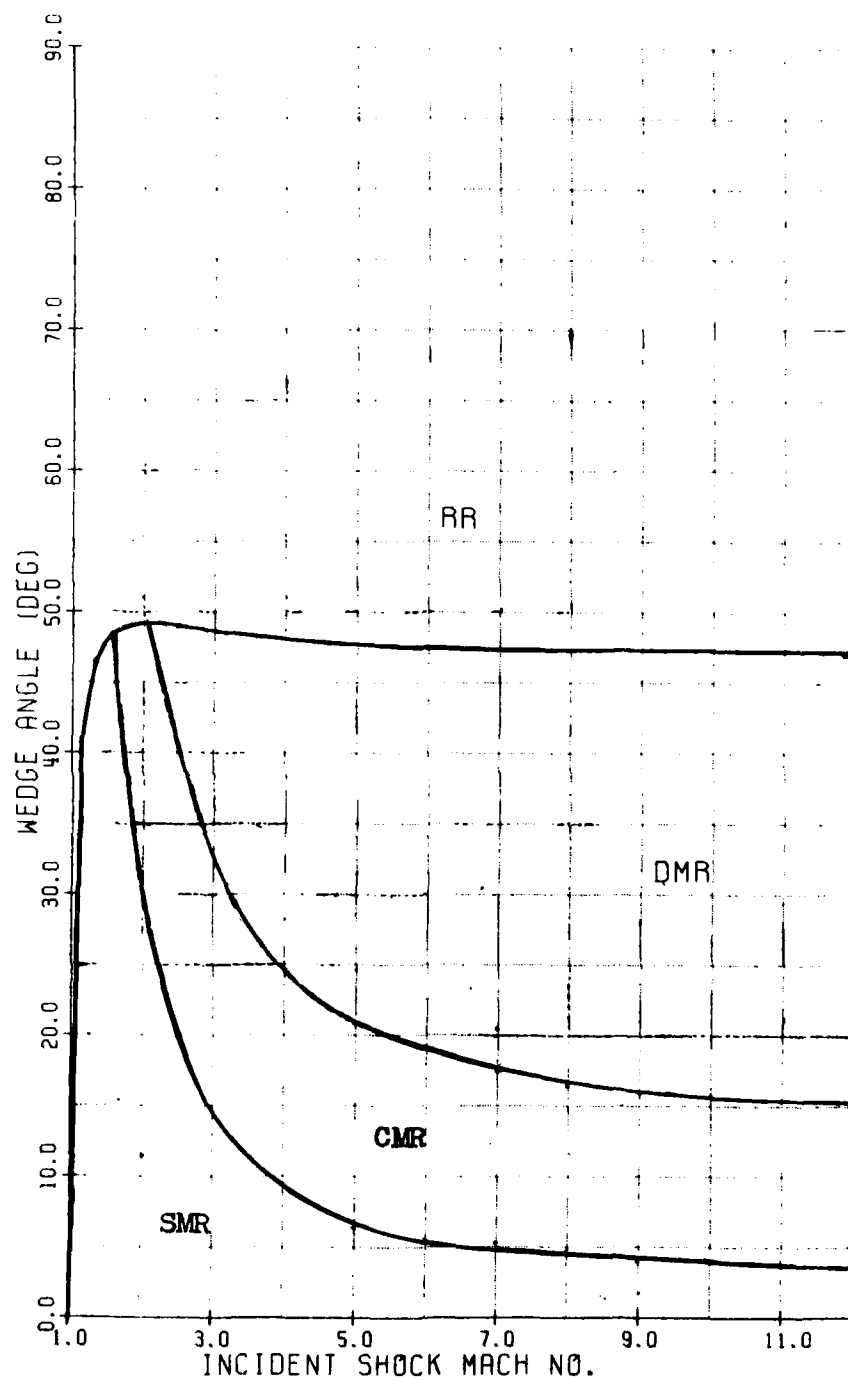
FIG. 35(a)   REGIONS OF VARIOUS TYPES OF REFLECTION IN THE SHOCK
            MACH NO. - ACTUAL WEDGE ANGLE PLANE (PERFECT CO_2
 $\gamma = 1.290$).
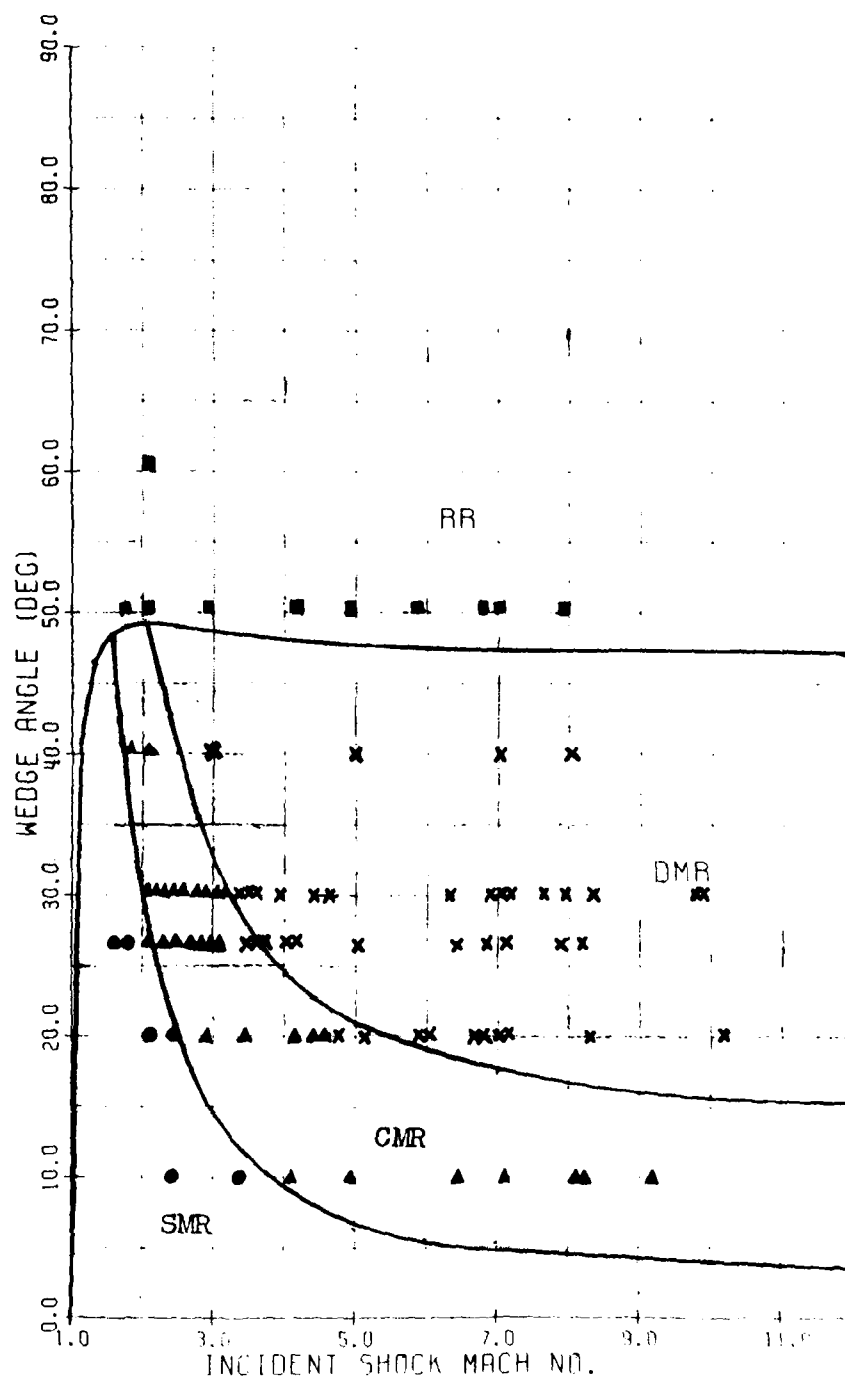
FIG. 35(b) COMPARISON OF PREDICTED REGIONS OF VARIOUS TYPES OF
REFLECTION AND EXPERIMENT IN THE SHOCK MACH NO. -
ACTUAL WEDGE ANGLE PLANE (PERFECT CO_2, $\gamma = 1.290$).

SYMBOLS: ■ = RR; ● = SMR; ▲ = CMR; x = DMR.
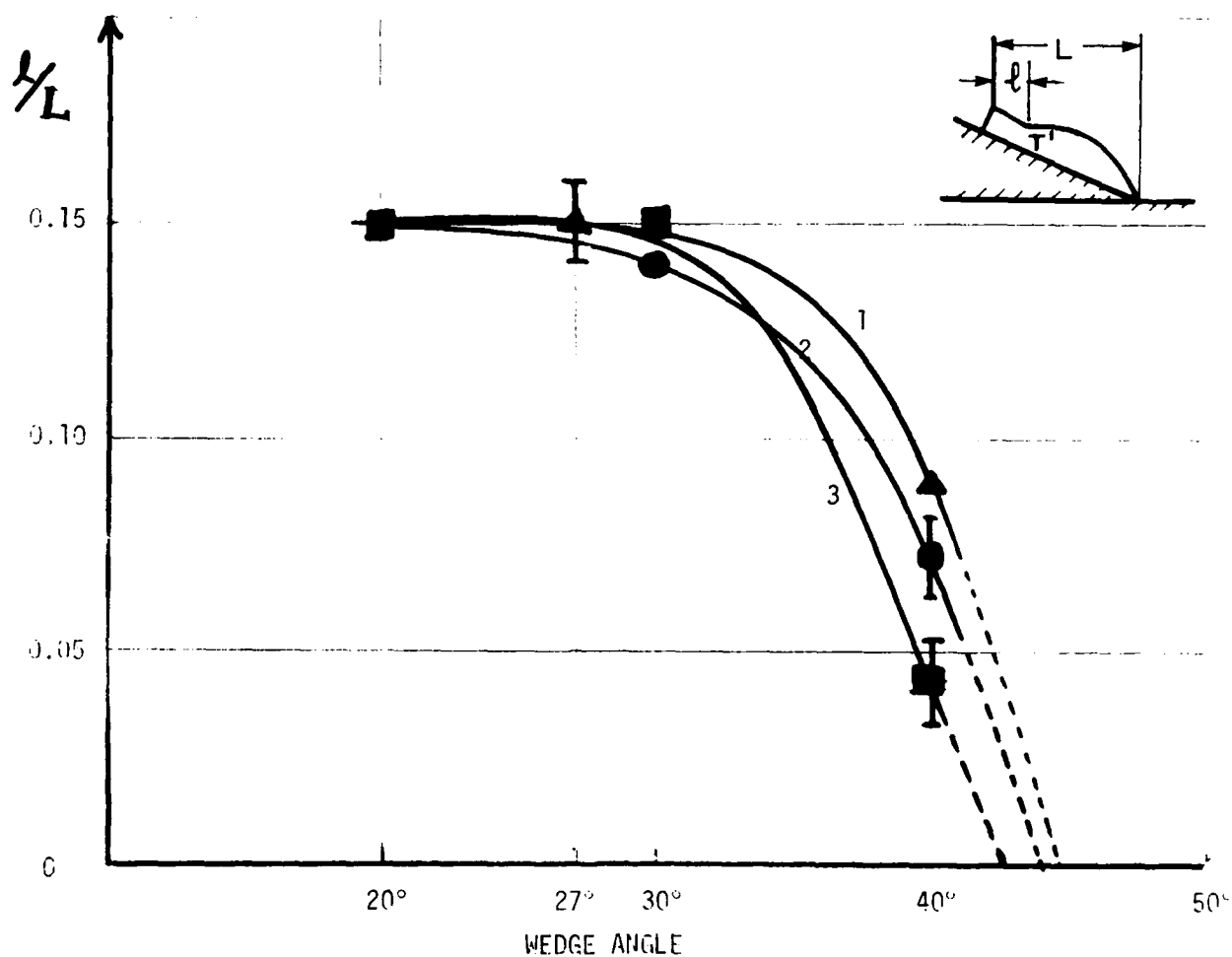
FIG. 36 MEASURED RATIO ℓ/L: CO_2

LINES: (1) $M_S = 5.00 \pm 0.07$
        (2) $M_S = 7.00 \pm 0.04$
        (3) $M_S = 8.15 \pm 0.15$

EXP	M_S	θ_W (°)	ℓ/L
49	5.05	20.3	0.15
96	5.07	27.1	0.15
58	4.99	40.2	0.09
53	7.01	20.3	0.15
25	7.04	30.1	0.14
150	7.04	40.2	0.07
121	8.33	20.3	0.15
115	8.30	30.1	0.15
151	8.00	40.2	0.04
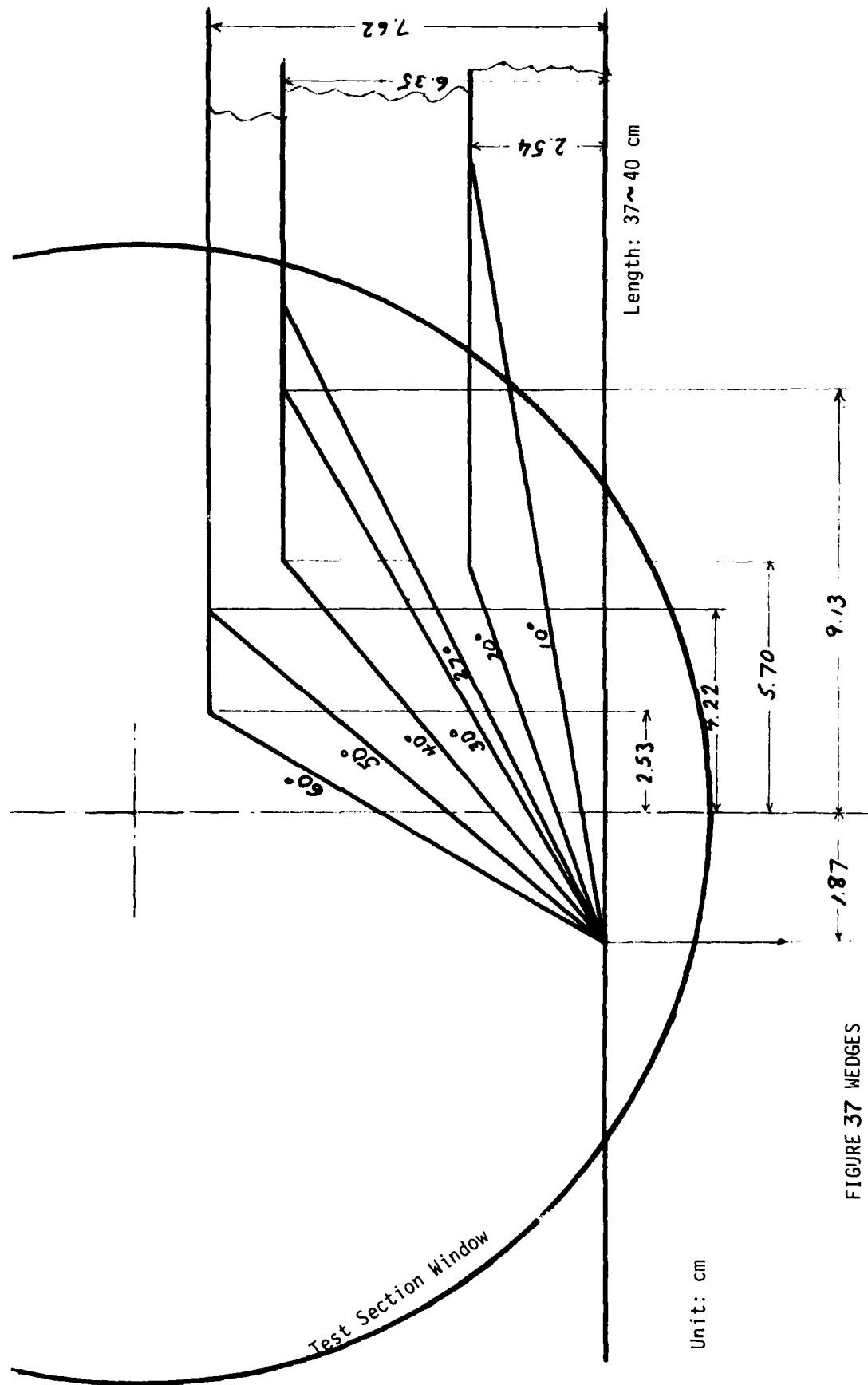
FIGURE 37 WEDGES

7.62

6.35

2.54

Length: 37~40 cm

9.13

5.70

4.22

2.53

1.87

60°

50°

40°

30°

20°

10°

0°

Test Section Window

Unit: cm

FIG. 3(b) THE TYPE OF FRINGES FOR A SUBSTANTIAL AIR DISPLACEMENT
(cf. FIG. 3a), SHOWING DETONATION.

θ_2, $w = 7°$, $M_1 = 1.4$, $p_1 = 50$ torr, $T_0 = 26.1°C$, $\lambda = 3472\text{Å}$.

TABLE 1   EXPERIMENTAL RESULTS: REGULAR REFLECTION.

EXP. NO.	V_s (m/s)	θ_w (°)	M_s	P_0 (tor)	T_0 (°C)	ω (°)
73	479.6	50.4	1.78	50.0	21.4	35.0
127	559.3	60.1	2.08	50.0	23.9	16.0
72	559.8	50.4	2.08	50.0	23.4	29.5
71	786.6	50.4	2.93	30.0	22.9	21.0
70	1112.4	50.4	4.14	15.0	22.7	16.0
69	1325.2	50.4	4.94	15.2	22.3	15.0
68	1551.2	50.4	5.78	15.2	22.9	14.0
66	1875.7	50.4	7.00	15.2	21.2	12.0
67	2131.3	50.4	7.96	10.2	21.8	13.0

SYMBOLS: EXP. NO.   = EXPERIMENT NUMBER
V_s (m/s)   = INCIDENT SHOCK VELOCITY
θ_w = WEDGE ANGLE
M_s = INCIDENT SHOCK MACH NUMBER
ω = ANGLE OF REFLECTION

TABLE 2 EXPERIMENTAL RESULTS: MACH REFLECTION.

EXP	TYPE	VS(M/S)	MS	PO(TOR)	TO(C)	AEDGE	CHI	TH..XSU	OMEGA
39	1	645.1	2.41	50.0	21.4	10.1	17.0	27.1	44.0
40	1	907.1	3.39	30.0	20.8	10.1	15.0	25.1	27.0
28	2	1088.6	4.07	14.9	20.8	10.1	15.0	25.1	17.5
29	2	1313.8	4.91	15.0	21.1	10.1	14.0	24.1	13.5
37	2	1726.9	6.45	15.2	21.6	10.1	14.0	24.1	9.0
124	2	1917.0	7.12	14.9	25.5	10.1	14.0	24.1	7.0
31	2	1911.0	7.14	14.8	21.3	10.1	14.0	24.1	6.0
32	2	2154.1	8.06	10.1	21.2	10.1	12.5	22.6	3.0
126	2	2185.0	8.14	10.1	23.7	10.1	13.0	23.1	-3.0
125	2	2478.0	9.22	5.1	23.8	10.1	13.0	23.1	-5.0
43	1	564.4	2.11	50.0	21.8	20.3	11.5	31.8	46.0
42	1	655.5	2.45	50.0	21.4	20.3	11.5	31.8	32.0
44	2	771.7	2.88	30.0	22.4	20.3	11.0	31.3	23.0
45	2	916.7	3.43	30.0	20.8	20.3	11.0	31.3	18.5
46	2	1124.7	4.21	15.2	21.2	20.3	11.5	31.8	1.0
122	2	1154.6	4.30	15.2	23.9	20.3	11.0	31.3	5.5
48	2	1207.1	4.52	15.2	20.8	20.3	11.0	31.3	1.5
147	3	1270.0	4.72	14.5	24.6	20.3	11.0	31.3	0.0
49	3	1351.7	5.05	15.2	21.4	20.3	11.0	31.3	-4.0
50	3	1575.2	5.88	15.2	22.2	20.3	11.0	31.3	-5.5
118	3	1612.7	6.01	15.1	23.0	20.3	10.3	30.6	-7.5
51	3	1787.7	6.68	15.2	22.0	20.3	11.0	31.3	-9.0
54	3	1803.6	6.73	15.2	22.0	20.3	10.5	30.8	-9.0
53	3	1875.7	7.01	15.2	21.8	20.3	10.5	30.8	-10.0
			7.24	15.2	23.6	20.3	11.5	30.8	-10.0
52	3	2233.0	8.34	10.1	21.7	20.3	11.0	31.3	-13.0
121	3	2241.2	8.33	10.1	24.4	20.3	10.5	30.8	-13.0
120	3	2733.6	10.18	3.5	23.3	20.3	10.5	30.8	-15.5
101	1	479.6	1.78	80.0	24.9	27.1	8.0	35.1	50.0
106	1	479.6	1.78	80.0	25.3	27.1	8.0	35.1	50.0
105	1	488.0	1.81	80.0	25.7	27.1	8.2	35.3	49.5
104	2	552.7	2.05	70.0	24.8	27.1	8.0	35.1	38.0
90	2	604.8	2.25	50.0	24.3	27.1	8.0	35.1	31.0
91	2	664.8	2.47	50.0	24.4	27.1	9.0	36.1	23.0
109	2	673.6	2.50	50.0	26.0	27.1	8.5	35.6	23.5
92	2	739.8	2.75	50.0	24.3	27.1	8.5	35.6	18.5
128	2	758.2	2.83	50.0	22.4	27.1	8.0	35.1	16.0
93	2	794.8	2.95	50.0	24.8	27.1	9.0	36.1	12.0
103	2	803.2	2.98	50.0	26.1	27.1	8.5	35.6	12.0
107	2	829.4	3.08	50.0	25.7	27.1	9.0	36.1	11.0
94	3	930.7	3.46	50.0	24.8	27.1	9.0	36.1	5.5
135	3	929.3	3.47	50.0	22.1	27.1	9.0	36.1	5.0
136	3	945.1	3.52	50.0	22.7	27.1	9.0	36.1	4.5
133	3	963.0	3.60	50.0	22.0	27.1	9.0	36.1	4.0
129	3	1084.7	4.05	14.5	22.2	27.1	8.5	35.6	2.0
95	3	1112.4	4.13	15.0	24.8	27.1	8.5	35.6	0.0
96	3	1363.8	5.07	15.2	24.5	27.1	9.0	36.1	-6.5
97	3	1726.9	6.42	15.3	24.5	27.1	8.0	35.1	-7.0
98	3	1841.7	6.84	13.5	25.0	27.1	8.5	35.6	-12.5
131	3	1899.1	7.08	13.5	22.6	27.1	8.0	35.1	-13.0
99	3	2124.0	7.89	10.0	24.9	27.1	8.0	35.1	-14.0
108	3	2200.7	8.16	10.2	26.0	27.1	8.0	35.1	-15.0

TYPE 1=SMR, 2=CMR, 3=DMR

TABLE 2 - CONTINUED.

EXP	TYPE	VS(M/S)	MS	PO(TOR)	TO(C)	WEDGE	CHI	EF.WDG	OMEGA
21	2	549.7	2.04	50.0	24.2	30.1	7.0	37.1	34.0
17	2	605.4	2.25	50.0	24.9	30.1	7.0	37.1	29.0
10	2	623.3	2.32	50.0	23.0	30.1	7.2	37.3	26.5
27	2	656.9	2.44	50.0	24.3	30.1	7.5	37.6	23.0
9	2	668.8	2.49	50.0	24.4	30.1	7.5	37.6	22.0
16	2	703.1	2.61	50.0	24.4	30.1	7.5	37.6	19.0
26	2	768.7	2.57	50.0	22.0	30.1	7.5	37.6	14.0
5	2	771.7	2.88	50.0	22.4	30.1	8.0	38.1	12.0
7	2	785.6	2.93	50.0	22.0	30.1	7.5	37.6	13.5
19	2	793.8	2.95	30.0	25.7	30.1	7.5	37.6	12.5
13	2	827.1	3.09	50.0	22.3	30.1	7.5	37.6	10.5
12	2	856.2	3.19	50.0	23.0	30.1	7.5	37.6	9.0
143	3	908.5	3.38	50.0	24.0	30.1	8.0	38.1	5.0
11	3	919.5	3.43	50.0	22.9	30.1	7.5	37.6	6.0
145	3	925.0	3.44	50.0	24.0	30.1	8.0	38.1	4.0
20	3	927.9	3.45	30.0	25.2	30.1	7.5	37.6	6.0
14	3	933.5	3.49	50.0	21.6	30.1	7.5	37.6	3.0
144	3	948.1	3.53	50.0	24.0	30.1	8.0	38.1	3.0
18	3	1053.4	3.97	13.2	21.8	30.1	7.5	37.6	0.0
22	3	1170.9	4.38	15.0	21.2	30.1	7.5	37.6	-3.0
4	3	1239.0	4.62	14.4	22.8	30.1	7.5	37.6	-2.5
114	3	1698.1	6.32	15.1	23.8	30.1	7.5	37.6	-10.5
23	3	1847.3	6.90	15.0	21.8	30.1	7.2	37.3	-12.5
25	3	1887.3	7.04	15.3	22.9	30.1	7.5	37.6	-13.5
140	3	1911.0	7.11	14.4	24.3	30.1	7.5	37.6	-13.0
24	3	2066.4	7.68	10.1	24.8	30.1	8.0	38.1	-14.0
146	3	2131.5	7.93	9.9	24.1	30.1	7.0	37.1	-13.5
141	3	2131.5	7.93	9.3	23.8	30.1	7.0	37.1	-13.5
115	3	2233.0	8.30	10.1	24.4	30.1	7.8	37.9	-15.
117	3	2627.6	9.77	3.5	24.2	30.1	6.5	36.6	-16.5
113	3	2627.6	9.78	3.4	23.8	30.1	6.5	36.6	-16.0
116	3	2639.0	9.82	3.5	24.1	30.1	6.5	36.6	-16.0
64	2	478.9	1.79	80.0	21.6	40.2	2.5	42.7	38.5
62	2	562.4	2.10	50.0	21.1	40.2	3.5	43.7	26.0
60	3	796.9	2.98	30.0	22.0	40.2	3.5	43.7	8.0
58	3	1333.9	4.99	15.2	20.9	40.2	3.0	43.2	-6.0
150	3	1899.1	7.04	11.2	26.2	40.2	3.0	43.2	-13.0
151	3	2146.5	8.00	8.7	23.2	40.2	1.5	41.7	-14.0

FORTRAN SYMBOLS:

EXP	EXPERIMENT NUMBER	
TYPE	TYPE OF REFLECTION: 1 = SMR, 2 = CMR, 3 = DMR	
VS(M/S)	INCIDENT SHOCK VELOCITY (M/S)	
MS	INCIDENT SHOCK MACH NUMBER: M_S	
PO(TOR)	P_0 (torr)	
TO(C)	T_0 (°C)	
WEDGE	WEDGE ANGLE (°)	
CHI	TRAJECTORY ANGLE χ OF THE TRIPLE POINT (°)	
EF.WDG	EFFECTIVE WEDGE ANGLE (°), $\theta_w' = \theta_w + \chi$	
OMEGA	ANGLE OF REFLECTION ω (°)	

TABLE B1 RELAXATION TIMES AND LENGTHS OF CO_2.

	P_1 tor	M_s	T °K			τ μs		ℓ cm	REF.
			(1)	(2)	(3)	(L)	(P)		
Vibration**	2.7	8.96	2520	2540	2315	13	155	3.1*	(21)
	3.5	8.84	2540	2500	2260	6	64	1.4*	(21)
	2.7	9.41	2730	2740	2400	1.4	16	0.4*	(21)
Dissociation	3.9	9.30	2730	2720	2390	110	1220	27.6*	(21)
	2.7	9.40	2730	2740	2400	85	950	21.6*	(21)
	3.0	7.5			1900	50*	650	12	(62)
	3.0	10			2400	30*	400	8	(62)

T(1)   MEASURED MAXIMUM TEMPERATURE
T(2)   TEMPERATURE FOR NO DISSOCIATION
T(3)   EQUILIBRIUM TEMPERATURE
τ(L)   LABORATORY TIME
τ(P)   PARTICLE TIME
ℓ RELAXATION LENGTH
*   CALCULATED BY THE PRESENT AUTHOR ON THE BASIS OF THE
    SOUND SPEED a = 270.2 M/SEC AT T = 300°K FOR CO_2
**   ASYMMETRICAL STRETCHING MODE (CHARACTERISTIC TEMPERATURE
    θ_3 = 3380.3°K)

TABLE C1 GLADSTONE-DALE CONSTANTS FOR NITROGEN [REPRODUCED FROM
          BEN-DOR & WHITTEN (10)].

constant \ gas	K_{m_1}	K_{a_1}	K_{m_2}	K_{a_2}	Z_1	Z_2
Nitrogen	0.2376 $\pm$ 0.03%	0.328 $\pm$ 1.7%	0.246 $\pm$ 0.03%	0.331 $\pm$ 2.5%	-0.0904	-0.0805

1) λ_1 = 6943Å
2) λ_2 = 3471.5Å

K_{m_1}, K_{a_1}, K_{m_2}, K_{a_2}, Z_1 AND Z_2 ARE ALL IN CM^3/G.

NB: SUBSCRIPTS:
     m = MOLECULAR
     a = ATOMIC
     1 = WAVELENGTH λ_1 = 6943Å
     2 = WAVELENGTH λ_2 = 3472Å

*TYPOGRAPHICAL ERROR; THE CORRECT VALUE IS -0.0850 (AUTHOR)

APPENDIX A

ANALYTICAL CONSIDERATION

In this appendix, analytical aspects of the shock reflection problems are reviewed. Inasmuch as only strong to very strong shocks are dealt with in the present experiments, the analyses of the problem involving weak and very weak shocks are precluded from consideration here. The theories and the method of solution, by which the predicted transition boundaries between various types of reflection are obtained will now be explained.

1. Pseudo-Stationary Flow

We first note an important property of the flow involving the reflection phenomenon of a planar shock at a compressive corner in a shock tube. From the theoretical point of view, the walls of the shock tube and the reflecting surface may be regarded to extend semi-infinitely, so that no characteristic length scale is involved in the flow. In addition, if the flow is considered two-dimensional, the entire configuration is observed to grow linearly with time*, and every elementary fluid particle in the flow moves away radially from the corner with a constant velocity particular to a particle [Bleakney & Taub (14)].

It is therefore possible to make the observed non-stationary phenomenon independent of time through the transformation

$$\xi = x/t \ , \ \eta = y/t$$

where x and y are Cartesian coordinates with origin at the corner, and t is measured from the instant the incident shock has struck the corner.

According to the principle of Galilean invariance, the basic laws of physics are identical in all reference systems that move with uniform velocity with respect to one another. Therefore, the two space coordinates x and y may be measured in any frame of reference that is moving with a constant velocity relative to the corner.

The streamlines in the $\xi - \eta$ plane in the cases of RR and MR are shown in Fig. Al, which is reproduced from Jones et al (7). $P = (u_1,o)$, where u_1 is the induced flow velocity behind the incident shock relative to the shock tube, indicates the point to which streamlines in the region behind the incident shock, undisturbed by the reflected shock, are directed in this frame of reference. It should be borne in mind that relative orientation of each streamline to the shocks varies if the frame of reference is changed via a Galilean transformation.

2. The Simple Two-Shock and Three-Shock Theories

If the frame of reference is attached to the confluence point of the discontinuities, the directions of the flow in the angular regions

---

*For example, Gvozdeva & Predvoditeleva (25) determined the configuration to be self-similar to an accuracy of up to 3% using a high-speed camera.

delineated by the discontinuities become uniform in the sense that all the streamlines in a region have the same direction; and it becomes possible to apply the oblique shock relations across each shock subject to the following simplifying assumptions:

1) All the discontinuities are plane in the vicinity of the confluence point.
2) The gas is ideal so that transport phenomena such as viscosity and heat transfer may be neglected.
3) The flow variables are constant in each of the angular region around the confluence point.

The flow properties of each region are found algebraically by successive applications of the oblique shock relations to each shock until the following boundary conditions are satisfied:

For two-shock interactions, it is required that the flow deflections across the incident and reflected shocks be equal and opposite;

For three-shock interactions, it is required

1) That the total flow deflection across the incident and reflected shocks be equal to the flow deflection across the Mach stem;
2) That pressures across the slipstream be equal.

3. Method of Solution

Normal shock relations [Liepmann & Roshko (44)]

$$\rho_a u_a = \rho_b u_b$$

$$P_a + \rho_a u_a^2 = P_b + \rho_b u_b^2$$

$$h_a + (1/2)u_a^2 = h_b + (1/2)u_b^2$$

where subscripts a and b refer to the states ahead of and behind the shock, respectively, u is the component of flow velocity normal to the shock, and h enthalpy. The equations of state applied to each shock are in the forms:

$$\rho = \rho(P,T), \quad h = h(P,T)$$

where P is the pressure and T the temperature.

In the case of a perfect gas with a constant specific heat ratio, the above relations may be reduced to closed forms, the Rankin-Hugoniot relations. In the case of real gases, however, recourse to the method of successive approximation must be taken. In the present study, the iterative procedure in terms of ρ_b is continued until successive values of ρ_b are within 0.05% in the case of the quasi-equilibrium models for equations of state, and 0.5% in the case of the complete equilibrium model. Figure A2 shows the

wave angle-flow deflection angle diagrams for the various models of equations of state.

The real-gas effect is immediately seen in terms of the greater flow deflection angles θ_1 for real-gas models (Models E, Q1, Q2 and Q3) in Fig. A2. For example, the difference in θ_1 between the two extremes - the equilibrium model (Model E) for which θ_1 is greatest and the perfect-gas model (Model P) for which θ_1 is least for a given incident flow Mach number M_0 - amounts to as much as approximately 9° for $M_0 = 10$. This is a direct consequence of the absorption of heat by the internal degrees of freedom of the gas in the real-gas model. An increase in the number of degrees will result in a decrease in the temperature ratio T_1/T_0, and hence, an increase in the compression ratio ρ_1/ρ_0 across the shock for identical initial conditions. From the expression for the flow deflection angle θ_1 obtainable from the oblique-shock relations after a little manipulation

$$\theta_1 = \phi_0 - \arctan[(\rho_0/\rho_1)\tan\phi_0]$$

where ϕ_0 is the flow angle, it is obvious that, for an identical initial condition, the greater the compression ratio (i.e., the more internal degrees of freedom are taken into account), the greater the flow deflection angle. This effect may be visualized from the standpoint of the flow velocity, since its component parallel to the shock is identical on either side of the shock irrespective of the model of equation of state for an identical initial condition, while its component normal to the shock decreases according to the number of the internal degrees of freedom is increased.

These solutions are again iterated in terms of ϕ_1 in the case of two-shock interactions, or in terms of ϕ_1 and ϕ_3 in the case of three-shock interactions until

$$|1 - \theta_2/\theta_1| < 0.2 \times 10^{-2}$$

in the case of two-shock interactions, or

$$|1 - (\theta_1 - \theta_2)/\theta_3| < 0.2 \times 10^{-2}$$

and

$$|1 - P_3/P_2| < 0.5 \times 10^{-3}$$

in the case of three-shock interactions, where ϕ_i, θ_i and P_i are the wave angle, flow deflection angle, and pressure of region i (see Figs. 5 and 10).

FIG. A1 THE PSEUDO-STATIONARY FLOW IN THE ξ-η PLANE [AFTER JONES ET AL (7)].

(a) REGULAR REFLECTION
(b) MACH REFLECTION

WAVE ANGLE (DEG)

MO=1.1
MO=1.2
MO=1.3
MO=1.5
MO=1.6
MO=1.7
MO=1.8
MO=1.9
MO=2.0
MO=2.2
MO=2.4
MO=2.6
MO=2.8
MO=3.0
MO=6.0
MO=9.0
MO=10.0

DEFLECTION ANGLE (DEG)

θ_1
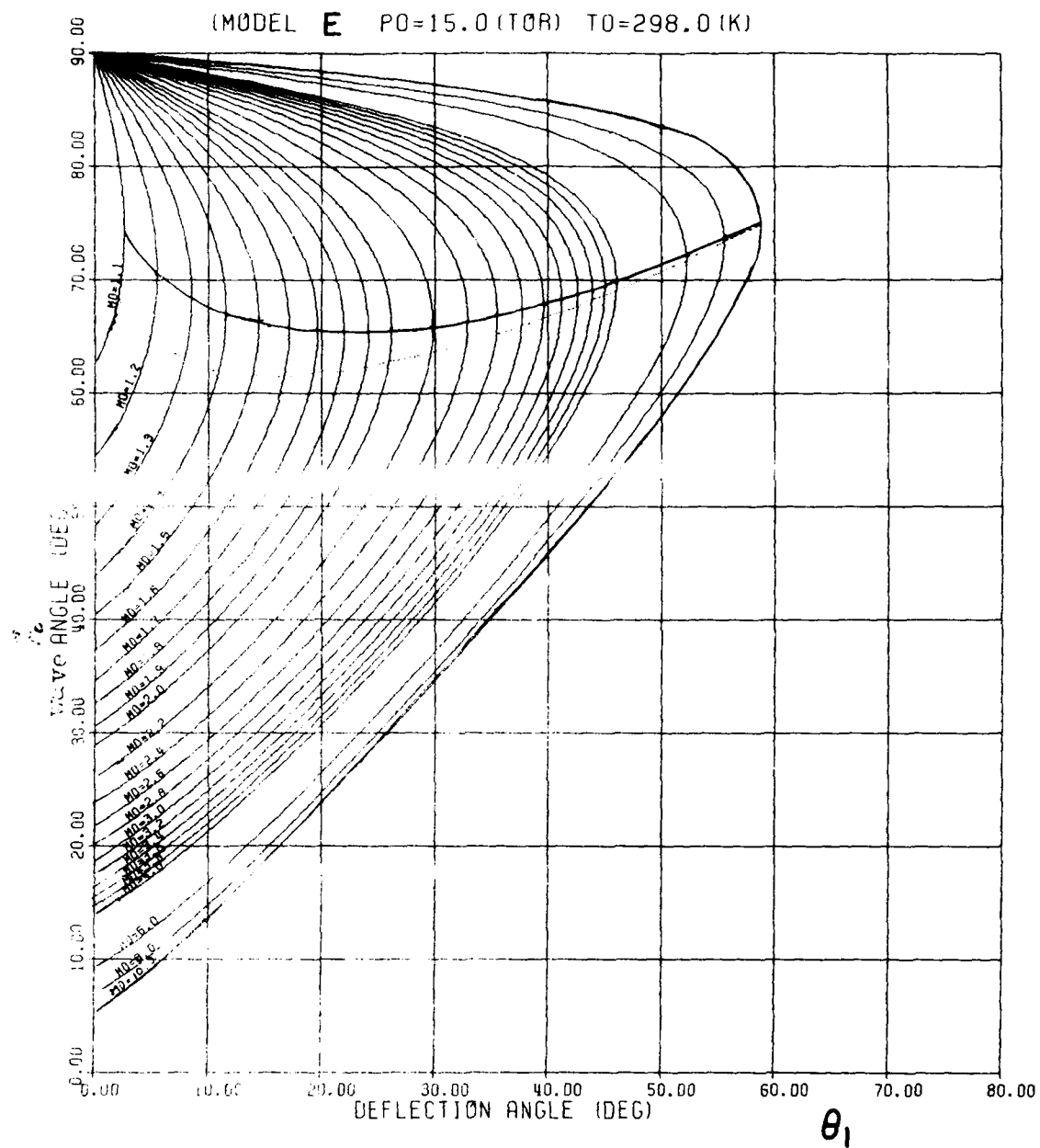
FIG. A2 WAVE ANGLE - FLOW DEFLECTION ANGLE DIAGRAM.

(a) EQUILIBRIUM CO_2 (MODEL E)

——— $\theta_1 = \theta_{1max}$

— — — $M_1 = 1$

M_0 M_1

SHOCK

(MODEL **Q1** PO=15.0(TOR) TO=298.0(K)

FIG. A. - CONTINUED.

(b) QUASI-EQUILIBRIUM CO$_2$ (MODEL Q1)

(MODEL Q2 PO=15.0(TOR) TO=298.0(K))
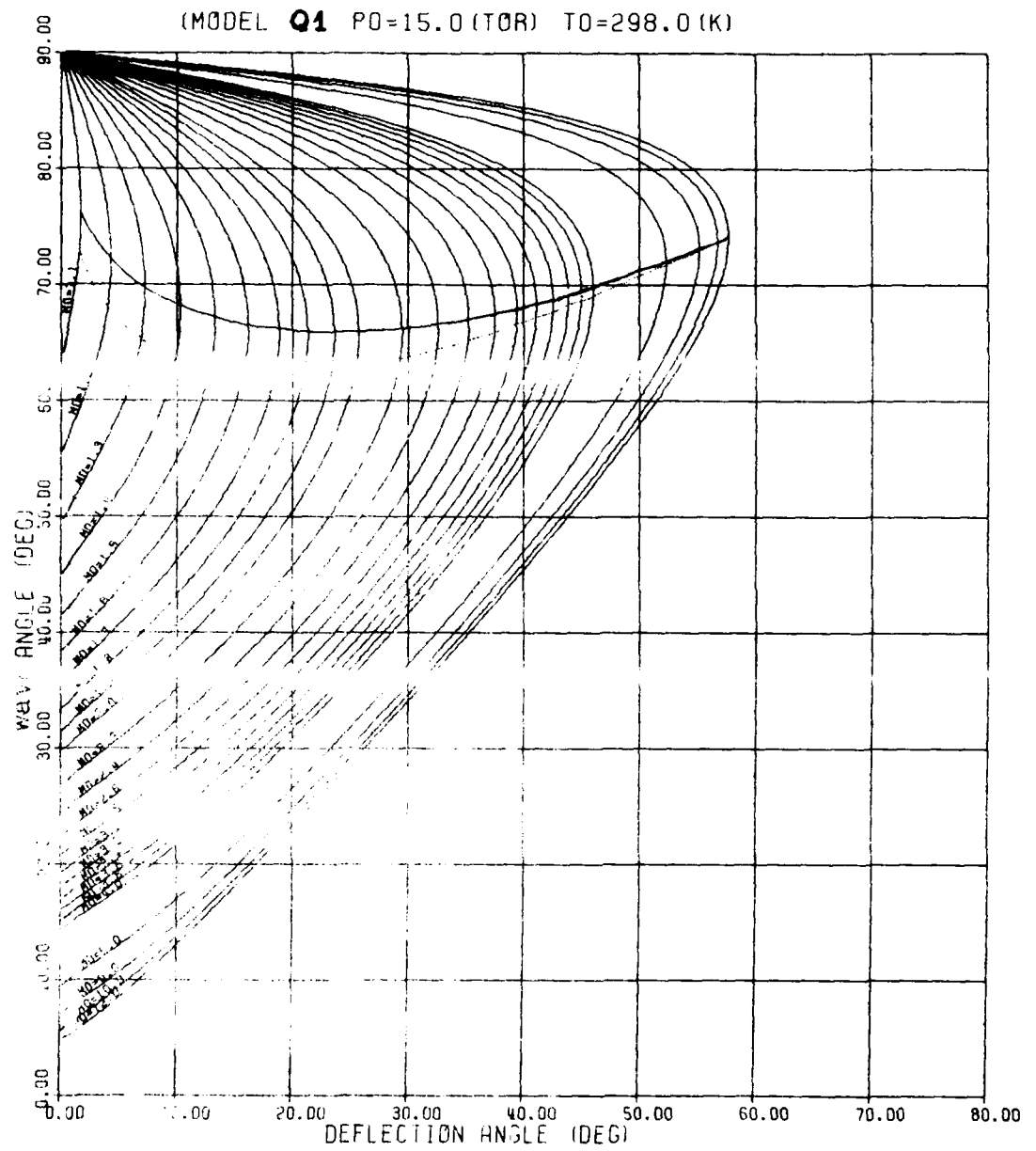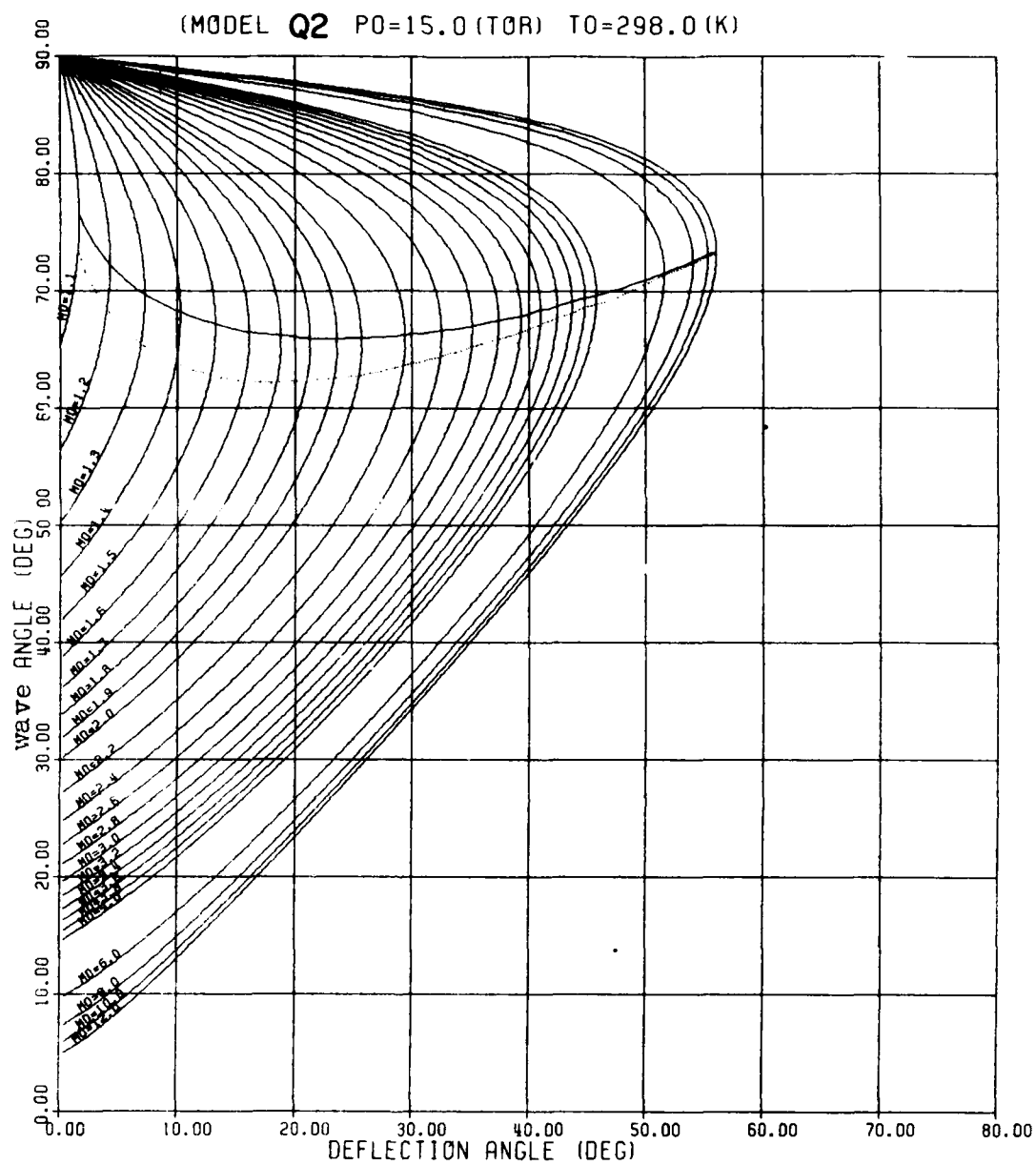
FIG. A2 - CONTINUED.

(c) QUASI-EQUILIBRIUM CO$_2$ (MODEL Q2)

(MODEL **Q3** PO=15.0(TOR) TO=298.0(K)
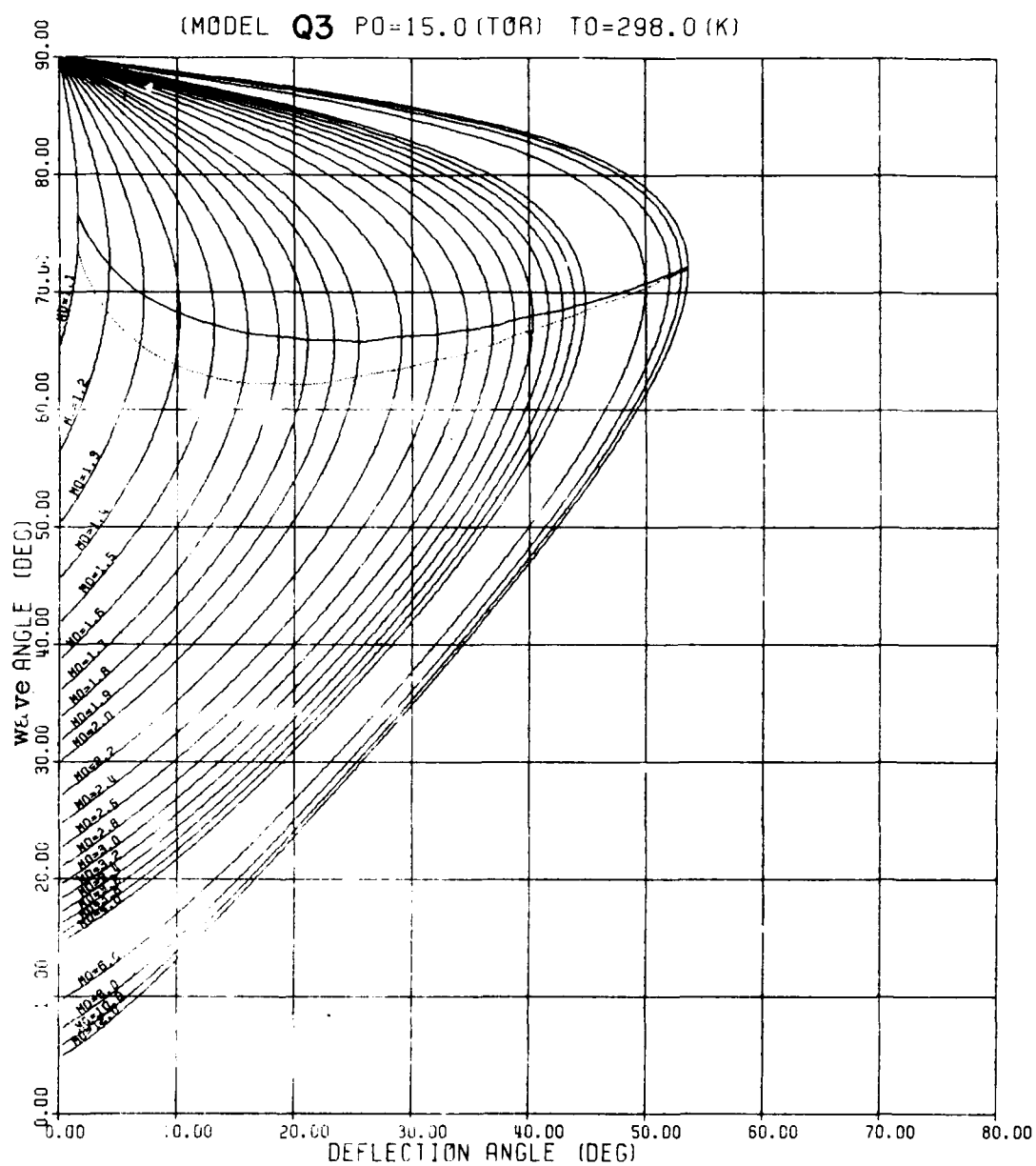
FIG. 42 - CONTINUED.

(d) QUASI-EQUILIBRIUM CO$_2$ (MODEL Q3)

AD-A108 553   TORONTO UNIV DOWNSVIEW (ONTARIO) INST FOR AEROSPACE --ETC F/8 20/4
                   PSEUDO-STATIONARY OBLIQUE SHOCK-WAVE REFLECTION IN CARBON DIOXI--ETC(U)
                   APR 81 S ANDO   AFOSR-77-3303
UNCLASSIFIED   UTIAS-TN-231   AFOSR-TR-81-0807   NL

END
DATE
FILMED
2-82
DTIC

1.0

1.1

1.25 1.4 1.6

2.8 2.5
3.2 2.2
3.6
4.0 2.0

1.8
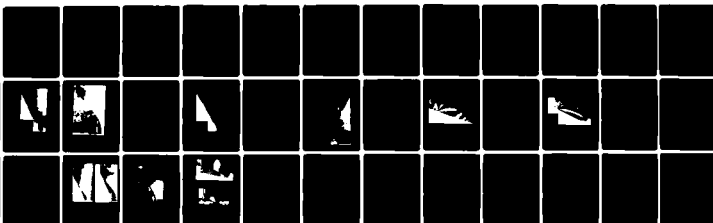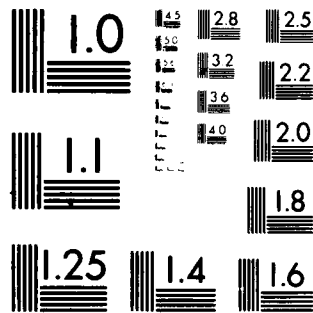
MICROCOPY RESOLUTION TEST CHART
NATIONAL BUREAU OF STANDARDS 1963 A
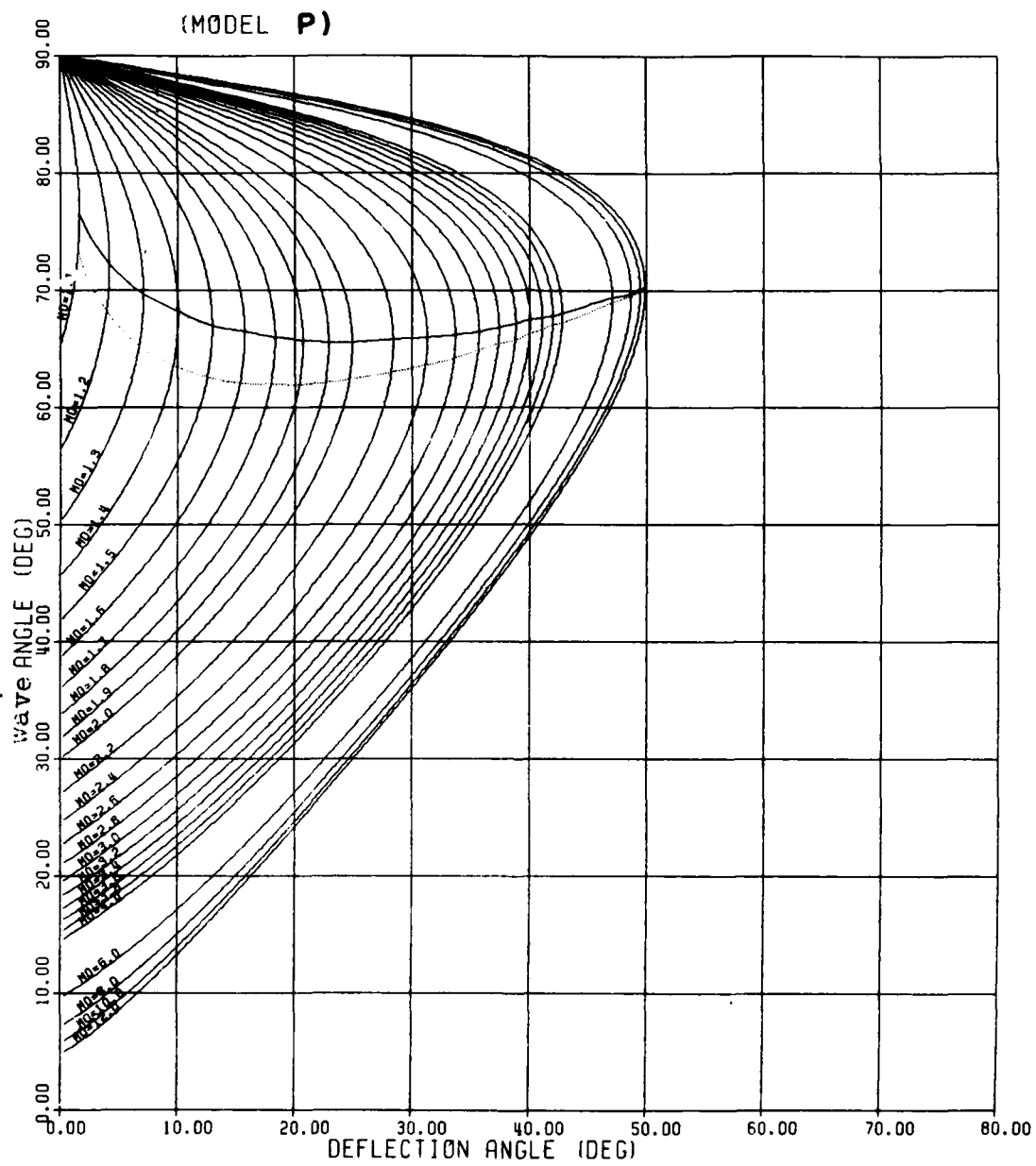
(MODEL **P**)

FIG. A2 - CONTINUED.

(e) $\gamma = 1.290$ (MODEL P)

APPENDIX B

THERMODYNAMIC STATES OF CO_2

With the steady advancement in space exploration technology in recent times, it is no longer beyond the realm of possibility to send spacecraft to other planets, and CO_2 has been gaining a new significance; for example, studies on entry probes with pure CO_2 as a model for Martian and Venusian atmospheres have been undertaken in the last decade [see Miller & Wilder (47)].

Consisting of linear triatomic molecules, CO_2 is one of the simplest of the polyatomic gases. It is in part owing to this fact that a considerable number of research papers concerning the vibrational relaxation phenomena of CO_2 have been published in the past, some of which were cited in Section 6.

CO_2 has four vibrational modes: doubly-degenerate bending modes ($\theta_2 = 960.2°K$), the symmetrical stretching mode ($\theta_1 = 1932.2°K$), and the asymmetrical stretching mode ($\theta_3 = 3380.3°K$), where θ is the characteristic temperature related to the characteristic frequency ν of oscillation of the vibrational mode by $\theta = h\nu/kT$, where h is Planck's constant, k is Boltzmann's constant, and T is the translational temperature. As can be found from the harmonic oscillator approximation for the vibrational specific heat, $C_{vib}/R = (\theta/T)^2 \exp(\theta/T)/[\exp(\theta/T) - 1]^2$, the contribution to the specific heat at room temperature by the doubly-degenerate bending modes amounts to 0.9R, where R is the gas constant. (The valence modes contribute 0.07R.) Thus, as demonstrated by Bazhenova et al (3), it is not realistic to set the frozen specific-heat ratio γ of CO_2 to 1.4, the value obtained when the vibrational energy contributions are ignored. Considering the fact that the isentropic exponent γ_E of CO_2 at 300°K is 1.286 (Ref. 46), γ was set to be 1.290 in this study.

In conjunction with the simple two-shock and three-shock theories, the following models for equations of state were employed to compute the thermodynamic properties of the gas in the regions around the confluence point:

(1) Equilibrium Model (Model E)

The gas is considered to be always in equilibrium including dissociation but not electronic excitation or ionization which are negligible over the shock Mach number range of the present experiments ($1.8 < M_s < 10.2$). Mole fractions of five species (CO_2, CO, O_2, O, and C) were computed by the method of White et al (37) on the digital computer. The expression for various partition functions and concomitant data of Allison (38), and Allison & Newman (39) were used. The computed values were checked against and found to be within a fraction of a percent of the corresponding values listed in Miller & Wilder (40).

In this model, therefore, the gas is considered to readjust to a new equilibrium state infinitely fast behind each shock around the triple point.

(2) Quasi-Equilibrium Models (Models Q1, Q2, and Q3)

As seen in Table B1, near the upper limit of the shock-Mach-number range of the present experiments, where the effects of dissociation may become significant, the dissociation relaxation time is at least an order of magnitude larger than the vibrational relaxation time. It may therefore be assumed that the vibrational relaxation is complete before dissociation becomes significant. (Dissociation of CO_2 is negligible below 1900°K.) Thus, it is meaningful to define quasi-equilibrium states in which no dissociation occurs but one or more vibrational modes are in equilibrium [see, e.g., Griffith & Kenney (24)]. In light of the fact that the characteristic temperature for the asymmetrical stretching mode is almost twice the value for the symmetrical stretching mode which in turn is double the value for the bending modes, three models with various excited vibrational modes are employed, and respective enthalpies h for given pressure P and temperature T are obtained as follows:

(a) Model Q1 (all four vibrational modes are fully excited).

$$h = \frac{7}{2} RT + RT \left[\frac{2\theta_2/T}{\exp(\theta_2/T) - 1} + \frac{\theta_1/T}{\exp(\theta_1/T) - 1} + \frac{\theta_3/T}{\exp(\theta_3/T) - 1} \right]$$

(b) Model Q2 (the asymmetrical stretching mode, which has the highest characteristic temperature, is unexcited, while the symmetrical stretching mode and the bending modes are fully excited).

$$h = \frac{7}{2} RT + RT \left[\frac{2\theta_2/T}{\exp(\theta_2/T) - 1} + \frac{\theta_1/T}{\exp(\theta_1/T) - 1} \right]$$

(c) Model Q3 (the valence modes are unexcited, and only the bending modes, which have the lowest characteristic temperature, are fully excited).

$$h = \frac{7}{2} RT + RT \left[\frac{2\theta_2/T}{\exp(\theta_2/T - 1} \right]$$

For these models, the equation of state for a thermally perfect gas,

$$P = \rho RT$$

is applicable because dissociation is assumed absent.

(3) Perfect-Gas Model (Model P)

In this model, the relaxation is considered to take place infinitely slowly, so that the thermodynamic states of the gas in all the regions around the confluence point are given by the perfect-gas equations of state with a constant specific heat ratio $\gamma = 1.290$:

$$P = \rho RT$$

$$h = [\gamma/(\gamma - 1)]RT$$

Figures B-1a through B-13 show the comparison of the predicted angle χ of the triple-point trajectory by Eq. (5) in Appendix D, using the five models of the equation of state for CO_2 with the measured angles χ^*, in terms of the deviation $\Delta\chi = \chi - \chi^*$. The centre line indicates $\Delta\chi = 0$, so that the closer the data points to the centre line, the better the agreement between theory and experiments. Our choice of perfect-gas model in Section 3 seems to be supported by Fig. D-1a, which shows the least overall deviations of the data points from the centre line among the five models. Deviations are seen to be greater for the models with more internal degrees of freedom.

Examination of experimental data by Gaydon & Hurle (21) reproduced in Table B1 shows that the dissociation relaxation time is an order of magnitude longer than the vibrational relaxation time, and that the measured peak temperatures closely agree with the theoretical temperatures calculated by Gaydon & Hurle. It seems therefore possible to preclude the equilibrium model from consideration for the range of shock Mach number of the present studies.

Figure B-2a shows the effect of increase of heat capacity due to excitation of three vibrational modes and dissociation. The latter phenomenon is clearly seen to be pressure-dependent. Since even a small degree of dissociation necessitates a large quantity of heat, temperature is considerably lower in dissociating gases than in a perfect gas. At $M_S = 12$, the equilibrium temperature - including dissociation - is less than half of the perfect-gas temperature. As a consequence of the lowering of temperature, density increases for real gases as evident in Fig. B-2b. Density is also influenced by the initial pressure if dissociation is taken into account. Even at $M_S = 12$, the equilibrium density with $P_0 = 1$ torr is more than twice as much as the limiting value of 7.9 for perfect CO_2 with $\gamma = 1.29$; and as M_S increases, density continues to increase in real gases. However, as far as pressure is concerned, behaviour of real gases does not deviate appreciably from that of a perfect gas as illustrated in Fig. B-2c. Figure B-2d shows the induced flow velocity behind the shock, nondimensionalized by the sound speed in the region in front of the shock. The behaviour of the curves may be understood in relation to Fig. B-2b: as density behind the shock is greater in real gases, the equation of continuity of mass implies that the flow velocity will accordingly be smaller in real gases. Figure B-3 shows the theoretical curves for the ratio of Kmole of dissociated CO_2 to Kmole of undissociated CO_2, or compressibility Z. It can be seen from Fig. B-3 that the effect of dissociation does not become significant until M_S exceeds 6.

Figure B-4 shows shock transit time, vibration and dissociation relaxation times in CO_2, which is reproduced from Fig. 5 of Camac (18). The vibration relaxation time of CO_2 at one atmosphere pressure is plotted in terms of particle time against temperature in Fig. B-5 by using the formula of Ref. 18 (see Section 6).
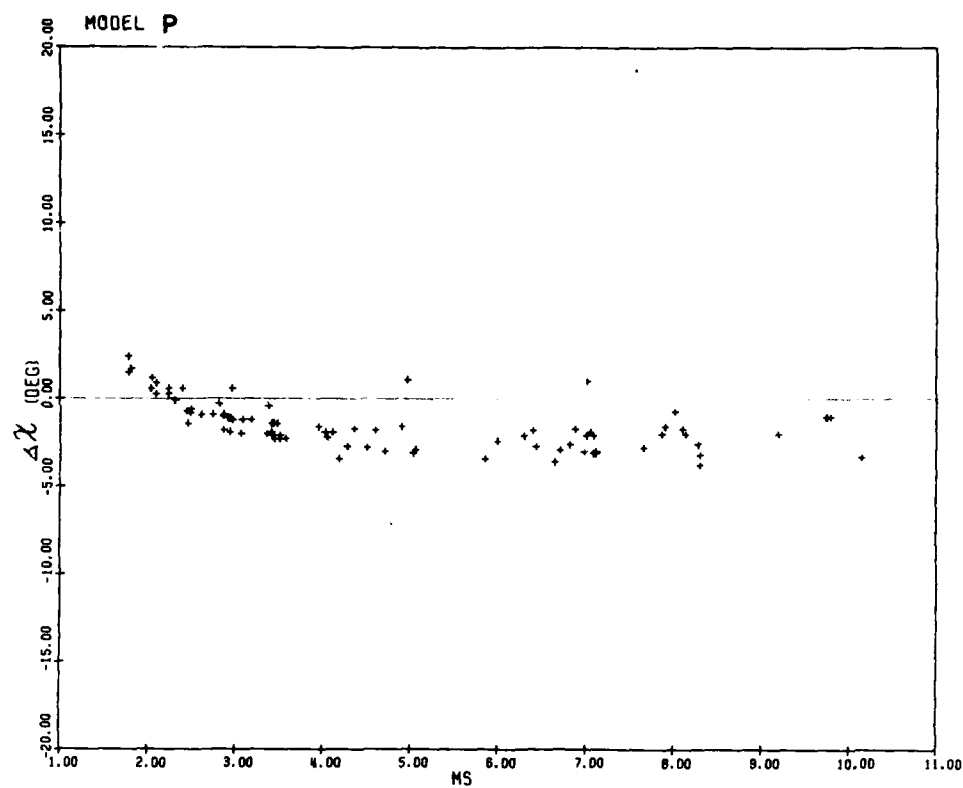
FIG. B1 COMPARISON OF THE PREDICTED χ AND MEASURED ANGLES χ^* OF THE TRIPLE-POINT TRAJECTORY.

(a) PERFECT CO_2 ($\gamma = 1.290$, MODEL P)
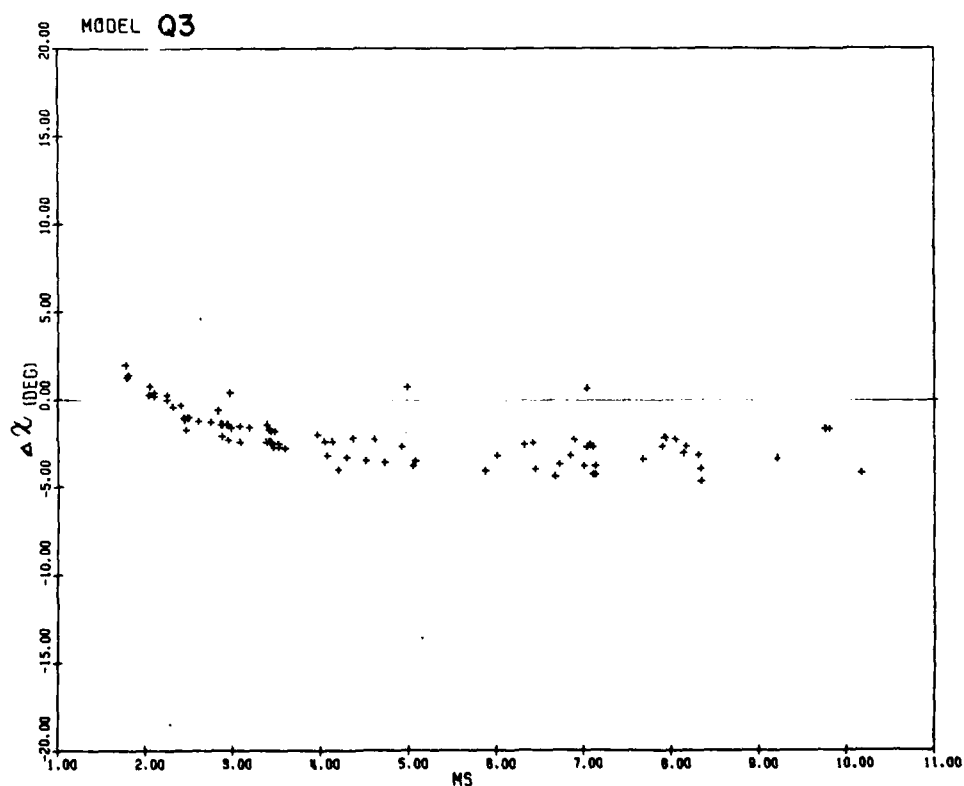
FIG. B1 - CONTINUED.   (b) QUASI-EQUILIBRIUM CO_2 (MODEL Q3)
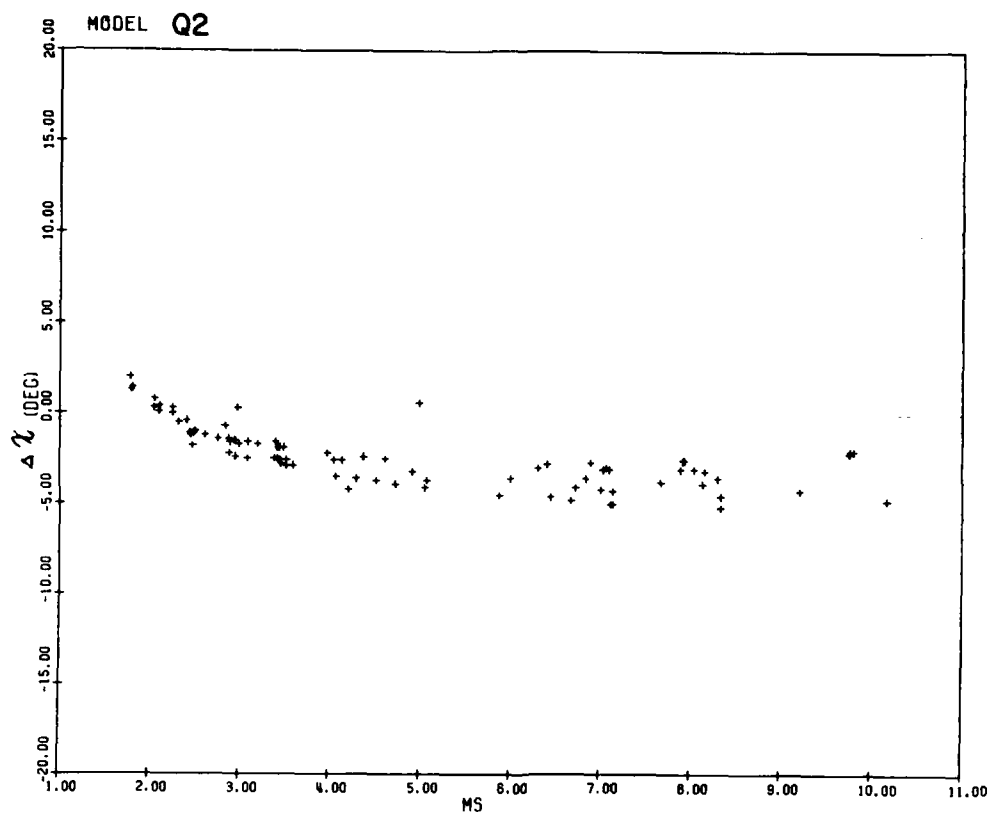
FIG. B1 – CONTINUED.   (c) QUASI-EQUILIBRIUM CO_2 (MODEL Q2)
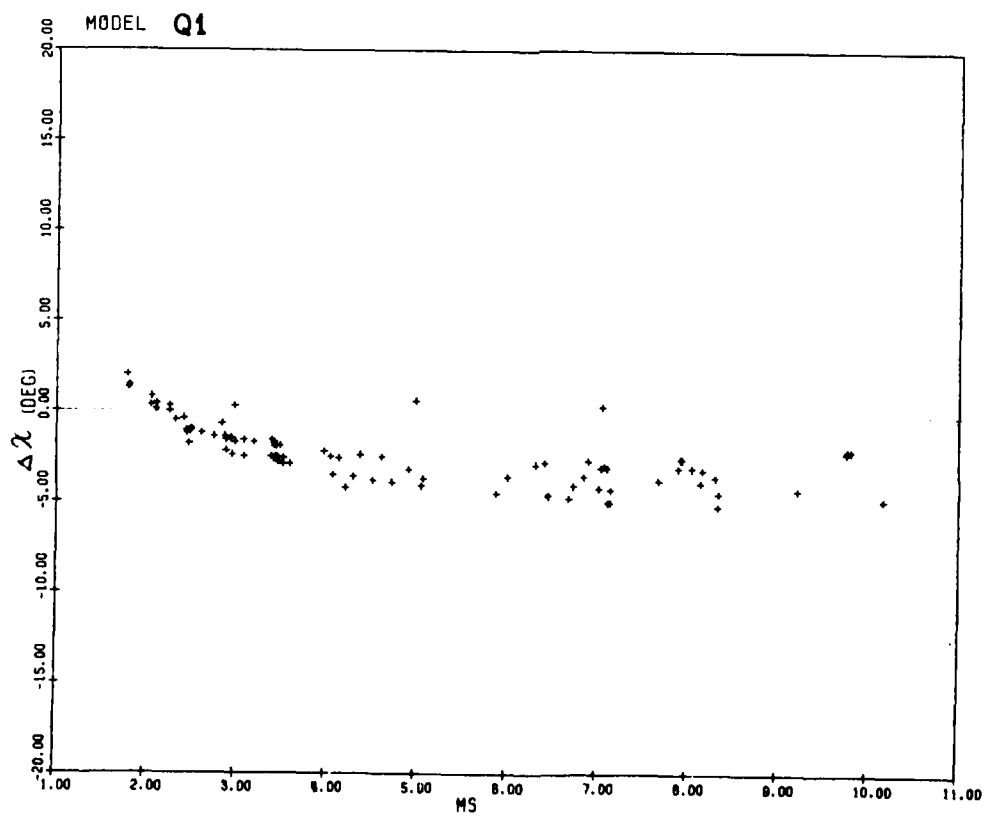
FIG. B1 – CONTINUED.   (d) QUASI-EQUILIBRIUM CO_2 (MODEL Q1)
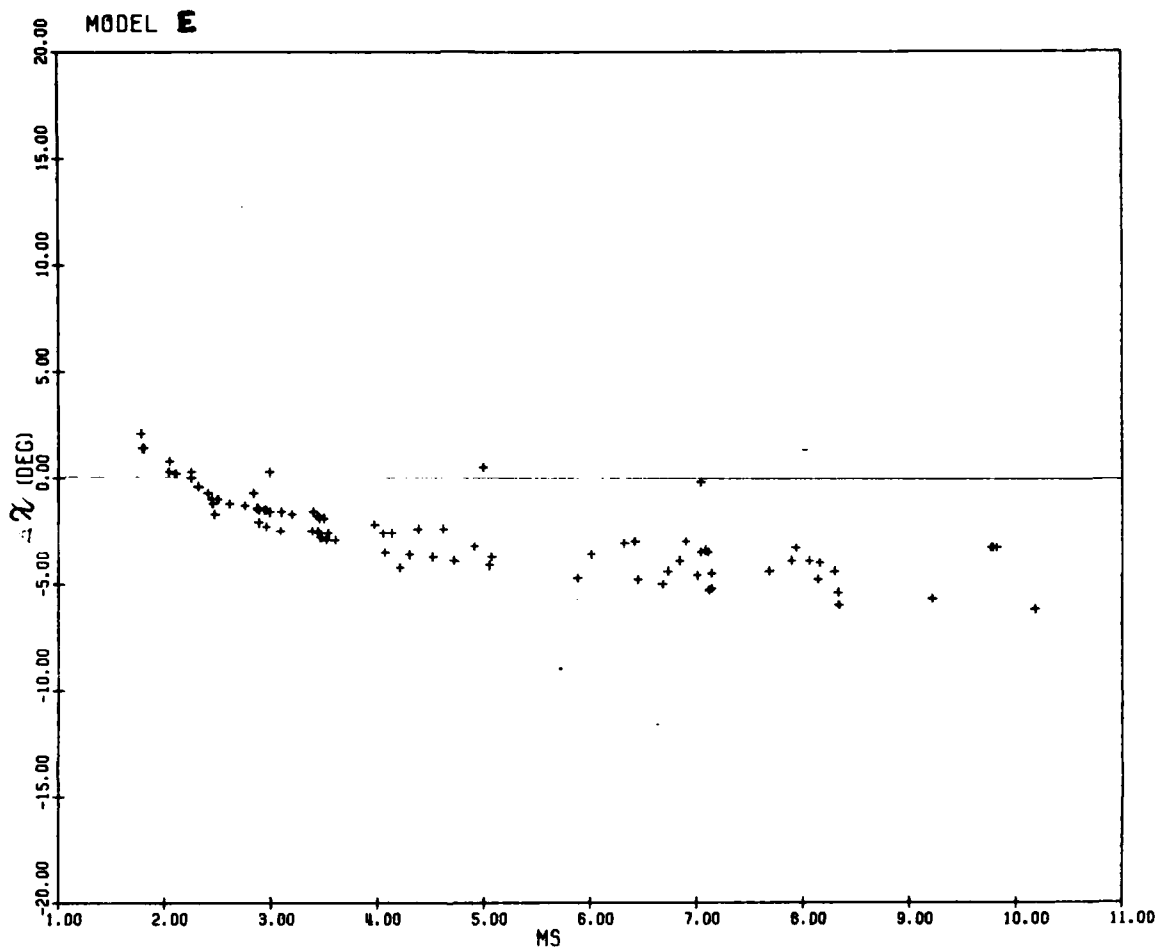
FIG. B1 - CONTINUED.

(e) EQUILIBRIUM CO_2 (MODEL E)
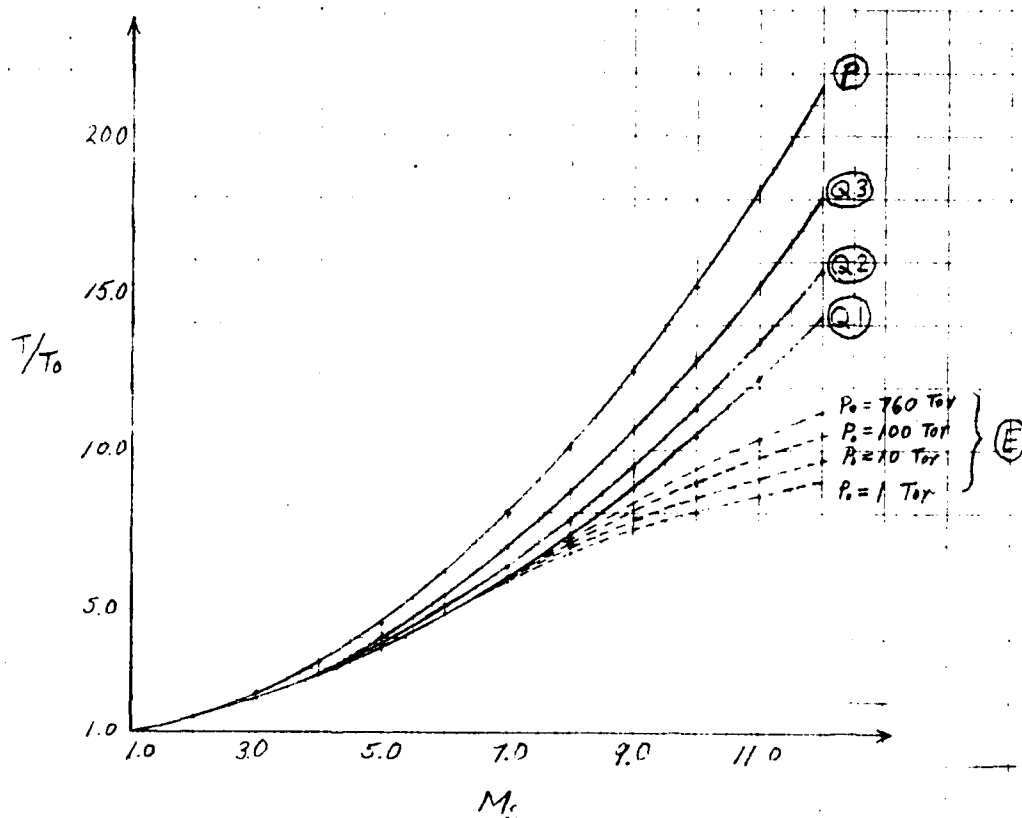
FIG. B2 VARIATION OF SHOCK PARAMETERS WITH SHOCK MACH NUMBER
IN PERFECT (γ = 1.29) AND REAL CO_2.   (a) TEMPERATURE
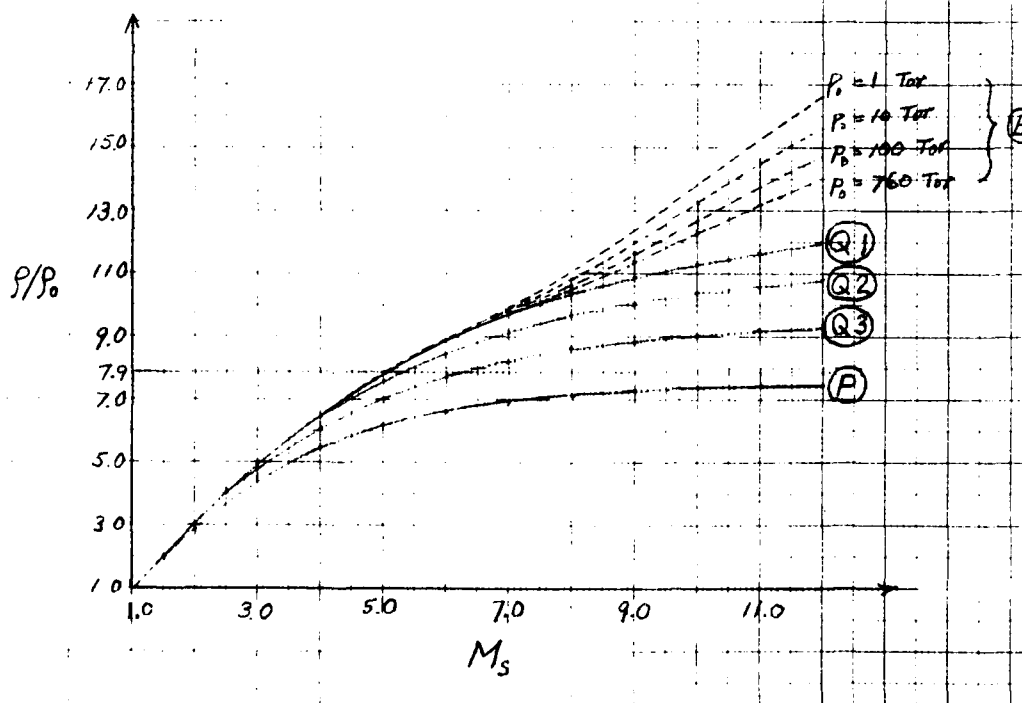
FIG. B2 - CONTINUED. (b) DENSITY

$P_o = 1$ tor
$P_o = 760$ Tor } Ⓔ

㉓
㉒
㉑
Ⓟ
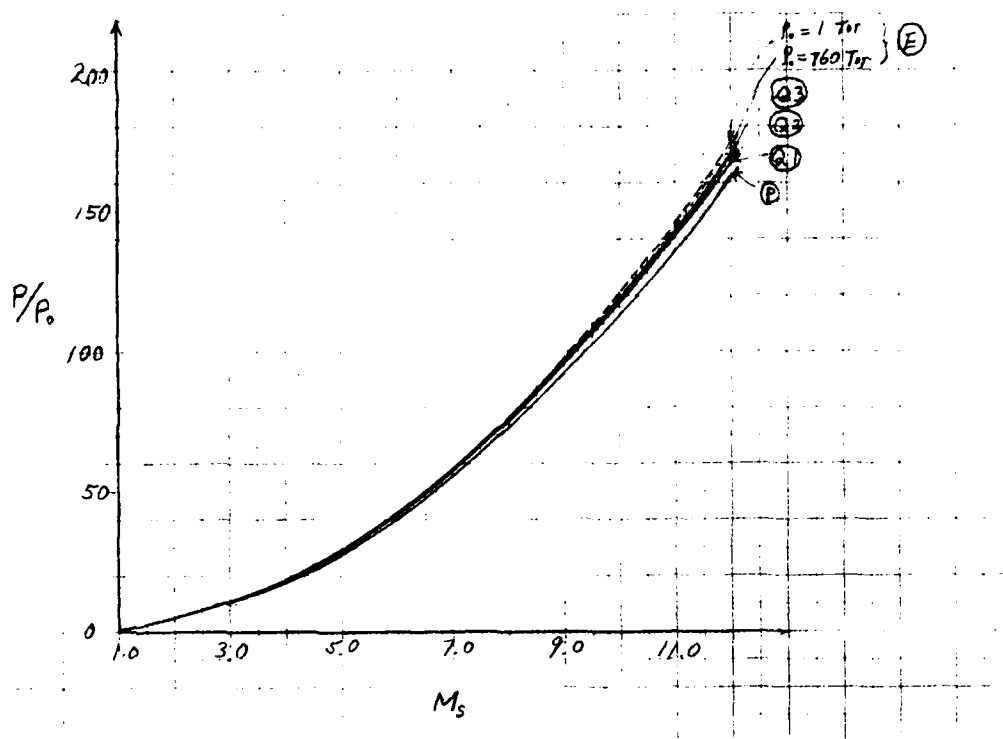
FIG. B2 – CONTINUED.   (c) PRESSURE

$P_o = 1$ tor
$P_o = 760$ tor } Ⓔ

㉑
㉒
㉓
Ⓟ
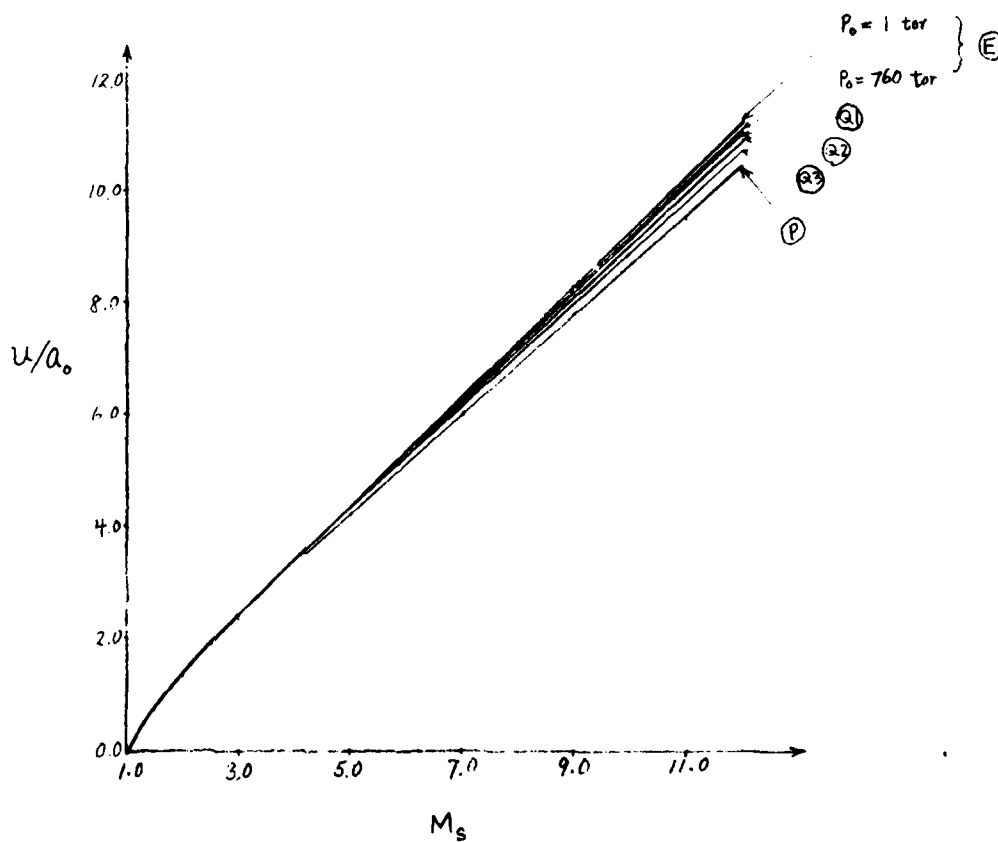
FIG. B2 – CONTINUED.

(d) RATIO OF INDUCED-FLOW VELOCITY u TO SPEED OF SOUND a_0
OF REGION AHEAD OF SHOCK
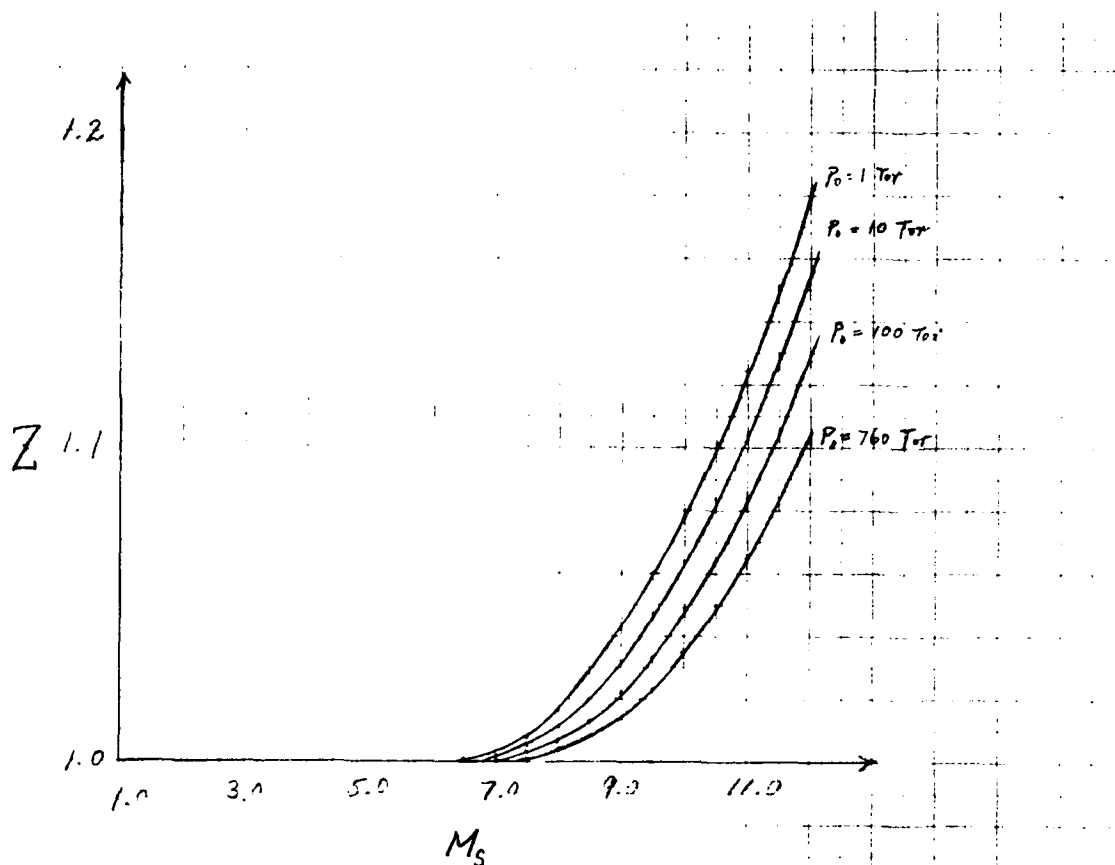
FIG. B3   KMOLE OF DISSOCIATED CARBON DIOXIDE PER KMOLE OF
          UNDISSOCIATED CARBON DIOXIDE (COMPRESSIBILITY, Z).
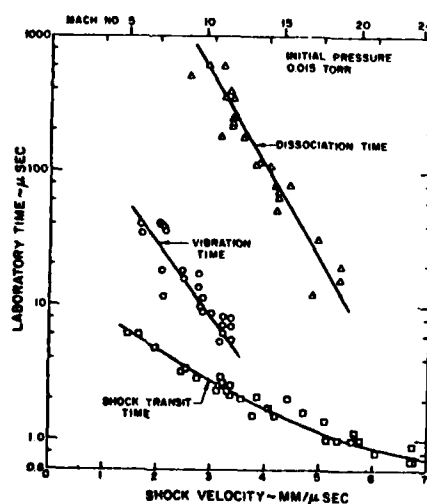
FIG. B4 CO_2 SHOCK TRANSIT TIME, VIBRATION AND DISSOCIATION
          RELAXATION TIMES [AFTER CAMAC (47)].
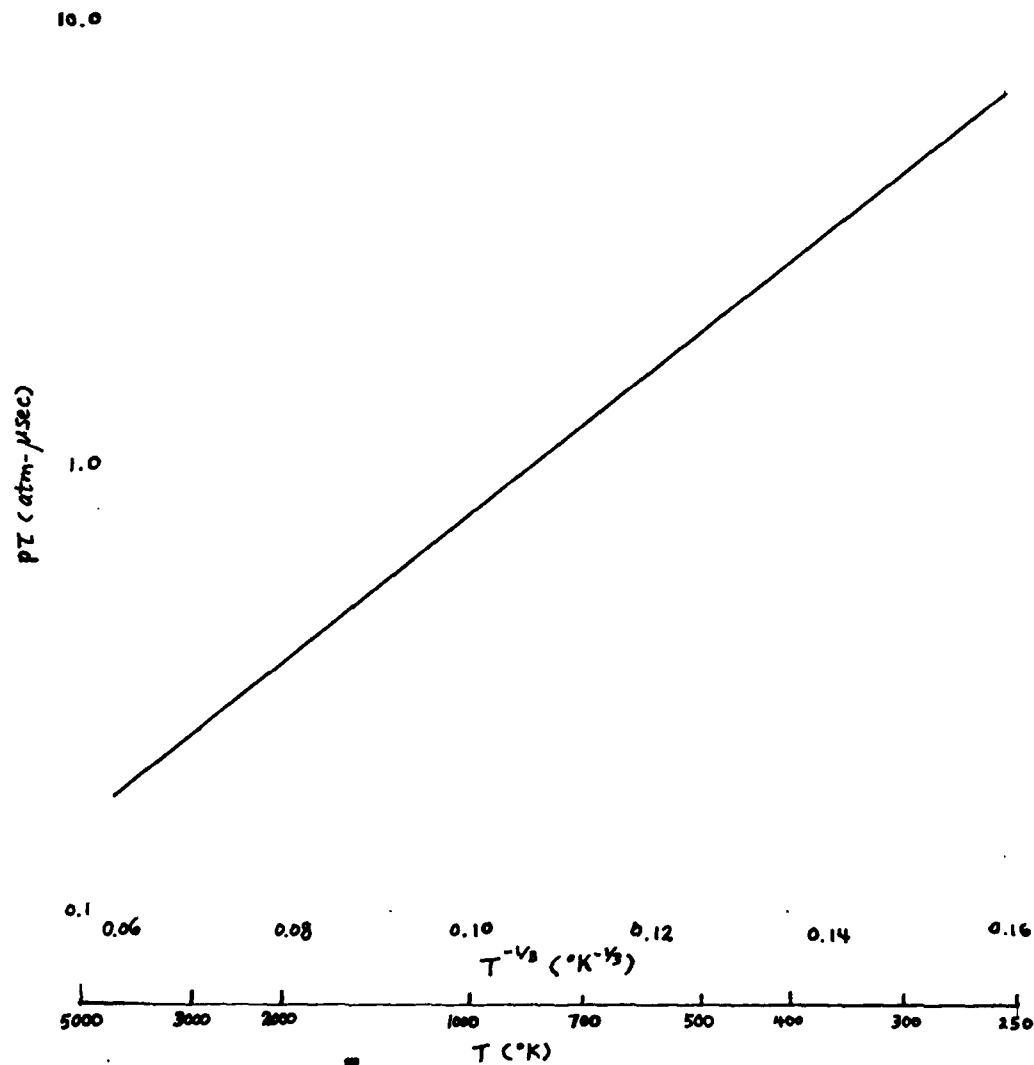
FIG. B5 CO$_2$ VIBRATION RELAXATION TIME. IN ATMOSPHERES
PRESSURE - MICROSECOND PARTICLE TIME IS PLOTTED
AS A FUNCTION OF T$^{-1/3}$ ($^{\circ}$K$^{-1/3}$) (AFTER REF. 47).

APPENDIX C

COMPARISON OF DENSITY CONTOURS

OBTAINED BY DIRECT AND INDIRECT METHODS

As mentioned in Section 2, infinite-fringe interferograms visualize the lines of constant density, or isopycnics, and are perhaps the simplest direct means to study the characteristics of density fields. When the flow field is not too complicated, it is even possible to determine the density of each isopycnic, for we know the density difference $\Delta\rho$ between any two consecutive isopycnics is related to the wavelength λ of the light source, and the so-called Gladstone-Dale constant usually denoted by K, which related the density change to the change in refractive index of the gas, by

$$\Delta\rho = \frac{\lambda}{KL}$$

where L is the depth of the test section of the shock tube. Using the values for K listed in Table C1, one can calculate $\Delta\rho$ for the case of N_2; it is equal to 0.2876×10^{-4} g/cm^3 for $\lambda = 6943$Å, and 0.1389×10^{-4} g/cm^3 for $\lambda = 3472$Å.

In view of these utilities of the infinite-fringe interferometry, it was felt desirable to repeat the experiments reported in Ben-Dor & Glass (5) taking the infinite-fringe interferograms to compare with the isopycnics of the flow fields they obtained by means of the fringe-shift analysis of finite-fringe interferograms. Because only two types of reflection - RR and SMR - are dealt with in Ref. 5, further two cases representative of CMR and DMR reported in Ref. 7a were also repeated, and similar comparisons were made. The results are presented in this appendix.

Figure C-1a is the infinite-fringe interferogram corresponding to Case 1 of Ref. 5. The density contours obtained from fringe-shift analysis by Ben-Dor and Glass is reproduced in Fig. C-1c. "Smearing" of isopycnic marked d in Fig. C-1a indicates the disturbance in the flow field due to the change of flow direction behind the curved reflected shock, i.e. the bow wave, from that along the shock-tube bottom surface to the direction along the wedge surface. The shapes of isopycnics are observed to be simple immediately behind the bow shock where the shock is almost normal to the induced flow, and behind the straight segment of the reflected shock. Figure C-2a is the infinite-fringe interferogram corresponding to Case 2 of Ref. 5. Figure C-2b is the result obtained by Ben-Dor and Glass from fringe-shift analysis and Fig. C-2c is the numerical prediction by Kutler & Shankar (41). The shape of isopycnic marked "a" in Fig. C-2a is noteworthy in that neither Figs. C-2b nor C-2c managed to depict. Although the resemblance of the shapes of the isopycnics between Figs. C-2a and C-2c is somewhat remote, the ranges of numerical values ρ/ρ_0 assigned to isopycnics in the two figures are in remarkably good agreement, while in Fig. C-2c the highest density region behind the straight reflected shock is approximately 15% greater than those values in Figs. C-2a and C-2c. Figure C-3a is the infinite-fringe interferogram for Case 3 in Ref. 5. The density contours obtained from fringe-shift analysis by Ben-Dor and Glass and from a numerical method by Schneyer (51) are reproduced in Figs. C-3b and C-3c, respectively.

A few words may be said about the number of isopycnics produced
in the density contours obtained from different methods. In the infinite-
fringe method, the difference in density $\Delta\rho$ between the two consecutive
fringes is $\Delta\rho = \lambda/(KL)$, so that $\Delta\rho$ can be made small - and hence more isopycnics
will be produced - by using the light sources of shorter wavelengths. Com-
pare Figs. C-1a and C-1b, which were taken simultaneously in the same experi-
ment. The wavelength of the light source for Fig. C-1a is one half of the
wavelength (the second harmonic) of the light source for Fig. C-1b. Hence,
other quantities such as density variation, K, and L being identical in both
pictures, there are twice as many isopynics visible in Fig. C-1a as in Fig.
C-1b. Before commenting on the number of isopycnics shown in the density
contours from the finite-fringe method, an outline of the method used by
Ben-Dor and Glass (5, 7a, b) is in order. Although the principle of their
modus operandi is no different from the standard finite-fringe method which
has long been used in the past, their innovation lies in Steps 2 and 3
described below, in which the digitizer was employed to record the fringe
numbers of the points along the fringes on the magnetic tapes, and the computer
was used to extrapolate the fringe numbers at points other than those measured
data points, the processes customarily required a great deal of tedious and
awkward labour.

1.   A point in the "no-flow" picture and the corresponding point in
the "flow" picture are chosen as origins, and the x- and y-axes are drawn,
with reference to which the coordinates of any point in the flow field may
be given.

2.   Each fringe is "digitized" by recording the x- and y-coordinates
of the points along the fringe on the magnetic tapes. Thus, discrete points
in the x-y planes in the "no-flow" and "flow" pictures are assigned particular
fringe numbers.

3.   At equidistant points along lines of constant x (or y) in the x-y
plane drawn in the flow field, fringe numbers S_1 in the "no-flow" picture,
and S_2 in the "flow" picture are determined by means of extrapolation from
the nearest measured points. The fringe-shift values S at those points are
then obtained by

$$S = S_2 - S_1$$

from which densities ρ are found by

$$\rho = \rho_0 + \frac{\lambda}{KL} S$$

where $_0$ is the initial density.

4.   Isopycnics are drawn by connecting (by hand) the points of equal
density.

Thus, it can be seen that evaluated densities consist entirely of extrapolated values. Since the flow field is considered two-dimensional in the analysis, extrapolation is troublesome under the best of circumstances; and the fact of the matter is when the flow field is complex, the results tend to be no more reliable than sheer guesses. The reliability of the outcome from the finite-fringe method, therefore, does not depend so much on how numerous the isopycnics are drawn as on how closely the fringes are placed in the original interferograms. Moreover, owing to the expected error in measuring fringe shift (usually considered to be 0.1 fringes), there is a limit to how minutely the density change measurement can be achieved [see, for example, Ben-Dor & Whitten (10)]; therefore, the density variation between two consecutive isopycnics from the finite-fringe method should not be less than the limit thus imposed, regardless of the fringe-spacing in the original interferograms.

Infinite-fringe interferograms for CMR and DMR, and corresponding results from fringe-shift analysis by Ben-Dor and Glass (7a) are shown in Figs. C-4 and C-5. In either case, the range of values for ρ/ρ_0 given in Ref. 7a is nearly 15% larger than those determined from the infinite-fringe interferograms of the present experiments. The shapes of the isopycnics obtained using the infinite-fringe method also differ somewhat from the the finite-fringe results.

The method used by Ben-Dor and Glass (5, 7a, b) enables the densities to be determined at discrete points, so that the manner of connecting points at which the densities are identical to a prescribed tolerance tends inevitably to be speculative, particularly when the number of points in the flow field at which density is evaluated is small. In order to minimize the inherent error in judgement and to maximize the accuracy of the end result, it seems essential to make fringe-spacing of finite-fringe interferograms as narrow as possible, and to take as many points on fringes as practicable when digitizing the interferograms. The reason is to keep the interpolation errors small, since the points at which densities are to be determined do not necessarily coincide with those points at which the fringe shifts are measured, i.e., the points on fringes, cumbersome interpolation process becomes necessary to calculate the fringe shifts at points which do not lie on any fringe.

Despite its shortcomings, the approach taken by Ben-Dor and Glass (5, 7a, b) must be commended for being the first to attempt to put the digital computer to good use in order to save a considerable amount of tedious manual labour required in the process of drawing isopycnics by the finite-fringe method. It may be regarded as a springboard for more sophisticated ones which will undoubtedly be developed in the near future.
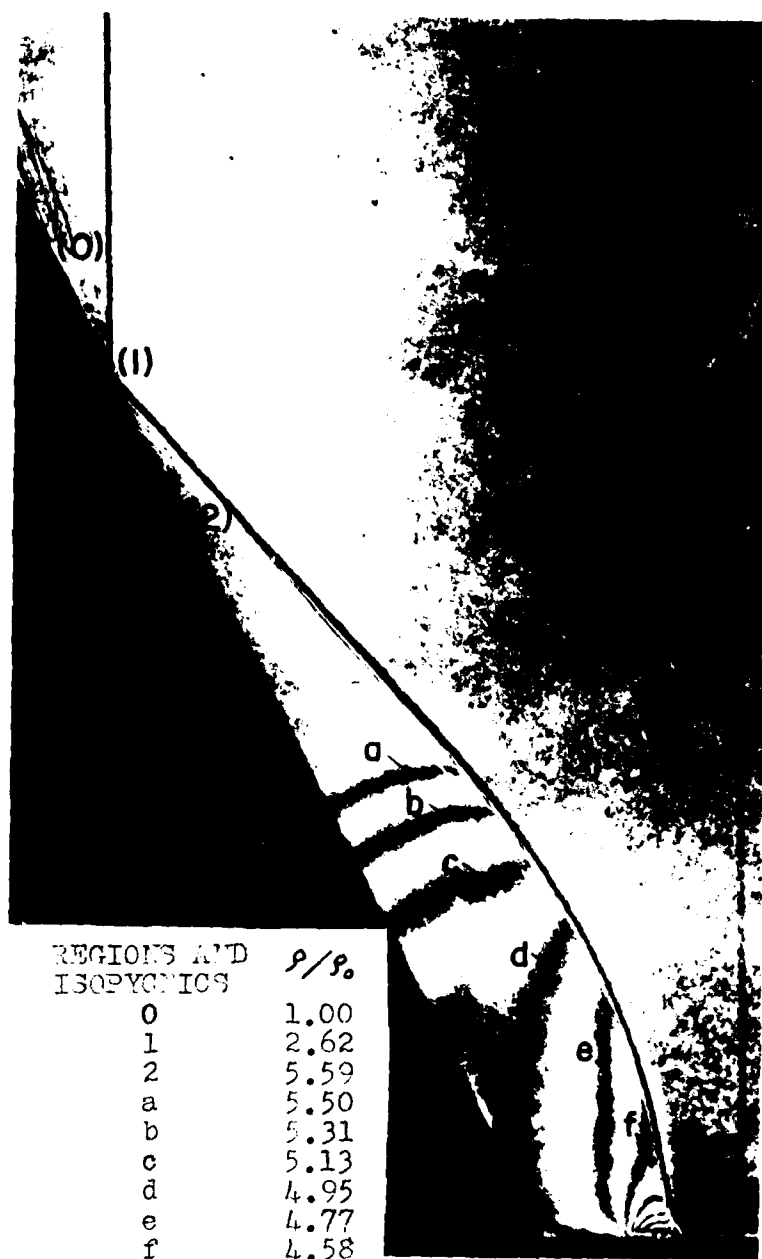
FIG. C1 DENSITY CONTOURS OF REGULAR REFLECTION IN N_2.

(a) INFINITE-FRINGE INTERFEROGRAM ($\lambda = 3472\text{Å}$)

$M_s = 1.97$, $\theta_w = 63.4°$, $P_0 = 50$ torr, $T_0 = 298.2°K$,
$\rho_0 = 0.7582 \times 10^{-4}$ g/cm³

FIG. C1 DENSITY CONTOURS OF REGULAR REFLECTION IN N_2.

(b) INFINITE-FRINGE INTERFEROGRAM ($\lambda = 6943Å$)

[TAKEN SIMULTANEOUSLY WITH THE INTERFEROGRAM IN FIG. C1(a)
IN THE SAME EXPERIMENT; FOR INITIAL CONDITIONS SEE FIG. C1(a).]

n	ρ / ρ_0
1	1.00
2	2.68
3	5.84
4	3.77
5	3.72
6	3.67
7	3.62
8	3.57
9	3.52
10	3.47
11	3.42
12	3.37
13	3.32
14	3.27
15	3.22
16	3.17
17	3.12
18	3.07
19	3.02
20	2.97

$\dfrac{\Delta \rho}{\rho_0} = 0.039$

$\overline{PQ} = 40.6$ mm

$\rho_0 = 0.757 \times 10^{-4} \ \dfrac{gm}{cm^3}$
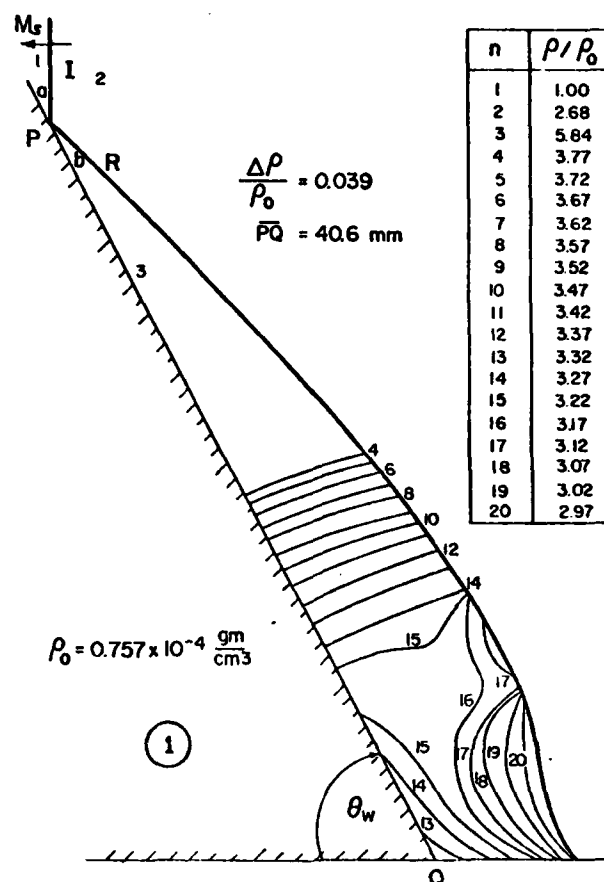
FIG. C1 - CONTINUED.

(c) ISOPYCNICS OBTAINED FROM FRINGE-SHIFT ANALYSIS OF FINITE-FRINGE INTERFEROGRAMS [AFTER BEN-DOR & GLASS (5)]. $M_s = 2.01$, $\theta_w = 63.4°$, $P_0 = 50$ torr, $T_0 = 298.6°K$.

REGIONS AND ISOPYCNICS	ρ/ρ_0
0	1.00
1	4.88
2	14.6
a	14.3
b	13.7
c	13.1
d	12.4
e	11.8
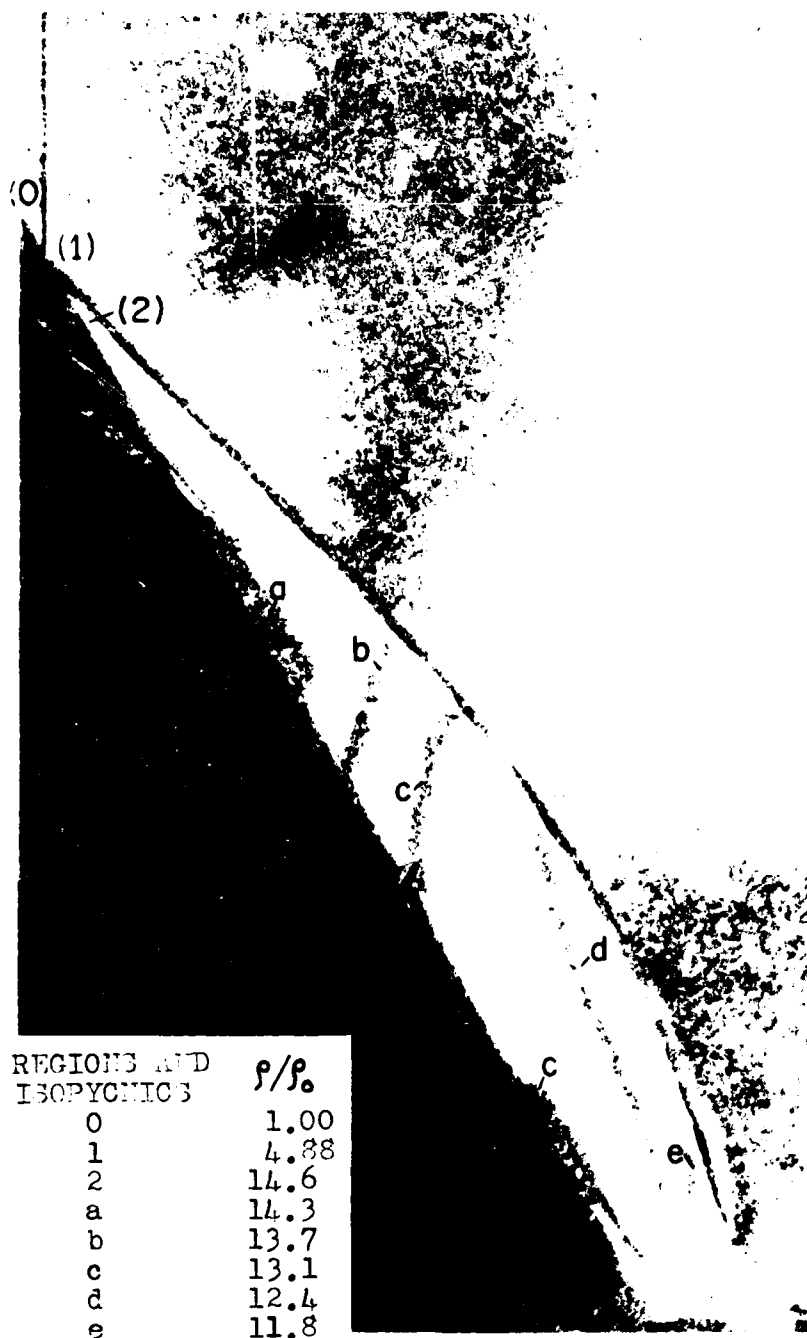
FIG. C2 DENSITY CONTOURS OF REGULAR REFLECTION IN N_2.

(a) INFINITE-FRINGE INTERFEROGRAM ($\lambda = 3472\text{Å}$)

$M_s = 4.66$, $\theta_w = 63.4°$, $P_0 = 15$ torr, $T_0 = 298.3°$K, $\rho_0 = 0.2257 \times 10^{-4}$ g/cm^3

Figure (b):

n	ρ/ρ_0
1	1.00
2	5.32
3	12.57
4	13.00
5	13.43
6	13.86
7	14.30
8	14.73
9	15.16
10	15.60
11	16.77

$$\frac{\Delta\rho}{\rho_0} = 0.126$$

$$\overline{PQ} = 43.9 \text{ mm}$$

$$\rho_0 = 0.231 \times 10^{-4} \frac{gm}{cm^3}$$

(b)

Figure (c):

n	ρ/ρ_0
1	14.41
2	14.14
3	13.77
4	13.54
5	13.24
6	12.98
7	12.70
8	13.35
9	13.47
10	13.08
11	12.75

(c)
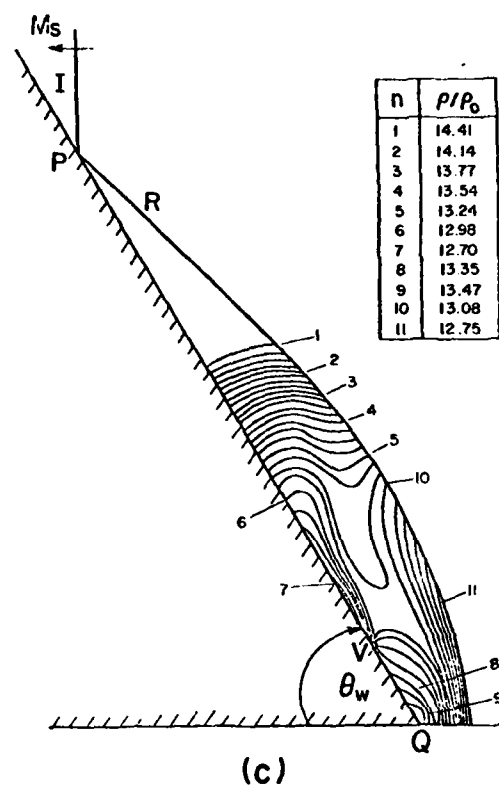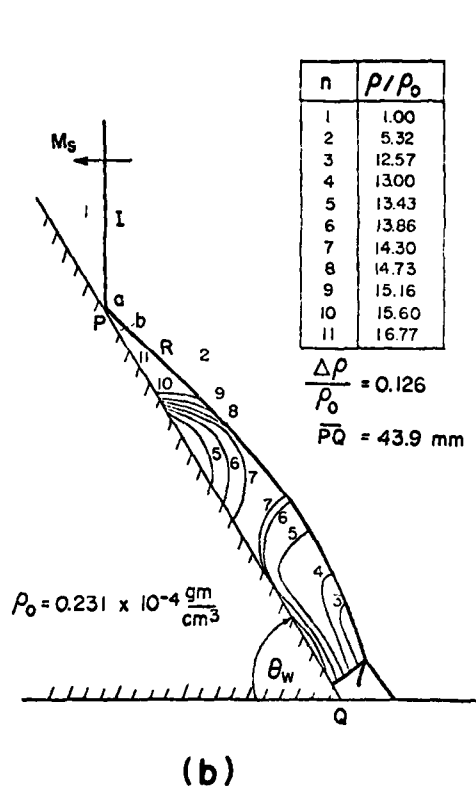
FIG. C2 - CONTINUED.

(b) ISOPYCNICS OBTAINED FROM FRINGE-SHIFT ANALYSIS OF FINITE-FRINGE INTERFEROGRAMS (λ = 3472Å) [AFTER BEN-DOR & GLASS (61)]. M_S = 4.68, θ_w = 60°, P_0 = 15.31 torr, T_0 = 298.1°K.

(c) ISOPYCNICS FOR REGULAR REFLECTION, NUMERICAL PREDICTION [AFTER KUTLER & SHANKAR (62)], O_2, γ = 1.4, M_S = 4.71, θ_w = 60°.

n	ρ/ρ_0
1	1.00
2	2.68
3	3.27
4	3.32
5	3.37
6	3.42
7	3.47
8	3.52
9	3.57
10	3.62
11	3.67
12	3.72
13	3.77
14	3.82
15	3.87
16	3.92

$$\frac{\Delta\rho}{\rho_0} = 0.039$$

$$\overline{PQ} = 41.9 \text{ mm}$$

$$\rho_3 = 0.757 \times 10^{-4} \frac{gm}{cm^3}$$

(b)

Contour Levels
1.5
2.0
2.6
3.0
3.3
3.6
3.75

(c)
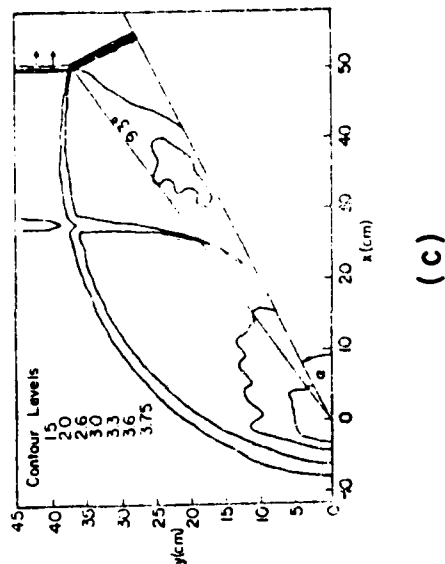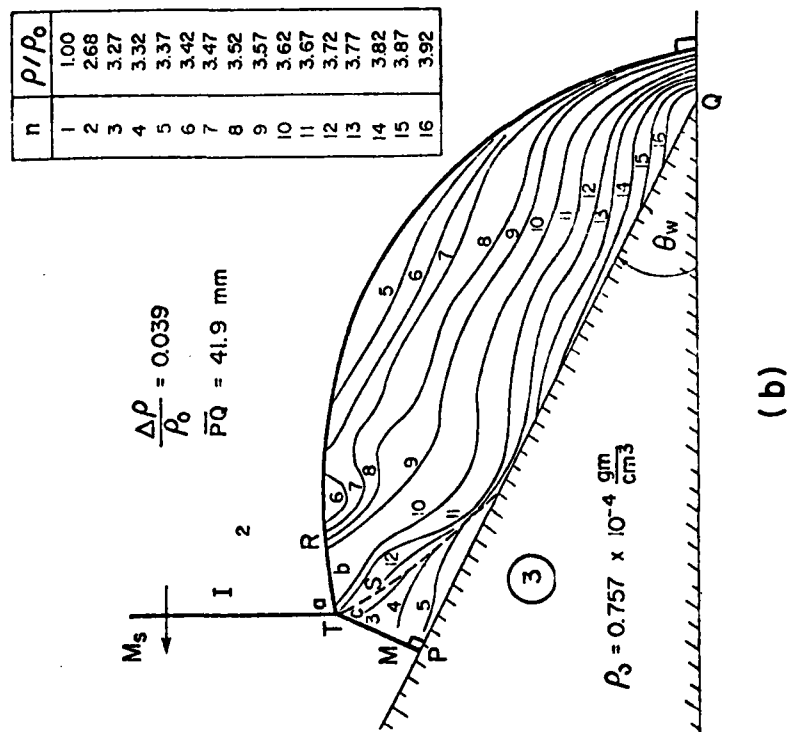
FIG. C3 - CONTINUED.

(b) ISOPYCNICS OBTAINED FROM FRINGE-SHIFT ANALYSIS OF FINITE-
FRINGE INTERFEROGRAMS [AFTER BEN-DOR & GLASS (61)].
N_2, $M_S = 2.01$, $\theta_w = 26.56°$, $P_0 = 50$ torr, $T_0 = 296.6°K$.

(c) ISOPYCNICS FOR SINGLE MACH REFLECTION, NUMERICAL PREDICTION
[AFTER SCHNEYER (64)]. $\gamma = 1.4$, $M_S = 2$, $\theta_w = 26.56°$.
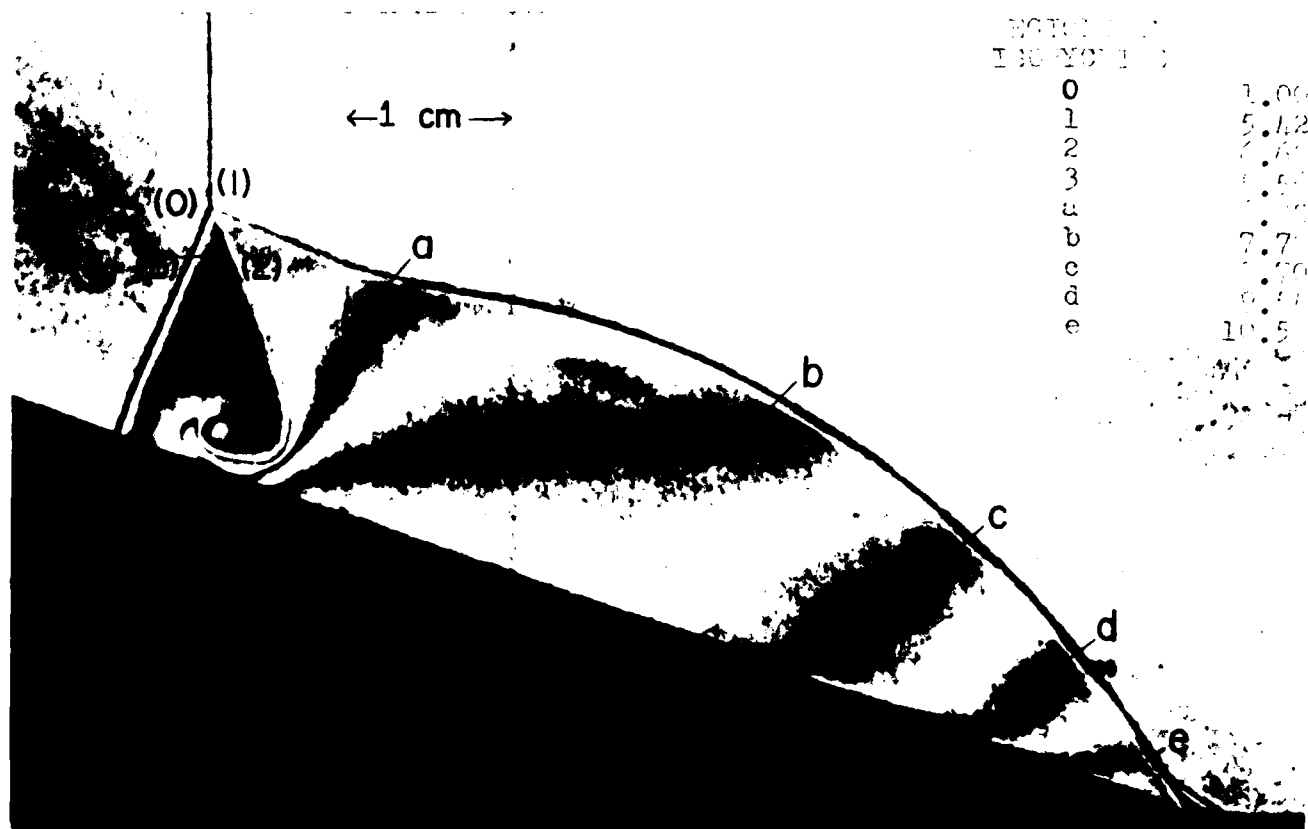
VELOCITY FIELD OF A CONEFLEX MACH REFLECTION IN AIR.

(a) EXPANDED SCHLIEREN TRIAL PHOTOGRAM ($\lambda = $ ...).
... P = ... torr, ...

n	ρ/ρ_0
1	1.000
2	6.227
3	6.672
4	7.197
5	6.502
6	6.827
7	7.152
8	7.477
9	7.802
10	8.127
11	8.453
12	8.778
13	9.103
14	9.428
15	9.753
16	10.078
17	10.403
18	10.728
19	11.053
20	11.378
21	11.704
22	12.029
23	12.354

$$\frac{\Delta\rho}{\rho_0} = 0.188$$

$$\overline{PQ} = 57.0 \text{ mm}$$

$$\rho_0 = 0.154 \times 10^{-4} \frac{gm}{cm^3}$$
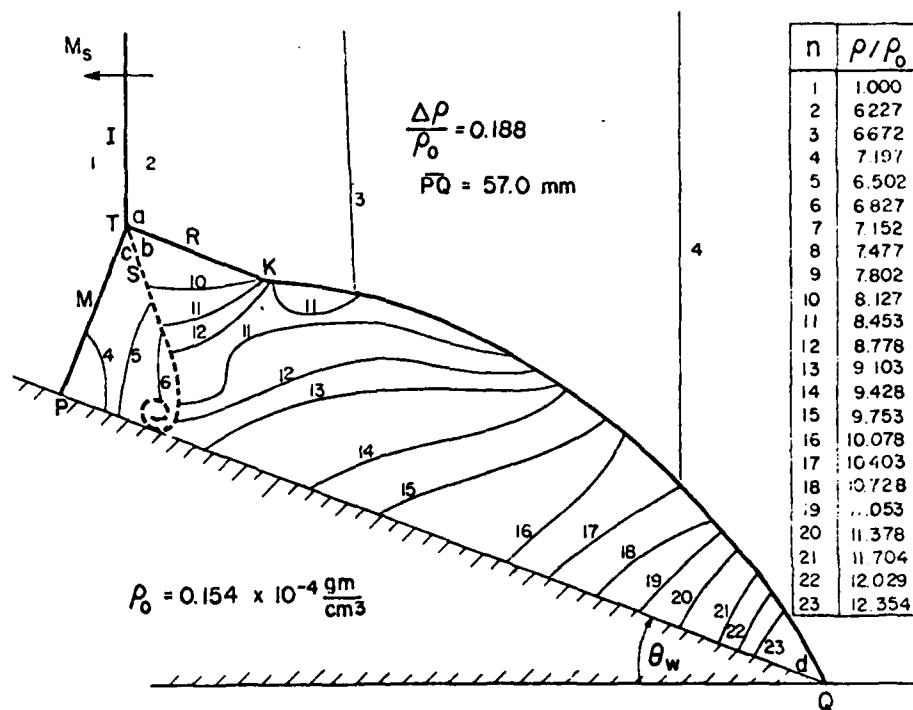
FIG. C4 - CONTINUED.

(b) ISOPYCNICS OBTAINED FROM FRINGE-SHIFT ANALYSIS OF FINITE-FRINGE INTERFEROGRAMS [AFTER BEN-DOR & GLASS (23a)]. N_2, $M_s = 6.90$, $\theta_w = 20°$, $P_0 = 10.12$ torr, $T_0 = 295.8°K$.

SECTION(?) ... ... E MACH REFLECTION IN K...

(a) ... ... INTERFEROGRAM (λ = 3.7...Å)
... ... T_0 = ... °K.

The figure shows a schematic with shock wave labels. Table of values:

n	ρ/ρ_0
1	1.000
2	5.680
3	6.685
4	6.830
5	7.806
6	8.872
7	9.756
8	10.734
9	11.710
10	12.685
11	13.661
12	14.637
13	15.613
14	16.589
15	17.564

$$\frac{\Delta\rho}{\rho_0} = 0.376$$

$$\overline{PQ} \approx 69.4 \text{ mm}$$

$$\rho_0 = 0.769 \times 10^{-5} \frac{gm}{cm3}$$
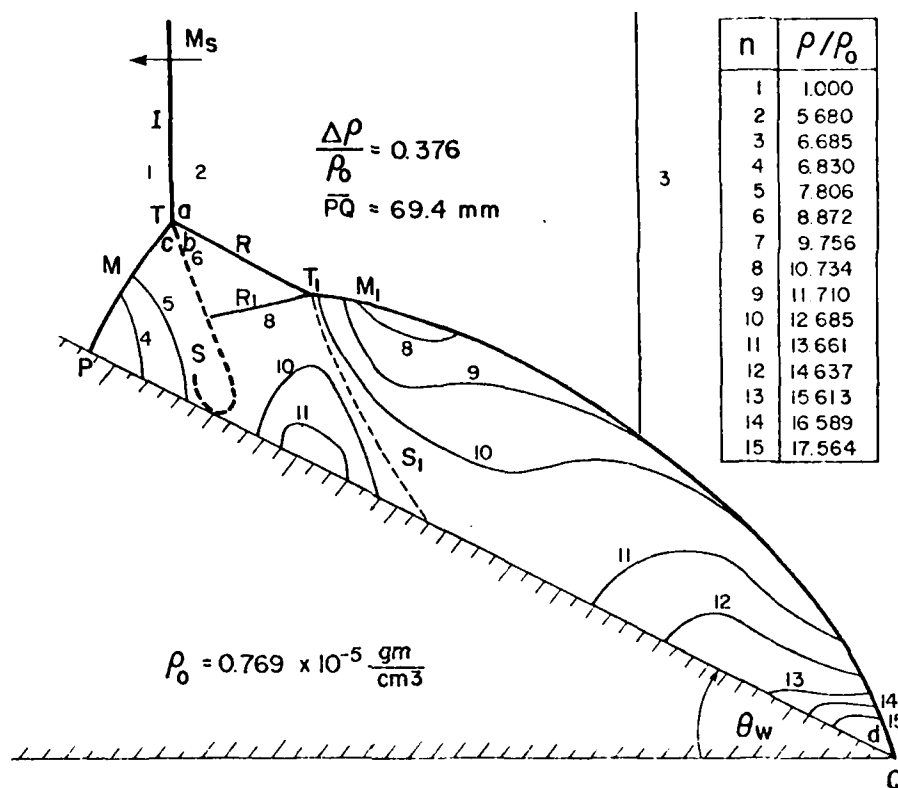
FIG. C5 - CONTINUED.

(b) ISOPYCNICS OBTAINED FROM FRINGE-SHIFT ANALYSIS OF FINITE-FRINGE INTERFEROGRAMS [AFTER BEN-DOR & GLASS (23a)]. N_2, $M_S = 8.06$, $\theta_W = 26.56°$, $P_0 = 5.11$ torr, $T_0 = 298.2°K$.

DERIVATION OF THE EXPRESSION FOR THE MACH NUMBER OF THE FLOW

BEHIND THE REFLECTED SHOCK RELATIVE TO THE REFLECTING SURFACE,

AND COMPARISON WITH EXPERIMENTS

Referring to Fig. 21a, the velocity u_2' of the flow in region 2 relative to E, where E is the intersection point of the extension of the straight segment of the slipstream S with the wedge surface, can be determined as follows: First, obtain the three-shock solution at the primary triple point T so that all the flow properties of the surrounding regions are known. Then, with the angle ψ as defined in Fig. 21a, the velocity w of T relative to E is found by applying the sine law to triangle OTE whose sides are proportional to the velocities of its vertices relative to each other, and is given by

$$w = u_0 \sin\chi / \sin\psi \tag{1}$$

where

$$\psi = \pi - (\chi + \theta_5) \tag{2}$$

Now, u_2 and w are in the same direction, so that u_2' is found by a straightforward application of a Galilean transformation

$$u_2' = u_2 - w \tag{3}$$

Thus, the Mach number M_2' of the flow in region 2, relative to E is given by

$$
\begin{aligned}
M_2' &= u_2'/a_2 \\
&= u_2/a_2 - (u_0/a_0)(a_0/a_2)(\sin\chi/\sin\psi) \\
&= M_2 - M_0(a_0/a_2)(\sin\chi/\sin\psi)
\end{aligned}
\tag{4}
$$

where a_i is the speed of sound in region i, which agrees with the expression given by Gvozdeva & Fokeev (18).

Equation (1) involves one parameter that is extraneous to the three-shock solution, i.e. the trajectory angle χ of the triple point T. As the three-shock solution pertains strictly to the local problem around T, one further assumption is required to relate the shock angles at T to the "global" boundary, i.e. in this case, the wedge surface. The most obvious assumption, and the one we shall adopt here, is that the extension of the tangent to the Mach stem at T meets the wedge surface perpendicularly. The required trajectory angle χ is then simply given by

$$\chi = \pi/2 - \phi_3 \qquad (5)$$

where ϕ_3 is the flow angle incident on the Mach stem and is given in the three-shock solution. Under this assumption the wedge angle θ_w is related to the three-shock resolution by

$$\theta_w = \phi_3 - \phi_0 \qquad (6)$$

where ϕ_0 is the angle between the oncoming flow u_0 and the incident shock I, and is a known quantity from experiment through the relation

$$\phi_0 = \pi/2 - (\theta_w^* + \chi^*) \qquad (7)$$

Note that the unprimed quantities χ and θ_w in Eqs. (5) and (6) indicate the predicted values, while the primed ones χ^* and θ_w^* in Eq. (7) indicate the measured values. Thus, by combining the above three equations (5), (6) and (7), it is possible to see how the two quantities $\Delta\chi$ and $\Delta\theta_w$ are related, where $\Delta\chi = \chi - \chi^*$ and $\Delta\theta_w = \theta_w - \theta_w^*$, as follows: From Eq. (5),

$$\phi_3 = \pi/2 - \chi \qquad (5')$$

Substitution of Eqs. (5') and (7) into Eq. (6) yields

$$\theta_w = \pi/2 - \chi - \pi/2 - \theta_w^* - \chi^* \qquad (8)$$

This becomes, after rearranging,

$$\theta_w - \theta_w^* = -(\chi - \chi^*) \qquad (9)$$

or

$$\Delta\theta_w = -\Delta\chi$$

The transition boundary between CMR and DMR in Fig. D1 is drawn according to Eq. (4) above, and all other boundaries are the same as in Fig. 39. Inadequacy of the transition criterion from CMR to DMR is apparent, confirming the remarks made by Bazhenova et al (4) and Gvozdeva & Fokeev (27) that the criterion of $M_2 = 1$ relative to E cannot be used to give the transition boundary between CMR and DMR.
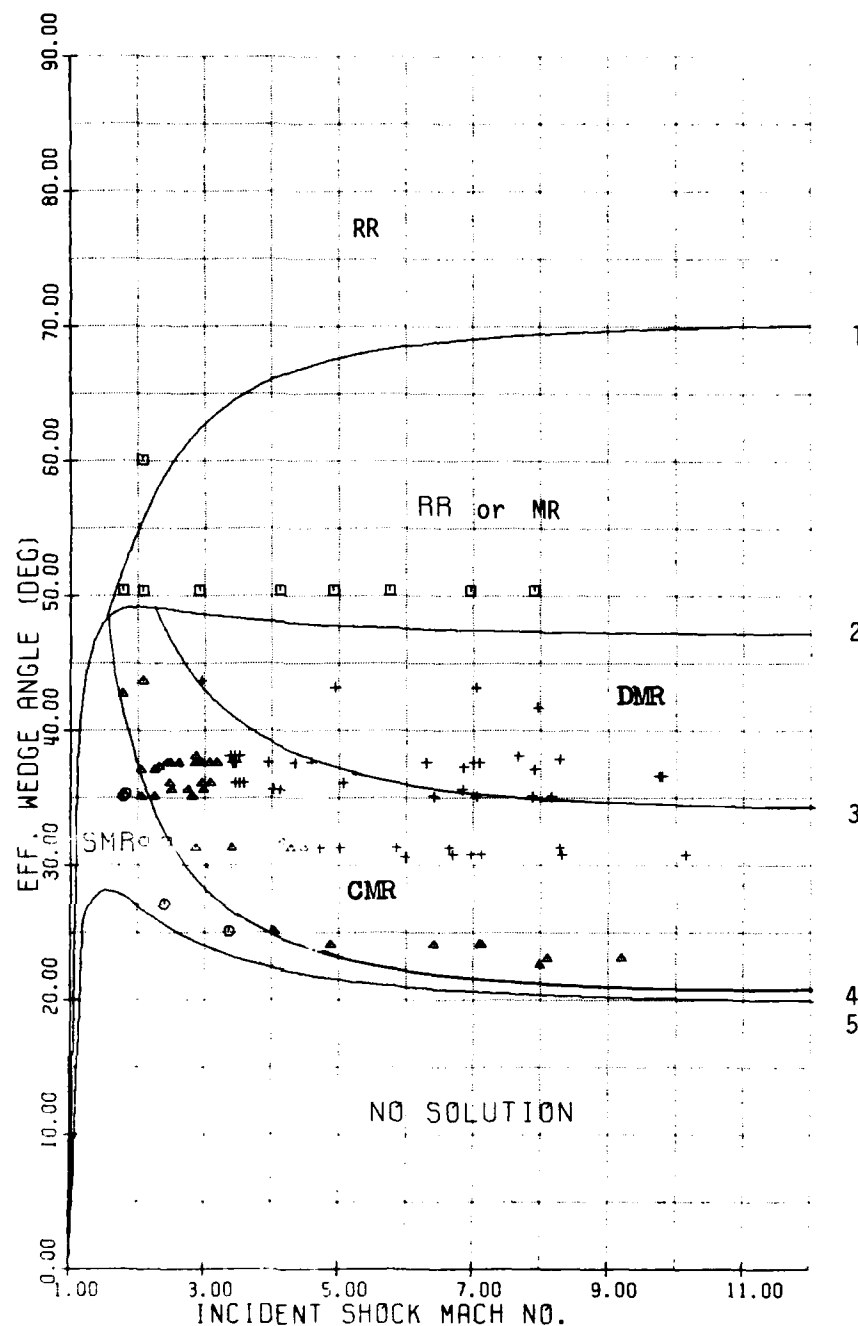
FIG. D1   COMPARISON OF PREDICTED REGIONS OF VARIOUS TYPES OF REFLECTION
AND EXPERIMENT [PERFECT CO_2 (γ = 1.29)].

TRANSITION BOUNDARIES:

(1) THE VON NEUMANN CRITERION
(2) THE DETACHMENT CRITERION
(3) FLOW BEHIND THE REFLECTED SHOCK IS SONIC
    RELATIVE TO THE WEDGE SURFACE
(4) FLOW BEHIND THE REFLECTED SHOCK IS SONIC
    RELATIVE TO THE PRIMARY TRIPLE POINT (M_2 = 1)
(5) THE EXTREME SONIC ANGLE (M_1 = 1)

TYPES OF REFLECTION: $\square$ = RR; $\circ$ = SMR; $\triangle$ = CMR; + = DMR.

APPENDIX E

INFLUENCES OF INITIAL PRESSURES ON THE IMAGES OF ISOPYCNICS

IN INFINITE-FRINGE INTERFEROGRAMS

As mentioned in Appendix C, the density difference $\Delta\rho$ between two consecutive isopycnics in the infinite-fringe interferogram is fixed for given wavelength λ of the light source, Gladstone-Dale constant K of the gas, and depth L of the shock-tube test section. The density variation in the flow field is enhanced by the higher initial pressure, since it will take a shorter distance for density to change by $\Delta\rho$ in a gas of higher P_0 than of lower P_0. Thus, by increasing P_0, more numerous isopycnics will be produced in the infinite-fringe interferograms for otherwise identical experiments. It can be seen in Figs. E1 and E2, which show RR and CMR with varied P_0, that every thick, smeared isopycnic in the interferograms with lower P_0 is replaced by two or more isopycnics that are narrower and distinct in the interferograms with higher P_0.

The vibrational relaxation lengths ℓ_v, the distance required for the departure from equilibrium to fall to 1/e, are calculated by using Camac's empirical formula cited in Section 6 (p. 16), and shown in the figures.

The conclusion based on the infinite-fringe interferograms in this appendix is that it is advantageous to use higher P_0 when investigating the characteristics of the density field, for then one can obtain a clearer perspective of the field.

Another crucial point shown by these interferograms is that although the vibrational relaxation lengths vary by an order of magnitude, the wave angles and slipstream angles do not change for a given M_s and θ_w. This confirms that the transition lines shown in Fig. 38a are correct only for $\gamma = 1.290$.

The author thanks Dr. J. H. Lee and Mr. R. Deschambault for making available the infinite-fringe interferograms included in this appendix.

(a)

(b)

|1.0 cm|

FIG. E1 - CONTINUED.

(c) $M_s = 2.4$, $\theta_w = 63.4°$, $P_0 = 10$ torr, $T_0 = 298.8°K$, $\ell_v = 10.2$ mm.

(a)
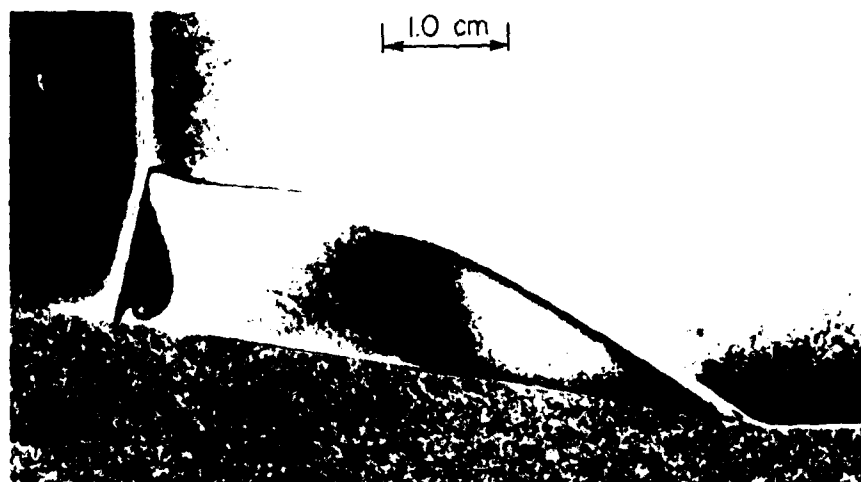
(b)

FIG. ... . INTERFEROMETRIC IMAGES OF ISOPYCNICS IN
... ... SINGLE HEAD AND SINGLE MACH REFLECTION IN CO_2
(... ... ...).

... ... tom, P_0 = ... K, d_g = ... mm

... ... tom, P_0 = ... K, d_g = ... mm

APPENDIX F

COMPARISON OF THE PREDICTED AND MEASURED ANGLES OF REFLECTION

The angle ω between the trajectory of the triple point and the reflected shock, or the angle of reflection, for each experiment in the present study was measured by using a conventional protractor. The difference $\Delta\omega$ between the predicted and measured ω for SMR, CMR and DMR are plotted in Figs. F-1a through F-1e for the five models of equation of state for CO_2 of Appendix B. Note in Fig. F-1a, $\Delta\omega$ begins to increase beyond $M_s \approx 7$, the range of M_s over which dissociation becomes significant according to the equilibrium CO_2 model (cf. Fig. B3), while agreement between theory and experiments is good for quasi-equilibrium models Q1 and Q2 which neglect dissociation but take into account the excitation of the vibrational modes; see Appendix B for details. As seen in Fig. F-1e, the perfect gas model with $\gamma = 1.290$ shows the least $\Delta\omega$ among the five models for lower shock Mach number range ($M_s \lesssim 3.5$), the predicted ω deviates from the measured angles significantly for higher M_s.

Inspection of the five diagrams shows that so far as the parameter ω is concerned, Models Q1 or Q2 appear to be most consistent with experiments. It is, however, important to note here that, since it was not possible to accurately measure the desired angle at the triple point owing to the limiting resolution power of photographs, the measured angle is the angle subtended by the trajectory of the triple point and the straight segment of the reflected shock, which may or may not be equal to the angle in the immediate vicinity of the triple point, say within 0.2 mm.
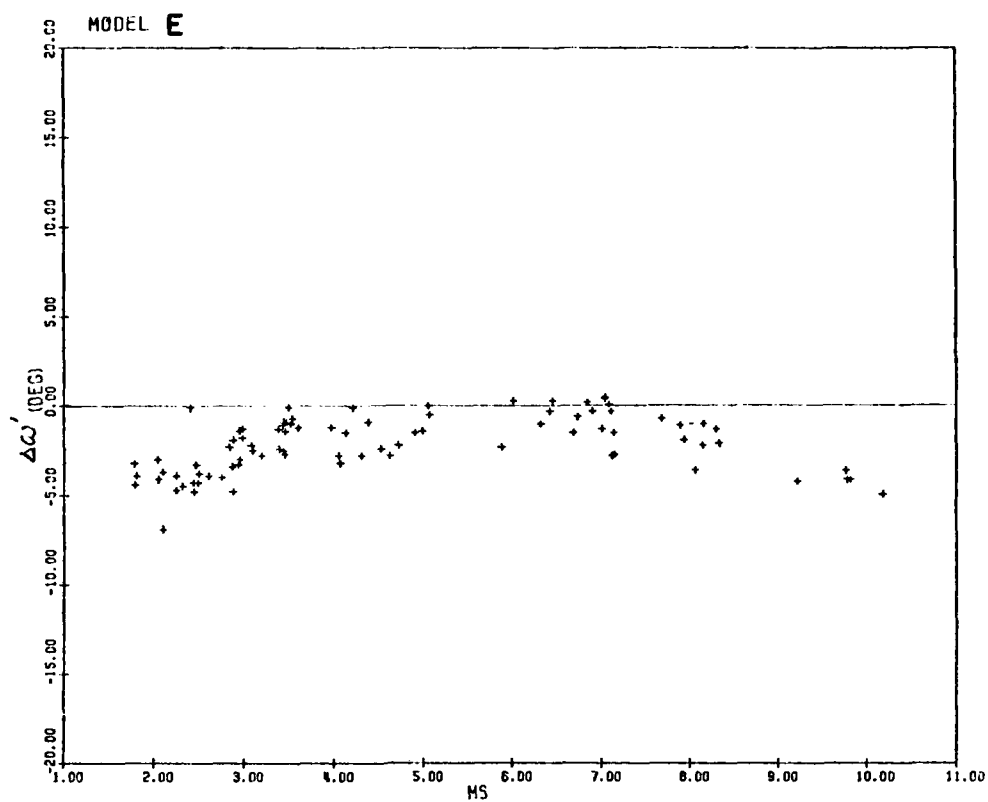
FIG. F1 COMPARISON OF THE PREDICTED AND MEASURED ANGLES OF REFLECTION.

(a) EQUILIBRIUM CO_2 (MODEL E) $\Delta\omega = (\omega)_{predicted} - (\omega)_{measured}$
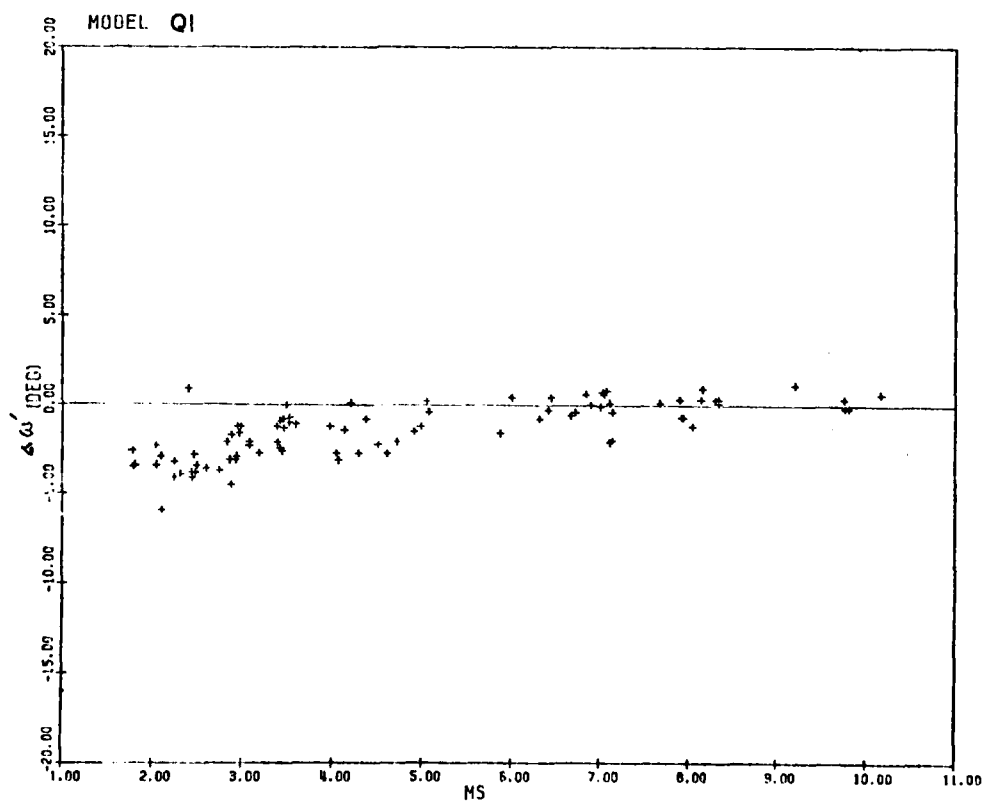
FIG. F1 - CONTINUED. (b) QUASI-EQUILIBRIUM CO_2 (MODEL Q1)
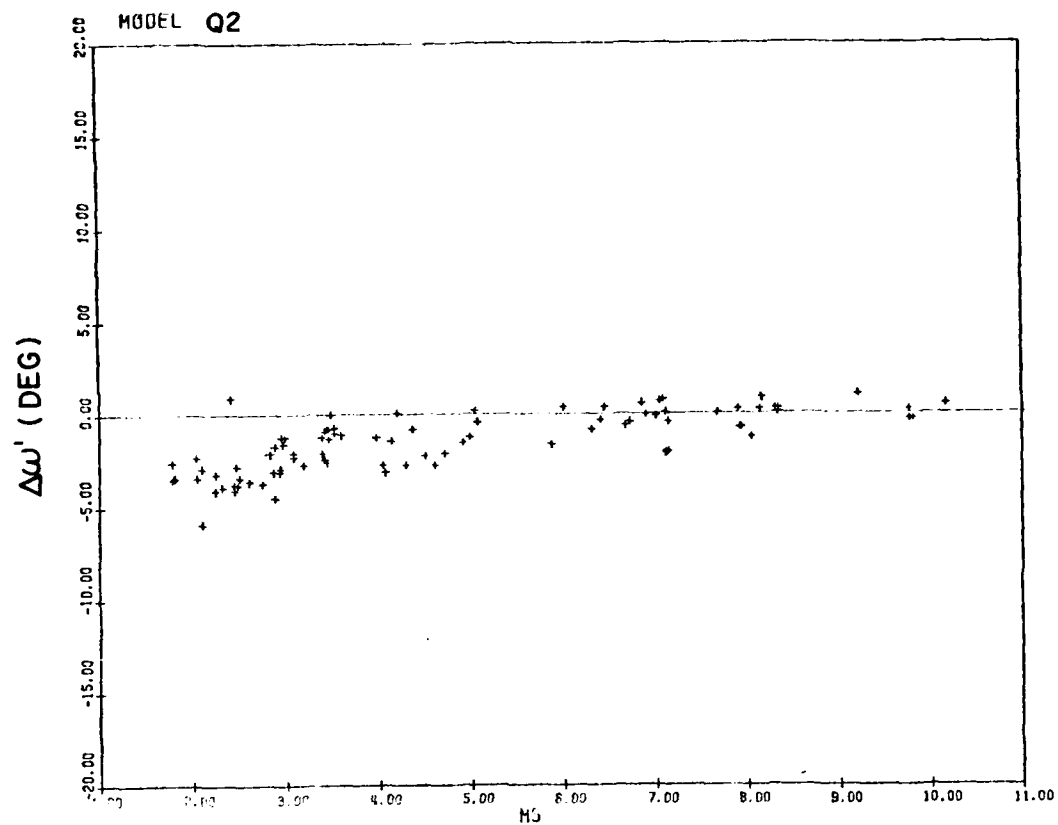
MODEL **Q2**

FIG. F1 - CONTINUED.   (c) QUASI-EQUILIBRIUM CO_2 (MODEL Q2)
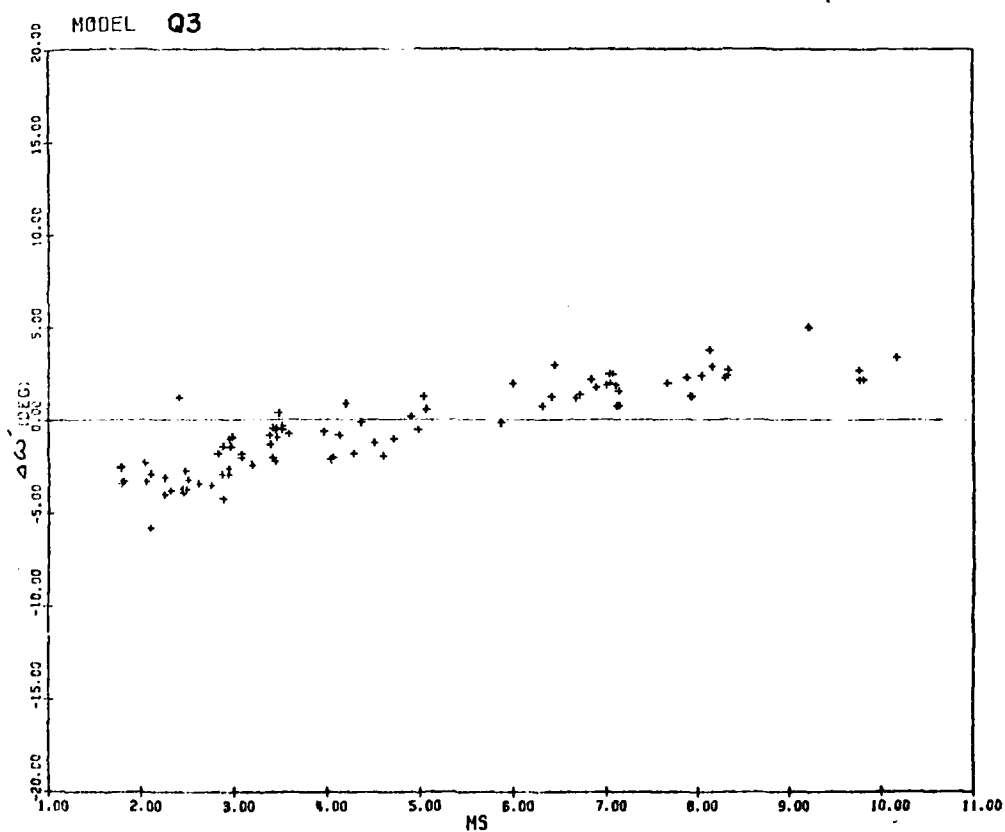
MODEL **Q3**

FIG. F1 - CONTINUED.   (d) QUASI-EQUILIBRIUM CO_2 (MODEL Q3)
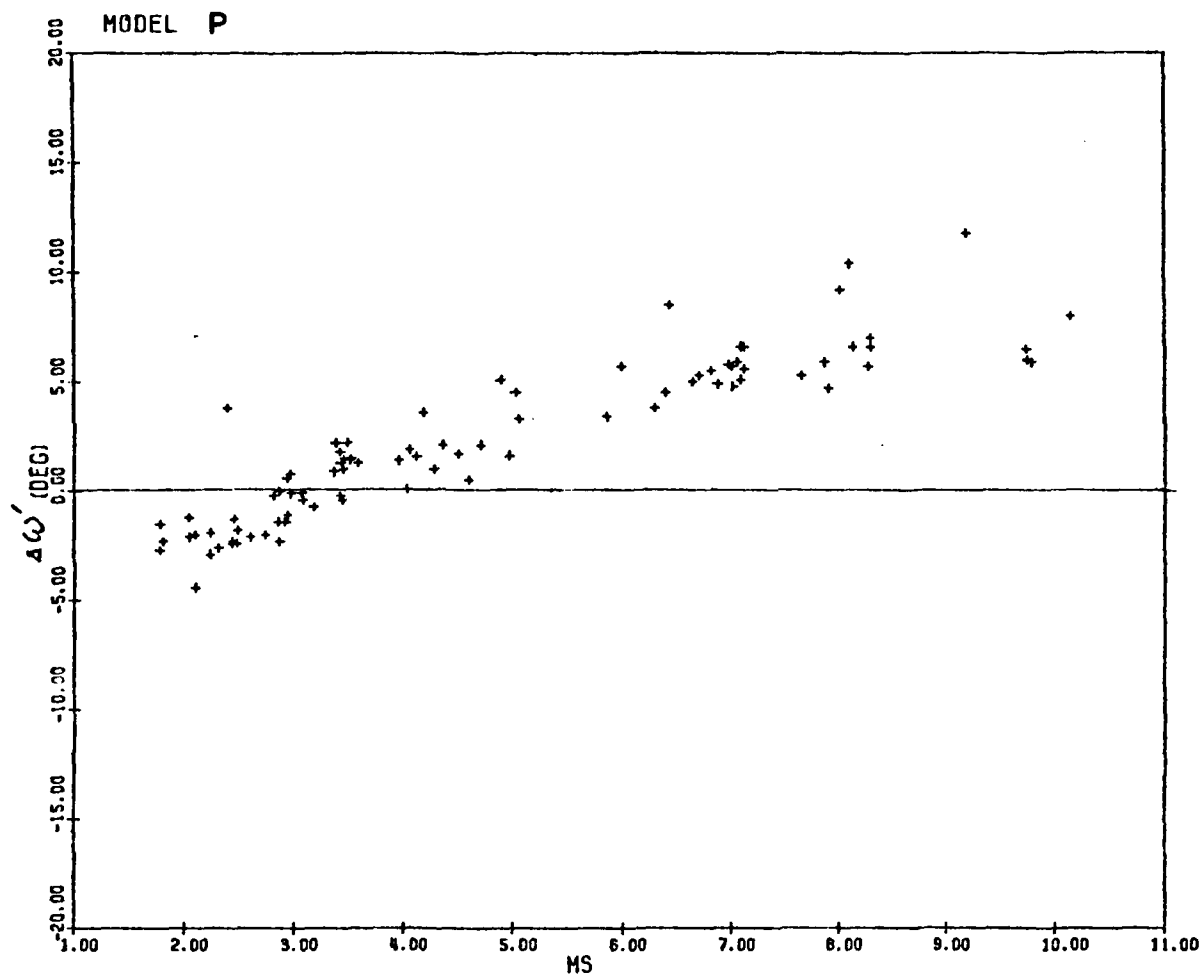
MODEL P

FIG. F1 - CONTINUED.

(e) $\gamma = 1.290$ (MODEL P)

APPENDIX G

BOW WAVES

In the shock-tube flow, a bow wave is formed at a concave corner even if the flow behind the incident shock is subsonic. This occurs as a result of the reflection process of the incident shock at the concave corner: as the incident shock impinges on the corner, the reflected shock becomes a bow wave and begins advancing into the oncoming induced flow behind the incident shock. Thus even though the flow is subsonic relative to the shock tube (this occurs when $M_S = 2.068$ for $\gamma = 1.4$ and $M_S = 1.906$ for $\gamma = 1.29$), the bow wave advances with a supersonic speed relative to the induced flow as a result of vector addition of the two velocities in opposite directions and it is only by moving into the oncoming flow and so maintaining the supersonic speed relative to it that the bow wave can exist at all in this circumstance. Thus, if the induced flow is supersonic relative to the shock tube, a bow wave may be either attached or detached; and in the latter case, it will eventually assume an equilibrium position at a fixed distance away from the corner. If, on the other hand, the induced flow is subsonic relative to the shock tube, a bow wave will remain nonstationary until it meets the contact surface and refracts. For the supersonic induced flow relative to the shock tube, the limiting angles at which a bow wave detaches from the wedge can be calculated by the methods available in standard text books [see, for example, Liepmann & Roshko (65)].

APPENDIX H

COMPUTER PROGRAMS

Included in this appendix are the listing of the computer programs to calculate the transition angles of shock reflection, to draw the maps of various domains as shown in Figs. 38 and D1, along with the listings of the programs to calculate the thermodynamic properties of equilibrium, quasi-equilibrium, and perfect CO_2, and to draw P- shock polar diagrams.

IBM system 3033 and the IBM system 360-Gould plotter combination at the University of Toronto Computing Centre were used.

Detailed analysis was done on each experiment using the listed computer programs. Sample output of two experiments, one for regular reflection and the other for complex Mach reflection, are also included in this appendix.

The above may be obtained by writing to Prof. I. I. Glass at UTIAS.